HIGHER ORDER SPECTRA AND UNIVERSAL SHAPE FUNCTIONS IN
AVALANCHE MODELS

BY

AMIT PANKAJ MEHTA

B.A., Cornell University, 2000
M.S., University of Illinois at Urbana-Champaign, 2002

DISSERTATION

Submitted in partial fulfillment of the requirements
for the degree of Doctor of Philosophy in Physics
in the Graduate College of the
University of Illinois at Urbana-Champaign, 2005

Urbana, Illinois

INFORMATION TO USERS

The quality of this reproduction is dependent upon the quality of the copy submitted. Broken or indistinct print, colored or poor quality illustrations and photographs, print bleed-through, substandard margins, and improper alignment can adversely affect reproduction.

In the unlikely event that the author did not send a complete manuscript and there are missing pages, these will be noted. Also, if unauthorized copyright material had to be removed, a note will indicate the deletion.

UMI®

CERTIFICATE OF COMMITTEE APPROVAL

University of Illinois at Urbana-Champaign
Graduate College

June 1, 2005

We hereby recommend that the thesis by:

AMIT PANKAJ MEHTA

Entitled:

HIGHER ORDER SPECTRA AND UNIVERSAL SHAPE FUNCTIONS IN AVALANCHE MODELS

Be accepted in partial fulfillment of the requirements for the degree of:
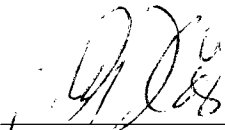
Doctor of Philosophy

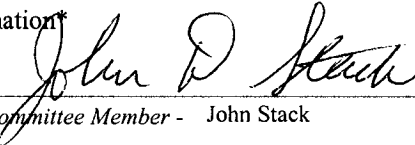*Signatures:*

Director of Research - Karin Dahmen

Head of Department - John Stack

Committee on Final Examination*

Chairperson - Alfred Hubler

Committee Member - John Stack

Committee Member - Michael Weissman

Committee Member -

Committee Member -

Committee Member -

* Required for doctoral degree but not for master's degree

We study non-equilibrium critical phenomena in disordered systems that crackle. Crackling refers to jumps or "avalanches" over many orders of magnitude that are induced by a slow external driving force or field. We study two kinds of crackling noise produced by disordered systems: Barkhausen noise, that is produced by magnetic material magnetized by a changing external field, and earthquakes, that are produced by the contact of two shifting tectonic plates. Both systems exhibit critical behavior; critical exponents and universal scaling functions associated with the crackling noise are studied in both systems. Theoretical results are obtained from simulation and compared with experiment and observation. Universal scaling functions allow a sharper test of theoretical models against experiment. While agreement in critical exponents is observed between theory and experiment, differences are found between universal scaling functions. Also, a simple mean field earthquake model that produces aftershocks is proposed. We also introduce a second approach to test theoretical models against experiment. In this approach, Barkhausen noise is analyzed with higher order spectral transformations, in both mean field theory, simulation, and experiment. Novel exponents are found through our analysis and key differences are found between simulation and experiment.

To my wife, Shilpi Mehta, whose support and encouragement made the rapid completion of my

thesis possible.

Acknowledgments

I would like to begin by thanking the most important person in my graduate career, my advisor Karin Dahmen. I had the opportunity to do a summer project with Karin when I first arrived to Urbana/Champaign. After seeing her passion for research, her contagious enthusiasm, and her positive attitude and mindset I decided to continue working with her. Her passion and enthusiasm has not only keep me excited about research, especially at times when I had hit a dead end, but she also challenged me and stretched me to reached my full potential. She always has the best interests of her students in mind, and she has gone out of her way to help them. I am very grateful for the opportunity of working with her for the past five years; this experience have left an indelible mark on my life.

I would also like to thank Bob White and John Carpenter for their help and guidance, especially in the beginning when I was new. Although I did not get an opportunity to collaborate with them on any projects, they were always available for many useful discussion, and to lend a helping hand.

In addition to my advisor, I am grateful for the opportunity to have collaborated with Yehuda Benzion, Mike Weissman, Jim Sethna, Andy Mills, and Tim Wotherspoon. I really enjoyed working with them, and they made a significant contribution to the research in this thesis.

I am grateful for my committee members: Mike Weissman, John Stack, and Alferd Hubler, for taking the time and making the commitment to be a part of my committee, and for the interesting questions they asked during my prelim examination.

Regarding my undergraduate physics education at Cornell I have many people to thank. I would like to thank: Peter Lepage, Saul Teukolsky, Jim Sethna, André Leclair, Henry Tye, Lou Hand, Ben Widom (chemistry), Karl Berkelmen, John Marohn (chemistry), and Roald Hoffman (chemistry) for the invaluable education and inspiration I obtained from their classes. I would also like to thank Lou Hand, Nari Mistry, and Al Sievers for giving me the opportunity to do research

Table of Contents

viii

List of Tables

List of Figures

xiii

List of Abbreviations

RFIM zero-temperature Random Field Ising Model

RBIM zero-temperature Random Bond Ising Model

RAIM zero-temperature Random Anisotropy Ising Model

IRM Infinite Range Random Field Ising Model ($T = 0$)

MFT Mean Field Theory

SOC Self-Organized Criticality

Chapter 1

Introduction

1

Equilibrium critical phenomena have formed a field of intense interest in science for much of the century. In the past few decades a new range of phenomena, driven systems that are far from equilibrium, such as turbulence and disordered systems, have broadened both the understanding and interest in critical phenomena [1, 2, 3, 4, 5].

Certain disordered systems *crackle*, that is when such a system is slowly driven it responds by discrete jumps of various sizes [1]. These jumps or events are often collective events called *avalanches*. The crackling is often the result of non-equilibrium collective transport in random media, where the interactions are strong enough that thermal effects are negligible and the system has many interacting degrees of freedom. There are many disordered systems that crackle: superconducting vortex line avalanches [6], resistance avalanches in a superconducting film [7], capillary condensation of helium in Nuclepore [8], acoustic emission in athermal martensites [9], and many more [1]. However, our focus will be on two systems: earthquakes, which are a result of two tectonic plates rubbing against each other over long periods of time [10], and Barkhausen noise in magnetic systems, which results from avalanches of spin reversals of magnetic domains in a magnetic material that is exposed to a changing external magnetic field [11]. Both phenomena, Barkhausen noise avalanches, and earthquakes span many orders of magnitude in size. In fact the size distributions of these avalanches/earthquakes are scale invariant (i.e. power law distributions) [10, 11]. The power law distributions in models of both systems are the result of an underlying critical point (continuous phase transition) where *universality* is observed. Universality simply means the statistics of the system are scale invariant and depend only on a few generic properties, such as dimensionality, range of interaction, and symmetries of the system.

The presence of universality allows us to extract correct predictions for the scaling behavior on long length scales from simple models for Barkhausen noise and earthquakes, which need only include a few essential details. These predictions may be tested against experiment and observation by comparing critical exponents, that is the exponents corresponding to the power law distributions of statistical quantities at the critical point. For example, τ is the avalanche size distribution exponent given by: $D(S) \sim S^{-\tau}$ (S is the avalanche size). These critical exponents are universal and therefore play an important role in characterizing critical phenomena, specifying the *universality class* of a particular system. However, we present strong evidence that comparing critical exponents

2

alone may not be sufficient to characterizing critical phenomena. We present two powerful methods to test theoretical models, that exhibit underlying criticality, to experiment. These methods not only allow a more stringent test of theory versus experiment, they even provide evidence for or against an underlying critical point in certain experimental systems.

1.1 First Method - Universal Scaling Functions

The first method of our analysis consists of studying universal scaling functions at the critical point; these scaling functions should be as universal as critical exponents. The advantage of comparing a scaling function is the comparison of an entire continuous set of points versus a single exponent, in other words rather than comparing a number (i.e. critical exponents), we are comparing a *shape*. As mentioned above we focus on two systems: Barkhausen noise in magnets and earthquakes, that are further discussed below in 1.1.1 and 1.1.2, respectively.

1.1.1 Avalanches and Barkhausen Noise

Real materials, have dirt, or disorder, which often leads to slow (glassy) dynamics due to complex free energy landscapes with diverging energy barriers [12]. On long length scales and practical time scales, thermal effects often become unimportant. Indeed, when such a system is driven by an external field it jumps from one local metastable free energy minimum to the next, and the state of the system depends on its history.

In magnetic materials jumps from one local minimum to the next involve a collective process whereby clusters of magnetic domains change the direction of their magnetization, in an avalanche. These avalanches can be triggered by a slowly but continuously increasing homogeneous external magnetic field H (taken from $-\infty$ to $+\infty$). These avalanches produce so-called Barkhausen noise, which can be observed experimentally as a voltage signal induced in a pickup coil wound around the magnet. Experiments show that these avalanches come in all sizes; their sizes are typically distributed according to a power law over several decades.

We model the dynamics of Barkhausen noise in magnets using the $T = 0$ random field Ising model (RFIM). The RFIM exhibits a disorder-induced continuous phase transition, and a corresponding critical point [11]. In the presence of weak demagnitizing infinite range forces the RFIM

3

(at low disorder) is SOC [13, 14, 16], and effectively models amorphous materials under tensile stress such as $Fe_xCo_{85-x}B_{15}$ where surface tension is dominant [19]. When dipolar interactions are added to the infinite range RFIM, they lower the upper critical dimension to 3, making the scaling in mean field theory exact in the physical dimension [20]. The mean field RFIM effectively models hysteresis and Barkhausen noise in polycrystalline or partially crystallized materials such as $FeSi$ where dipolar interactions dominate [19]. In chapter 3 we present details of the RFIM, and in chapter 5 we compare universal avalanche shape functions and exponents obtained from simulation and experiment. Our analysis tests whether the $T = 0$ RFIM is in the same universality class as the experimental systems exhibiting Barkhausen noise.

1.1.2 Earthquakes and Criticality

Earthquake phenomenology is characterized by several power law distributions. The most famous of these are the frequency-size distributions (i.e. histograms) of regional and global earthquakes [10], and the modified Omori law for the aftershock decay rate around large rupture zones [21, 22]. Using the seismic moment M_0 for the earthquake size, the frequency-size distributions (or moment histogram) has the form (e.g., [23])

$$n(M_0) \sim M_0^{-1-\beta} \tag{1.1}$$

Where $M_0 \sim \sum_i \Delta u_i \Delta A_i$ with Δu_i and ΔA_i being the local slip and rupture area during an earthquake, respectively. A related, more commonly used form in terms of earthquake magnitude M is

$$log(n(M)) = a - bM \tag{1.2}$$

where $n(M_0)dM_0 = n(M)dM$, the constant a characterizes the overall rate of activity in a region, and the "b-value" gives the relative rates of events in different magnitude ranges. Using the observed moment-magnitude scaling relation $M \sim 2/3 log(M_0)$ for large earthquakes [24], the exponent β of (1.1) is related to the b-value of as $b = 1.5\beta$.

The modified Omori law for aftershock decay rates is:

4

$$\Delta N / \Delta t \sim K(t + c)^p \tag{1.3}$$

where N is the cumulative number of aftershocks, t is the time after the mainshock, and K, c, and p are empirical constants. The exponents in (1.1) and (1.3) are stable for data collected over large space-time domains, with some clear deviations from global averages related to faulting type and regional properties [25]. For example, the b-values of strike-slip, thrust, and normal earthquakes with depth ≤ 50 km in the global Harvard catalogue are about 0.75, 0.85, and 1.05, respectively [26]. As another example, regions with high heat flow often have short aftershock sequences with relatively large exponent (e.g., $p > 1.25$), while regions with low heat flow have long aftershock sequences with low exponent (e.g., $p < 0.9$) [21, 22]. The association of earthquake statistics with power law relations like Eq. (1.1) and Eq. (1.2) led some to suggest that earthquake dynamics is associated with an underlying critical point [20, 27, 28, 29, 30, 31, 32]. However, power law distributions can be generated by many other mechanisms [33, 34] and it is important to develop criteria that can provide stronger evidence for or against the association of earthquakes with criticality. By comparing the earthquake moment rate function, $dm_0(t)/dt$, that gives the slip of the fault per unit time, in our earthquake model versus observation we strengthen the case for the existence of an underlying critical point. In chapter 4 we present details of our earthquake model and extend the model to include dynamical strengthening, and in chapter 6 we give the results of our analysis of the moment rate function in our model and observations.

1.2 Second Method - Higher Order Spectra

Our second method of analysis involves the study of higher order spectra that include: second spectra, 1.5 spectra, and cross second spectra. Higher order spectra give valuable information about a variety of systems that include: metastable states in vortex flow [35], natural auditory signals [36], conductance-noise in amorphous semiconductors [37], fluctuating current paths in devices [38], and quasi-equilibrium dynamics of spin glasses [39]. However, in this analysis we study the avalanche dynamics of Barkhausen noise in mean field theory. However, our results are applicable to a broad array of systems that have the same mean field dynamics, these systems include: charge density

5

waves, vortices in type II superconductors, crack propagation, and earthquakes [40].

In particular, we look at the higher order spectra (that include second spectra, 1.5 spectra, and cross second spectra) that effectively measure the correlations of the fluctuations of the power spectrum in *time*. The power spectrum of Barkhausen noise train voltage $V(t)$ is defined as $I(\omega) = |V(\omega)|^2$. The power spectrum of, $V(t)$, is proportional to the power that each frequency component (from the train) contributes to the total power. The second spectra gives information on how a given frequency component, f_1, in the power spectrum $S(f_1)$, varies in time–during the duration of the train. If the power contribution, $S(f_1)$, for a given f_1 is *stationary*, then its second spectra at f_1 will be zero; however, if it varies during the course of the Barkhausen train (i.e. *non-stationary*), this variation will show up in the second spectrum at f_1.

We calculate the higher order spectra of Barkhausen noise in mean field theory, obtain novel exponents, and compare our results with experiment and simulation; we find surprising differences between our experimental results and our simulation results. Our results are given in chapter 7, details of the analytical calculation of higher order spectra are given in Appendix F-G. Also, as we show in chapter 2, higher order spectra not only serve as a powerful tool to test theoretical models against experiment, they also provide evidence for or against the existence of an underlying critical point and the presence of SOC in certain systems.

6

Chapter 2

Experiments and Observations

7

In this chapter we discuss several experiments and observations in a variety of systems, ranging from earthquakes [41] to natural auditory and visual stimuli [36]. Most of the systems we discuss in this chapter exhibit avalanche dynamics and are relevant to the research discuss in this thesis. However, with regards to higher order spectra, we also discuss a few systems, such as resistance fluctuations [37] and natural auditory and visual stimuli [36], that do not exhibit avalanche dynamics. We include these systems to demonstrate the broad range of applicability of higher order spectra analysis. In section 2.1 we give an overview of experiments (and observations) where shape functions have been analyzed. In section 2.2 we overview experiments where higher order spectra played a crucial role in the analysis.

2.1 Shape Functions

2.1.1 Magnetic Material

We present the shape functions from two Barkhausen noise experiments obtained from two different materials [42, 43] given in Fig. (2.1-2.2). The materials were placed in a solenoid with a sinusoidally varying magnetic field, a pickup coil was wrapped around the material in question in order to measure the induced voltage. The Barkhausen noise is simply the train of induced voltage pulses measured from the material as a result of magnetic domains collectively flipping in the presence of the varying magnetic field. Durin et al's [43] sample is from an experiment on an amorphous alloy, $Fe_{64}Co_{21}B_{15}$, under tensile stress; the sample was under stress so as to enhance stress-induced anisotropy so much that the long range dipolar interactions can be neglected [43]. Spasojević et al's sample was a quasi-two-dimensional metal glass, more specifically a commercial VITROVAC 6025 X [42]. Additional details about Durin et al's, and Spasojević et al's experiment can be found elsewhere [14, 42, 43, 44].

The pulse (or avalanche) shapes in both materials were obtained by rescaling the duration and height of the Barkhausen pulses to one set value, so that a mean pulse shape could be ascertained. We notice that both pulse shapes obtained in Spasojević et al's and Durin et al's experiment are *asymmetric* to the left, and they are also asymmetric to different degrees. In subsequent chapters we shall discuss these asymmetries in more detail.

8
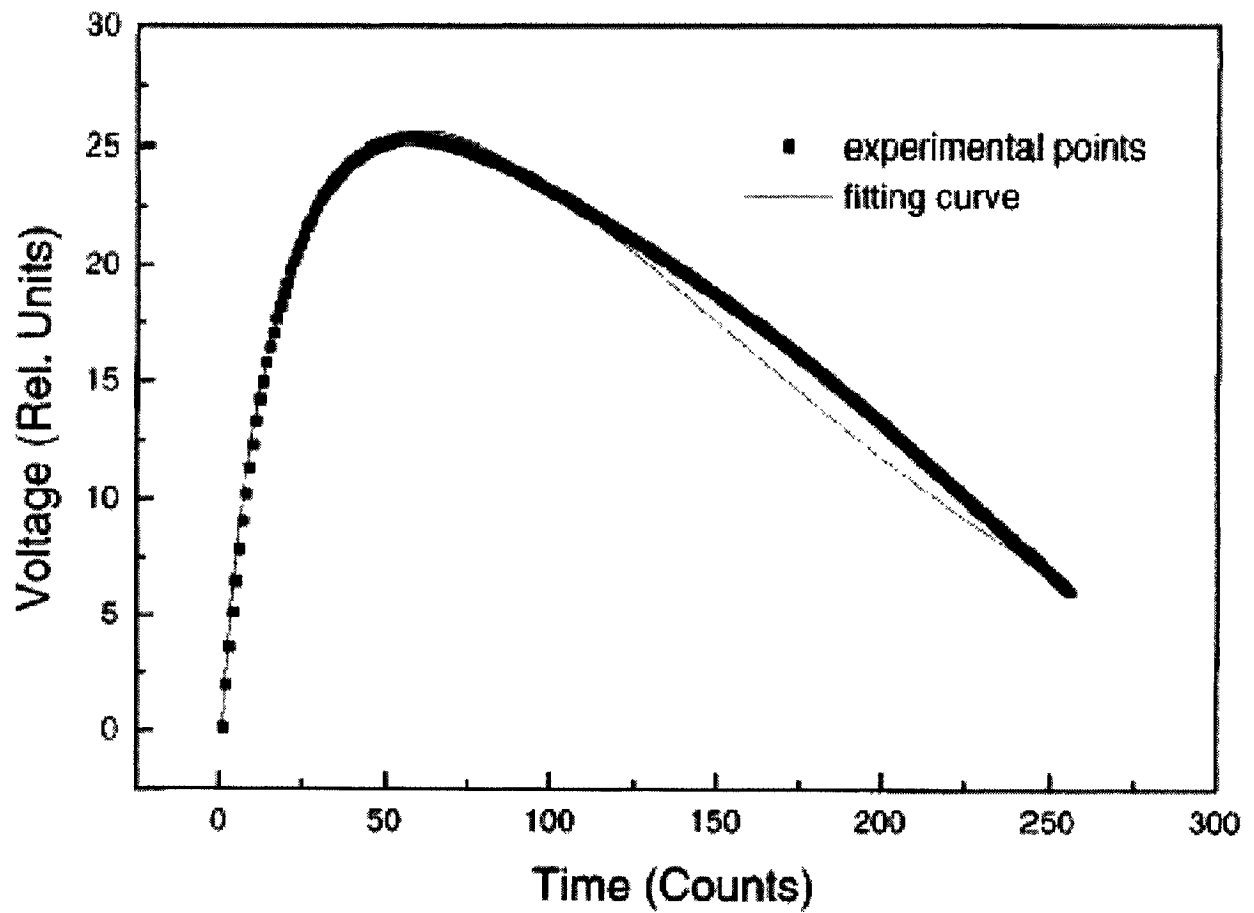
Figure 2.1: Average Barkhausen pulse shape obtained from Spasojević et al's sample [42]. Points represent actual experimental data, while the solid line represents a fit of the form $g(t/T) = exp(-t/T)$.

9
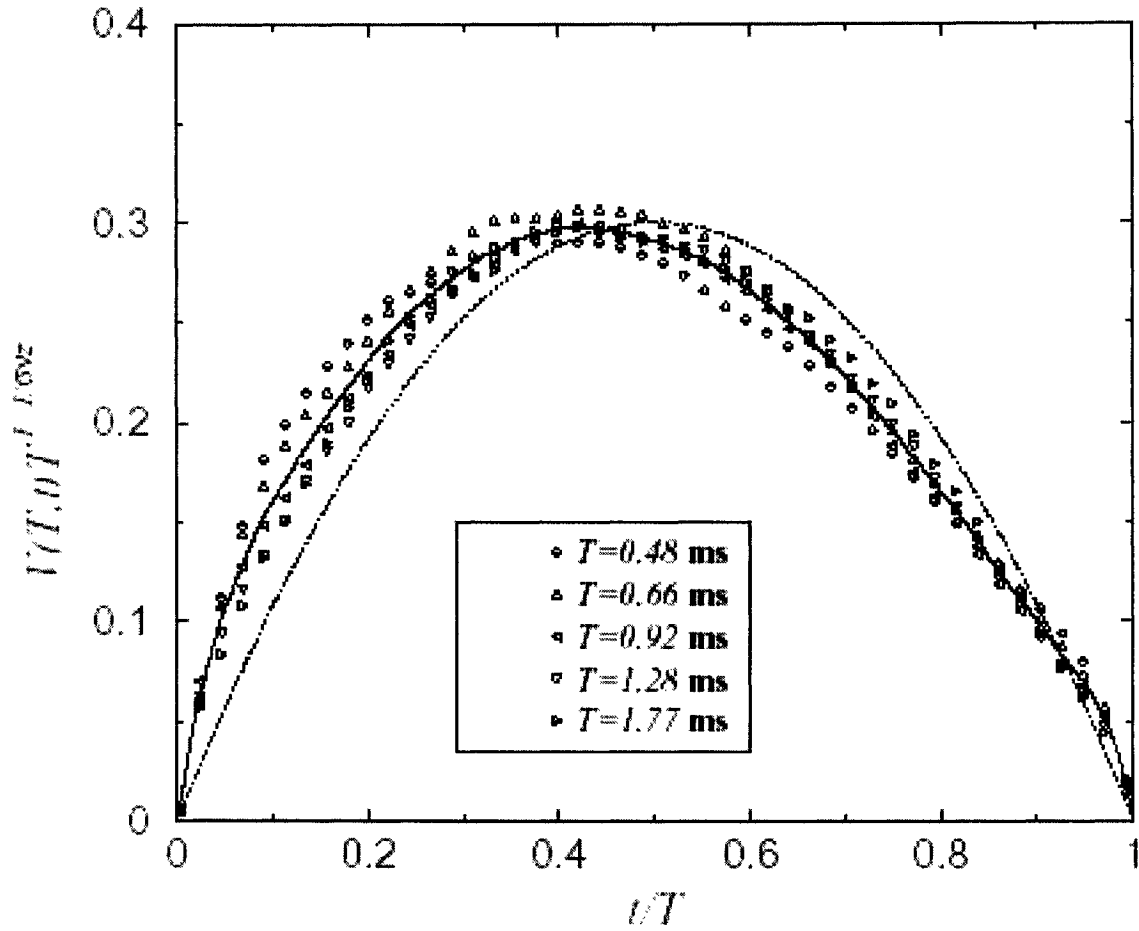
Figure 2.2: Mean collapsed avalanche shape function for the $Fe_{64}Co_{21}B_{15}$ amorphous crystal, figure was obtained from Durin et al's sample [43]. The x axis is rescaled by, T, the duration of the avalanche, so that all shapes have a unit magnitude; to obtain a collapse the y axis is rescaled by $T^{1-1/\sigma\nu z}$, the scaling of the average avalanche height [13]. The dotted line is a symmetric parabola, indicating the shape function is slightly asymmetric to the left.

10

2.1.2   Earthquakes

In the last decade high precision seismic measurements have made time versus moment rate profiles of earthquakes obtainable; these time profiles give the slip of the fault per unit time for an earthquake as a function of time (i.e. the area under the time profile is the moment of the earthquake). A recent study of shape functions in seismic activity was done by Heidi Houston [41] from time profiles of earthquakes ascertained by the University of Michigan seismology group [45] by inversion of teleseismically recorded body waves (obtained from Global Seismic Network [46]). The time profiles of these earthquakes are separated into two categories: deep events (below 40 km), and shallow events (above 40 km). Also, in order to compare the shapes of the time profiles, the profiles were rescaled by two methods: moment scaling and duration scaling. Moment scaling rescales the profiles so that the area (or moment) under all profiles are the same, on the other hand, duration scaling rescales all time profiles to a fixed duration and then rescales the height so the area under the profiles remains the same. In Fig. 2.3 we show the shape functions that were obtained from moment scaling (top) and duration scaling (bottom). In subsequent chapters we shall find that the non-plate boundary events (or deep events) from this study agree well with predictions from the mean field Benzion-Rice model [47].

2.2   Higher Order Spectra

2.2.1   Magnetic Material

In Figs. (2.4-2.5) we present the second spectra and the real 1.5 spectra obtained from an experiment by Petta et al [48]. The experiment was performed on $Fe_{64}Co_{21}B_{15}$, with a sample ribbon of dimensions $20cm \times 0.9cm \times 35\mu m$, this sample geometry reduces the effects of the demagnetizing field. The domain walls are aligned parallel to the ribbon length. A small 50 turn pickup coil around the center of the sample detects the Barkhausen noise.

The second spectra (Fig. 2.4) fall off as $f_2^{-0.35}$ for high frequencies and the 1.5 spectra curves are weakly dependent on f_1. This indicates that the high frequency power comes from large avalanches, with avalanche durations much greater than $1/f_1$, as apposed to short pulses, with avalanche durations on the order of $1/f_1$ [48]. On the other hand, in Fig. 2.6 we have the second spectra

11
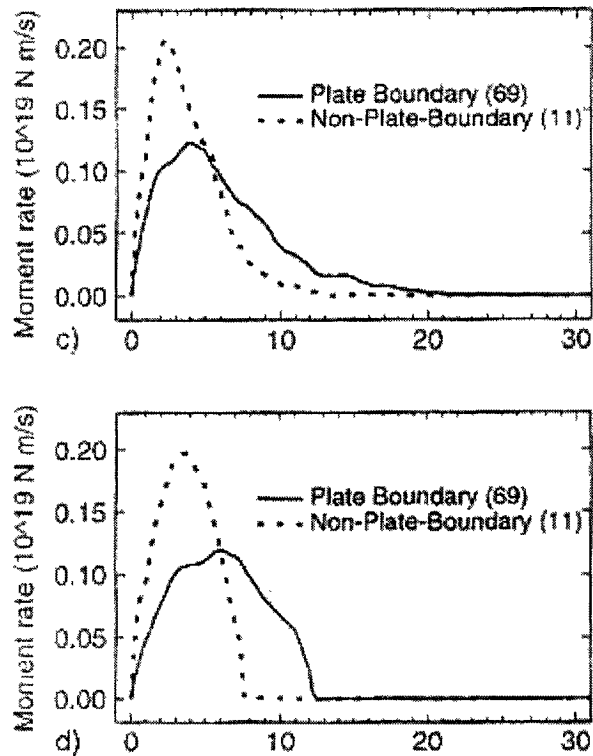
Figure 2.3: We present rescaled time versus moment rate profiles of seismic events determined with moment scaling (top) and duration scaling (bottom). Plate Boundary refers to shallow events (< 40 km), and Non-Plate Boundary refers to deep events (> 40 km). This figure was obtained from [41].

12

(bottom) and the 1.5 spectra (top) for 1.8% SiFe single crystal. In this case the second spectra are nearly flat and the 1.5 spectra are strongly dependent on f_1. As a result the high frequency power for 1.8% SiFe single crystal comes from individual short pulses (of duration $\sim 1/f_1$), therefore there is no underlying criticality in this system. This analysis is a powerful tool for ruling out systems that may appear to have an underlying critical point (or SOC) upon studying their power spectra.

Self-Organized criticality may also be ruled out with the assistance of higher order spectra. In a paper by O'Brien and Weissman [49] it was ascertained that Barkhausen noise obtained from an amorphous iron-based metallic alloy was absent of asymmetric precursors present in SOC systems. The imaginary cross second spectra were utilized in order to detect the possible presence of these asymmetric precursors, a negative value indicating the high frequency noise precedes low frequency, and vis-versa for a positive value. However, the imaginary cross second spectra were found to be zero in the absence of rare large asymmetric events that do not classify as asymmetric precursors.

2.2.2 Vortices in Type II Superconductors

Second spectra give valuable information on vortex flow. In particular, in a paper by Merithew et al [35] non-Gaussian flux-flow noise was recorded in the peak effect regime in $NbSe_2$. The flux-flow noise was analyzed via the second spectra. Traditionally, vortex flow noise was believed to be based on independent vortices or independent bundles of vortices [50], however, the second spectral analysis of the flux-flow noise demonstrates strong evidence to the contrary. The second spectra of the flux-flow noise determined by Merithew et al show a strong dependence on f_2 (see Fig. 2.7). On the other hand, the standard models of vortex flow noise based on independent vortices or bundles of vortices result in a flat second spectra that is independent of f_2. The strong f_2 dependence suggests that flux-flow noise is not the result of simple vortex motion, but rather nontrivial configuration fluctuations [35]. Similar to the case of Barkhausen noise mentioned above, higher order spectra allow us to distinguish a superposition of dynamics involving few degrees of freedom from complicated dynamics involving many degrees of freedom.

Another experiment involving vortex flow by Field et al [6] looked at vortex avalanches in the Bean critical state. In this experiment vortex avalanches are recorded by slowly ramping an external magnetic field on a tubular superconducting sample of $Nb_{47\%}Ti_{53\%}$ into the Bean critical state.

13
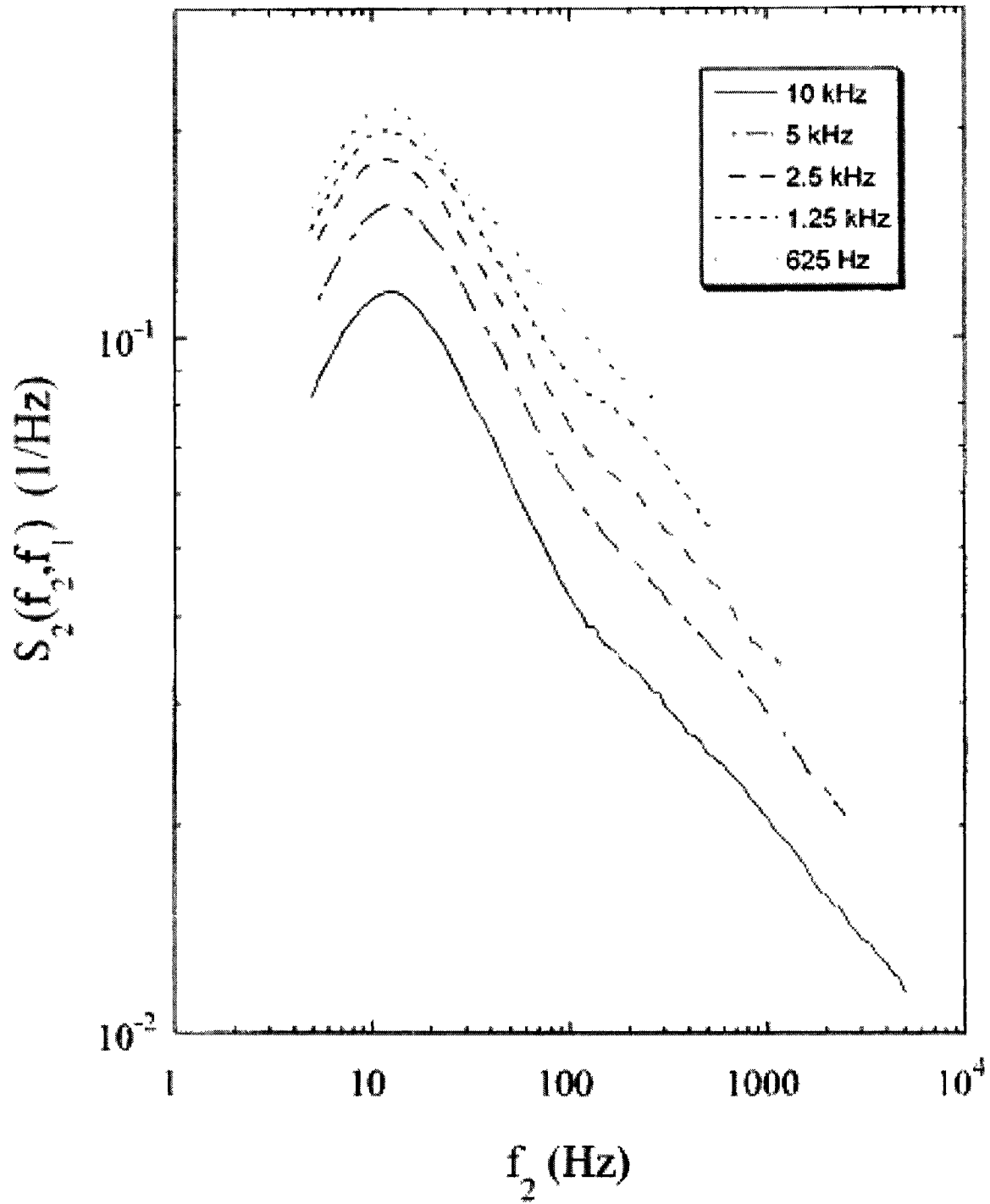
Figure 2.4: Second spectra obtained from Petta et al [48] for five different f_1 values, and $c = 0.2$ (from ABBM model).

14
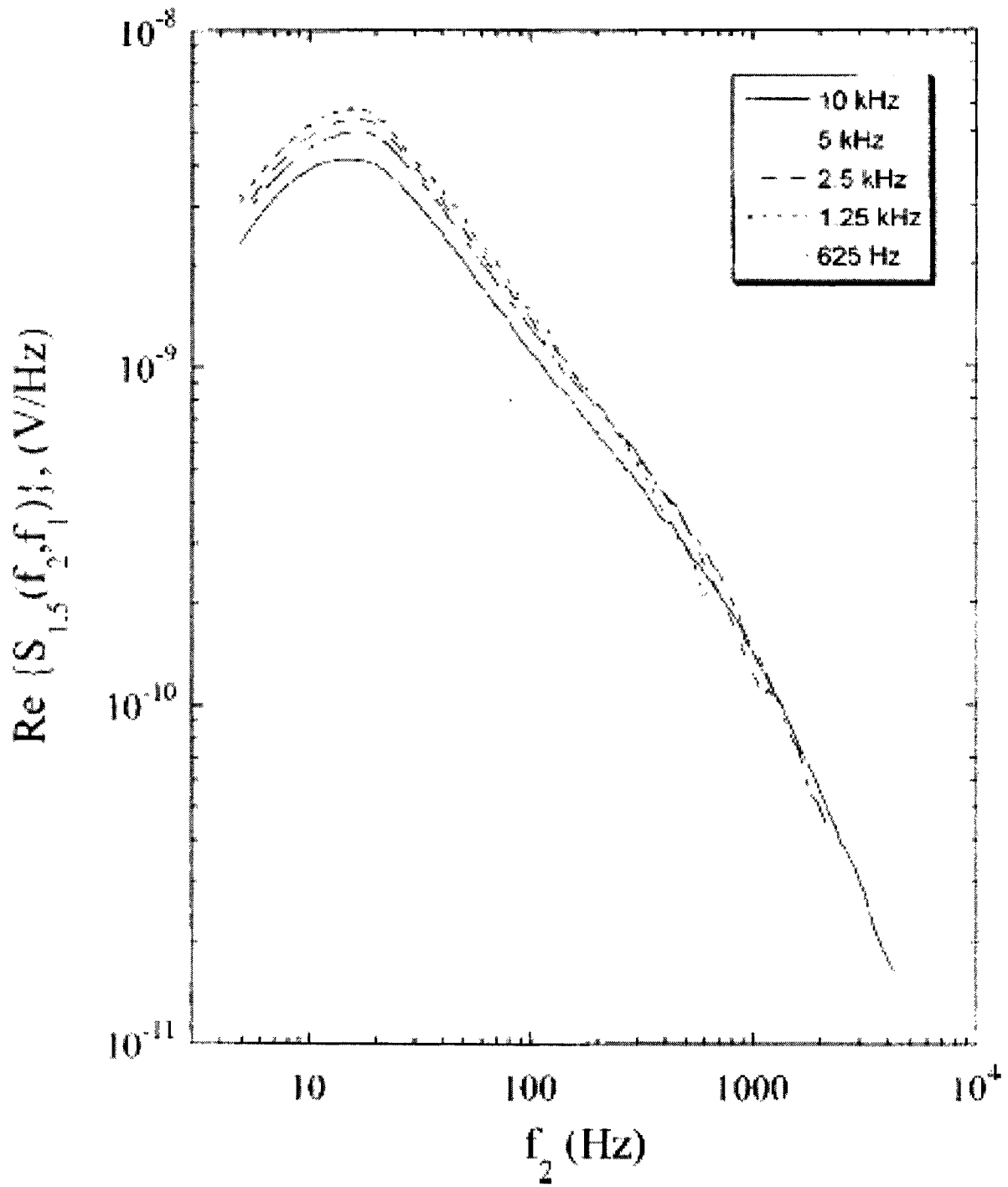
Figure 2.5: 1.5 spectra obtained from Petta et al [48] for five different f_1 values. The 1.5 spectra and the second spectra were obtained from the same data.

15
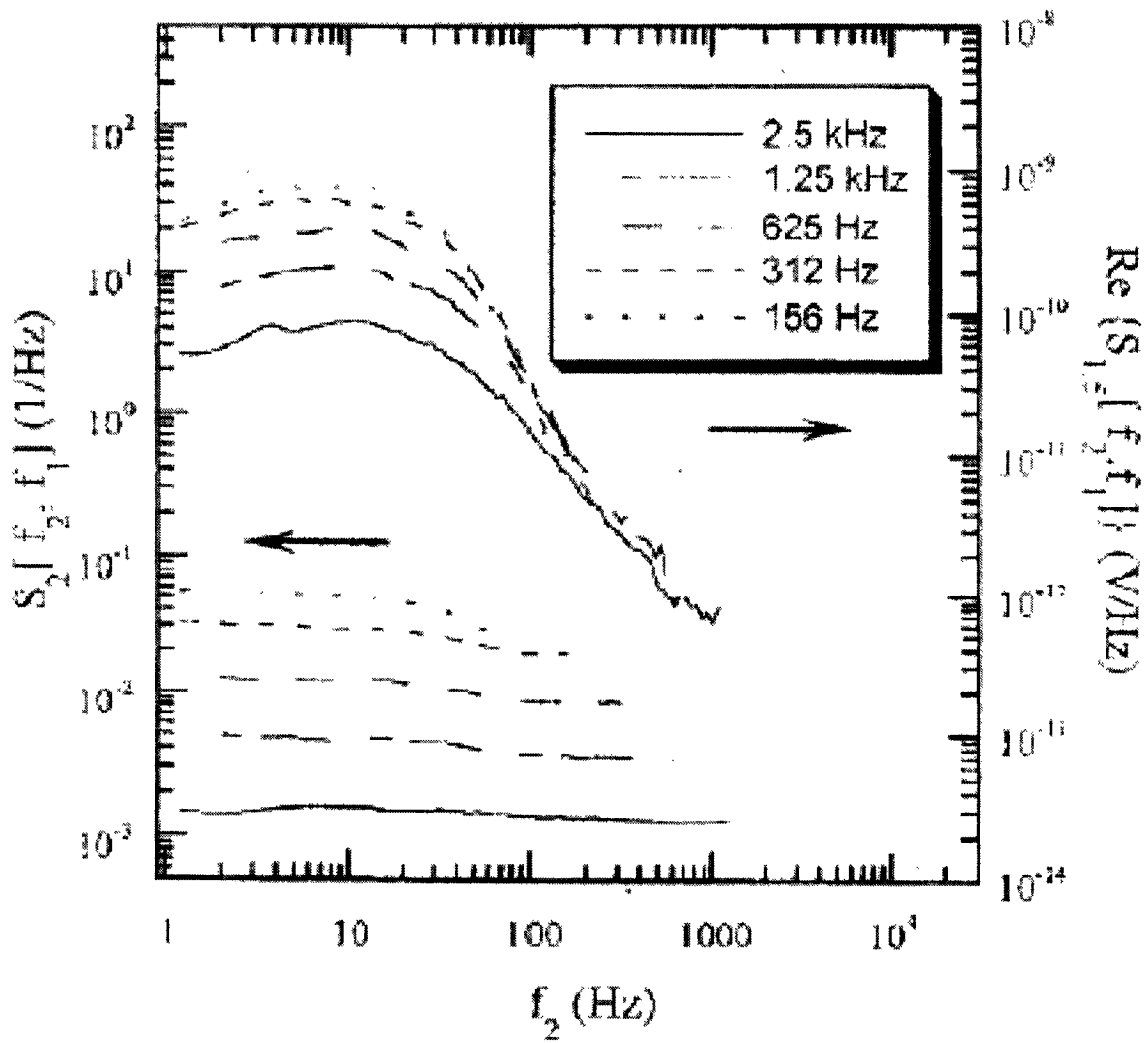
Figure 2.6: 1.5 spectra (top) and second spectra (bottom) for 1.8% SiFe single crystal obtained from [19].

16
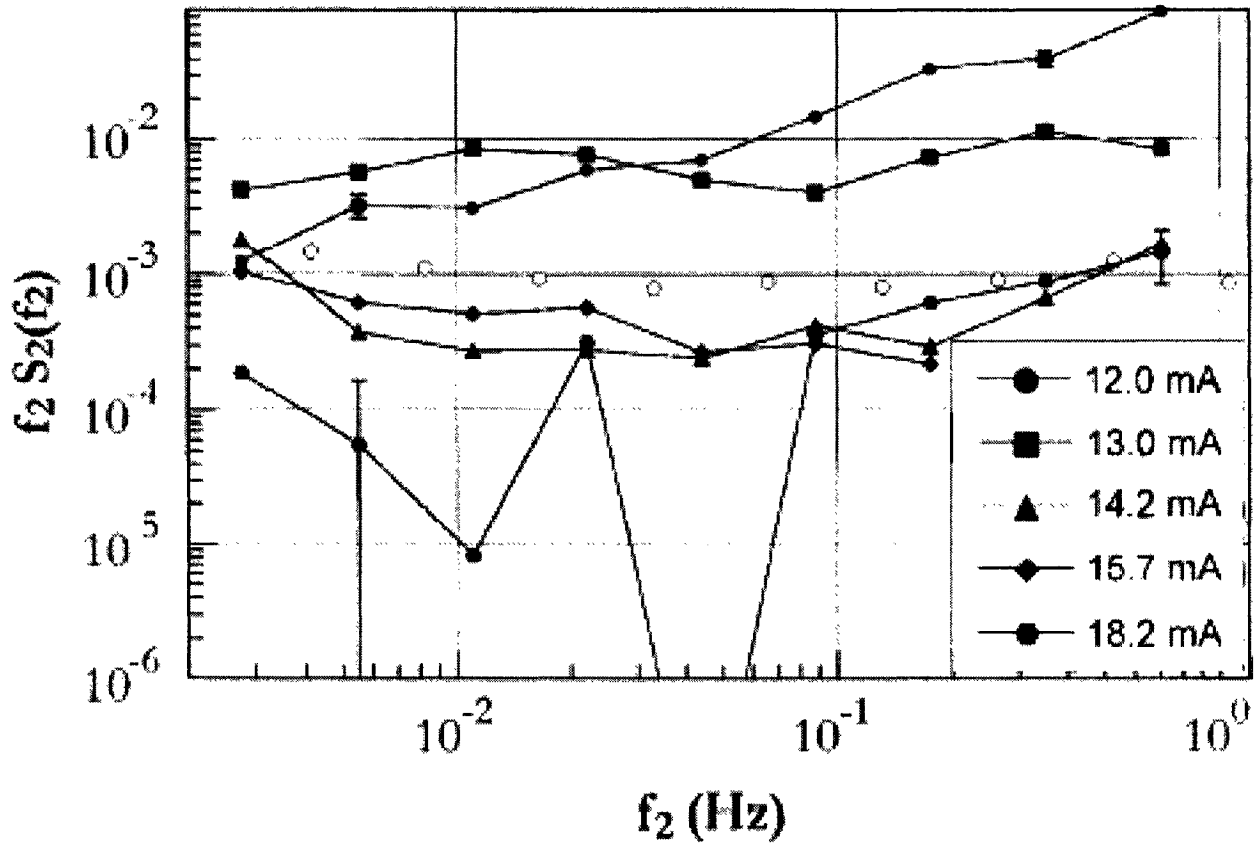
Figure 2.7: The second spectra for flux-flow noise for different currents. Figure was obtained from Merithew et al [35].

The avalanche size distribution and power spectra for the vortex avalanches are both power laws, strongly supporting the presence of an underlying critical point. The authors argue that the system is SOC, exhibiting threshold dynamics analogous to sandpiles. However, different cutoffs present in the avalanche size distribution for different values of the external magnetic field may suggest the presence of a plain old tunable critical point [11]. It would be interesting to see the higher order spectra for flux-flow noise generated by vortex avalanches in the Bean critical state. Not only would such an analysis allow a more rigorous comparison to sandpiles, it may help distinguish whether the system is SOC or plain old critical by identifying asymmetric precursors via the imaginary cross second spectra [49].

17

2.2.3 Natural Auditory and Visual Stimuli

Natural sounds and natural images have been shown to have second spectra with power law scaling [36]. In Fig. 2.8 we have the phase-only second spectra (curve a) for a human observer wearing a photodetector headband walking through outdoor scenery, phase-only indicates the Gaussian background has been removed. The second spectra scales as roughly $S_N^{2,\phi} \sim f^{-1/2}$, where f in Fig. 2.8 is the second spectra frequency. For 2D gray-scale natural images, the second spectra for the radial frequency f_r scale as $S_N^{2,\phi} \sim f_r^{-1}$. This exponent is consistent with the exponent of 1/2 found for natural sound, since in 2D we expect the exponent to be twice as large as 1D since, by dimensional analysis, we have $1/L^2$ instead of $1/L$ (L in this case since we have an image). There is a surprisingly simple explanation for the second spectra scaling and exponents, the exponent of 1/2 is due to different beat interactions between Fourier components at slightly offset frequencies [36].

2.2.4 Resistance Fluctuations in Hydrogenated Amorphous Silicon

An experiment by Parman, Israeloff and Kakalios [37] looked at the second spectra of resistance noise power fluctuations in n-type-doped hydrogenated amorphous silicon. Resistance fluctuations in most metallic solids and semiconductors have roughly $1/f$ power spectra that are the result of a superposition of statistically independent power spectra with a broad range of relaxation times. On the contrary, in hydrogenated amorphous silicon (a-Si:H) it has been shown that only a few microscopic processes are dominating the macroscopic conduction. To investigate further Parman et al [37] annealed a-Si:H film at 450K. Also, the film was n-doped by adding phosphine to the saline while the film was synthesized in a rf glow-discharge deposition system. The noise power of the resistance fluctuations was recorded at 300K.

The second spectra of the noise power of the resistance fluctuations, given in Fig. 2.9, give a power law which goes approximately as $1/f_2$, corroborating the fact that the noise power in a-Si:H is not the result of statistically independent power spectra over a broad distribution of relaxation times, since such a scenario would give a flat second spectra. In fact, there are clearly strong correlations between the noise power between different octaves. The authors suggest that the disorder in the a-Si:H, in the form of structural and electronic inhomogeneities, may be responsible

18
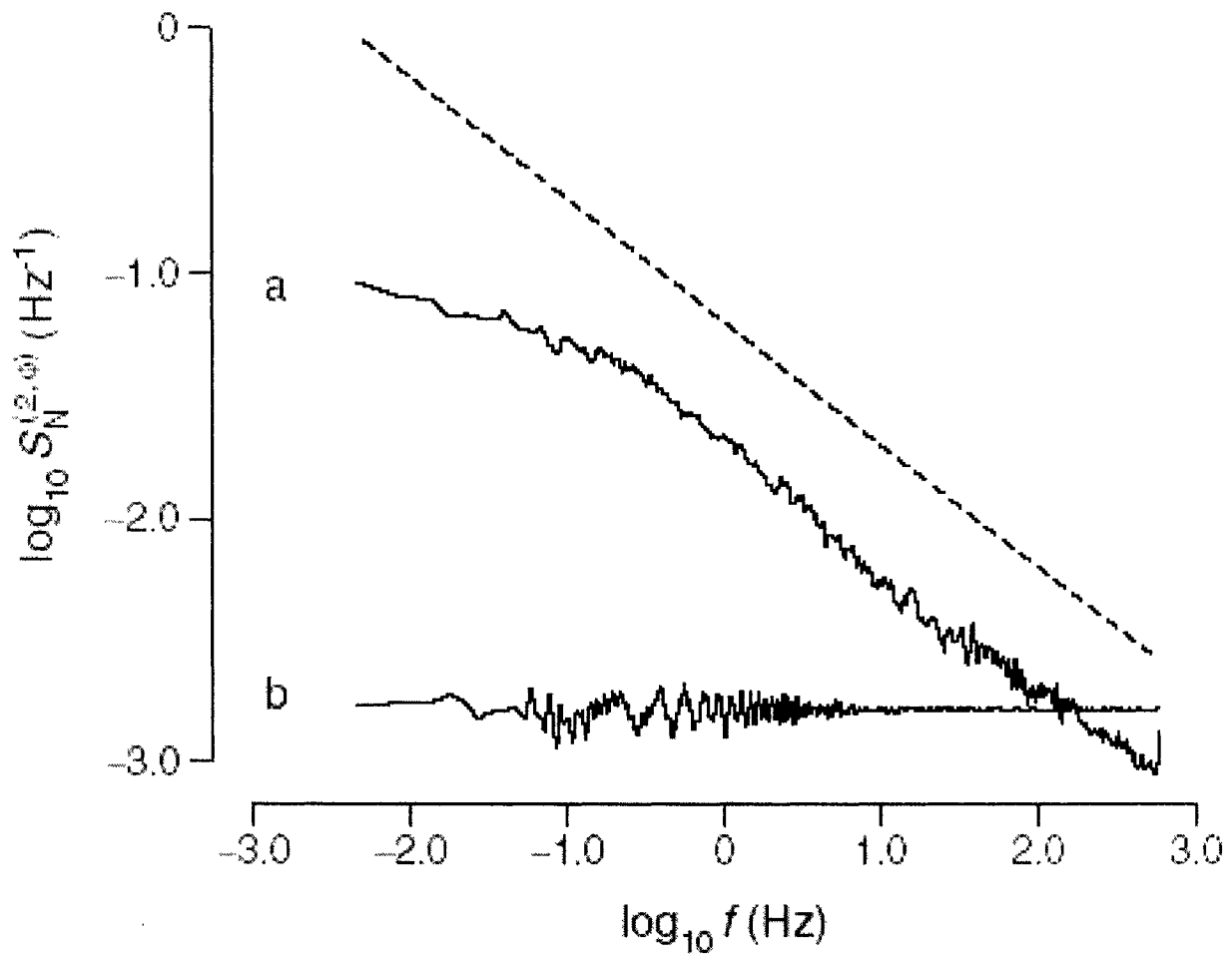
Figure 2.8: (a) Phase-only second spectra for natural auditory noise, phase-only means Gaussian background has been removed. (b) second spectra with the noise order randomized, thus removing all correlations resulting in a flat second spectra. The dotted line is a power law with exponent $-1/2$. Figure obtained from [36].

19
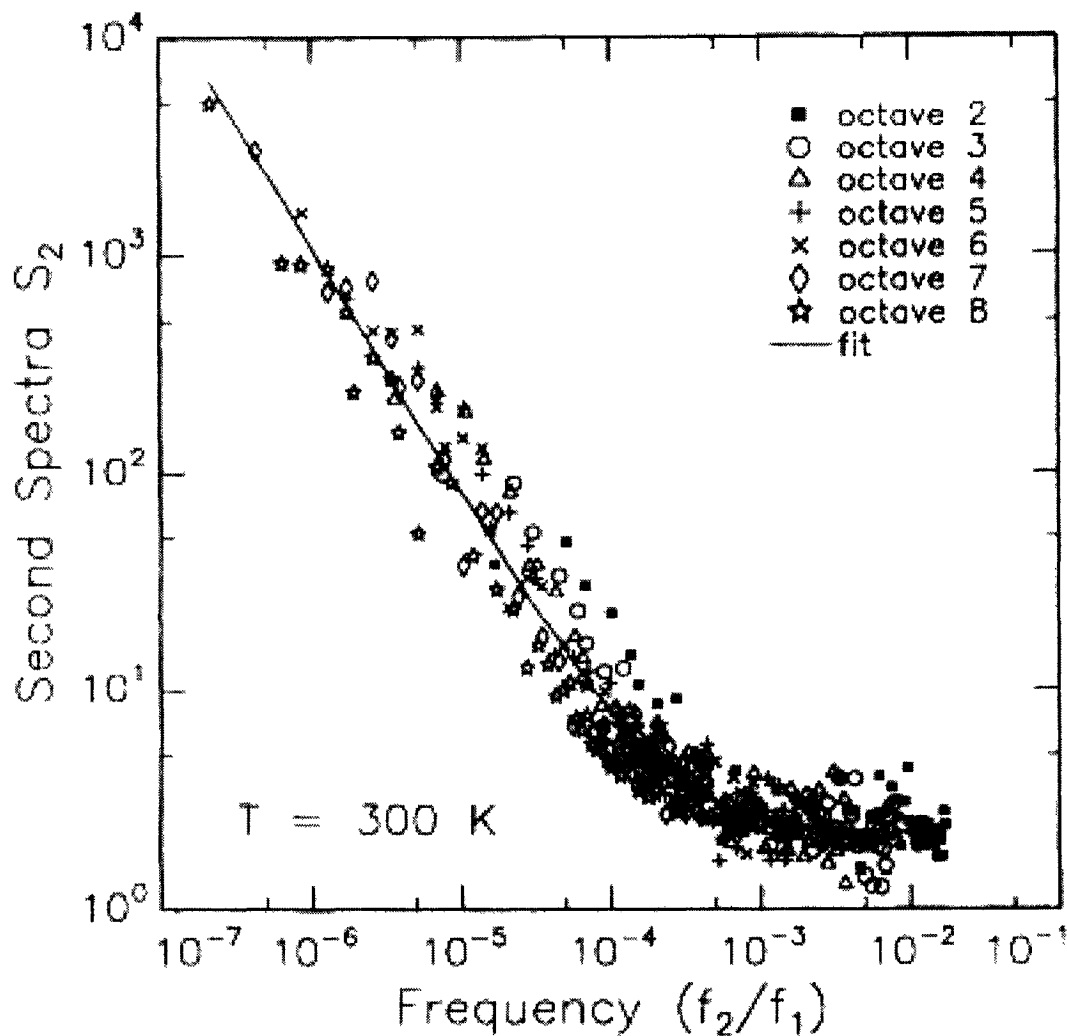
Figure 2.9: Second spectra for noise power of resistance fluctuations in n-type-doped hydrogenated amorphous silicon (a-Si:H) for 7 different frequencies taken from [37]. The fit give a power law exponent of ~ -1.

for the complex dynamics of the resistance fluctuations. It would be of great interest to see if this system may have an underlying critical point?

2.3 Remarks

The experiments and observations discussed in this chapter clearly demonstrate that shape functions and higher order spectra give valuable information about the underlying dynamics of the system in question. Also, we have shown that higher order spectra in particular have a broad range of applicability in a variety of systems, giving information not accessible by the ordinary power

spectra. In the remaining chapters we do a careful study of the shape functions and higher order spectra as they apply to theory, simulation, and experiment. Our purpose is to not only motivate these unique methods of analysis in the context of avalanche models, but to show their overall efficacy as a tool for understanding complex systems.

Chapter 3

Magnet Model

3.1 $T = 0$ Random Field Ising Model

In this thesis we study three variants of the non-equilibrium zero temperature random field Ising model (RFIM), which all predict power law distributions of avalanche sizes and *universal* non-equilibrium collective behavior. The RFIM is a model for a conventional magnet in which magnetic domains are modeled by "spins" on a lattice that can only point up or down. The first variant basically exhibits single front (domain wall) propagation dynamics in which spins at the edge of an existing front flip when it is (locally) energetically favorable to do so. Spins that are not adjacent to this front are very unlikely to flip on their own due to the presence of an infinite-range demagnetizing field, which is present in addition to nearest neighbor ferromagnetic interactions. We call this the infinite range model [13]. In the second variant, called the nucleation model, spins flip anywhere in the system when it is (locally) energetically favorable to do so. In this case there are *many interacting* fronts, unlike in the infinite range model. Only nearest neighbor ferromagnet interactions are included in the nucleation model [51]. The third variant, involves the addition of dipole-dipole interations to the infinite range model. This addition lowers the upper critical dimension of the model to $d = 3$, thus mean field theory becomes exact (up to logarithmic corrections) [13]. In the mean field RFIM every spin interacts with every other spin in the system, and flips with it is energetically favorable to do so.

3.1.1 Infinite Range and Nucleation Model

The RFIM consists of a (hypercubic) lattice of N spins ($s_i = \pm 1$), which may point up ($s_i = +1$) or down ($s_i = -1$). Spins are coupled to nearest neighbors (through a ferromagnetic exchange interaction J), and to an external field $H(t)$ which is increased adiabatically slowly. To model dirt in the material, we assign a random field, h_i, to each spin, chosen from a distribution $P(h_i) = exp(-h_i^2/2R^2)/\sqrt{2\pi}R$, where R, the disorder, determines the width of the Gaussian probability distribution and therefore gives a measure of the amount of quenched disorder for the system. Magnetocrystalline anisotropy, grain boundaries, varying bond strength, dislocations, and vacancies are some potential sources of disorder.

The Hamiltonian for the system at a time t is given by:

23

$$H = \sum_{<ij>} -Js_i s_j - \sum_i (H(t) + h_i - J_{inf}M)s_i, \tag{3.1}$$

where J_{inf} is the strength of the infinite range demagnetizing field ($J_{inf} = 0$ for the nucleation model), $M = \frac{1}{N}\sum_i s_i$ is the magnetization of the system, and $<ij>$ stands for nearest neighbor pairs of spins. Initially, $H(-\infty) = -\infty$ and all the spins are pointing down. Each spin is always aligned with its local effective field:

$$h_i^{eff} = J \sum_{<ij>} s_j + H(t) + h_i - J_{inf}M. \tag{3.2}$$

The infinite range model exhibits self-organized criticality (SOC) [52, 53, 54]. This means that as H is increased the model always operates at the critical depinning point, and no parameters need to be tuned to exhibit critical scaling behavior (except $\frac{dH}{dt} \to 0$). The nucleation model, on the other hand, is a plain old critical system with a continuous second order phase transition with disorder as the tuning parameter. The continuous non-equilibrium phase transition can be understood as follows. For zero disorder, the random fields of each spin will be the same, so that when one spin is flipped the entire lattice of spins will flip. This results in a rectangular hysteresis curve with a macroscopic jump in the magnetization when the external field overcomes the interaction with the neighbors. On the other hand, if the disorder is infinite, each spin will have a very different random field, so as the external field is raised each spin will essentially flip independently, triggering no other spins to flip. This will result in a smooth "hysteresis" curve with an approximately constant slope ($M(H) \sim H$ over a wide range of H). In between these two phases of behavior there is a continuous phase transition at some critical value $R = R_c$. At the transition each branch of the hysteresis loop has a single point with infinite slope ($\frac{dM}{dH}|_{\pm H_c} \to \infty$) at a critical field $H = \pm H_c$. R_c and H_c are nonuniversal. In three dimensions they are: $R_c = 2.16$ and $H_c = 1.43$ (in units of J) [55]. The transition is characterized by a number of universal critical exponents [56], and scaling functions. Details of the simulation algorithm are given elsewhere [57].

24

3.1.2 Mean Field Model

The $T = 0$ mean field RFIM consists of an array of N spins ($s_i = \pm 1$), which may point up ($s_i = +1$) or down ($s_i = -1$). Spins are coupled to all other spins (through a ferromagnetic exchange interaction J), and to an external field $H(t)$ which is increased adiabatically slowly. Just as in the infinite range and nucleation model we model disorder by assigning a random field, h_i, to each spin, chosen from a distribution $P(h_i) = exp(-h_i^2/2R^2)/(\sqrt{2\pi}R)$. The Hamiltonian for the system at a time t is given by:

$$H = - \sum_i (JM + H(t) + h_i)s_i, \qquad (3.3)$$

where $M = \frac{1}{N} \sum_j s_j$ is the magnetization of the system. Initially, $H(-\infty) = -\infty$ and all the spins are pointing down. Each spin is always aligned with its local effective field $h_i^{eff} = JM + H(t) + h_i$. Just as in the nucleation model the mean field RFIM also has a plain old critical point with a continuous phase transition, where $H_c = 0$ and $R_c = \sqrt{\frac{2}{\pi}}$ [11].

3.2 Avalanche Dynamics in the $T = 0$ RFIM

The external field $H(t)$ is adiabatically slowly increased from $-\infty$ until the local field, h_i^{eff}, of any spin s_i changes sign, causing the spin to flip [13, 58]. It takes some microscopic time Δt for a spin to flip ($\Delta t \equiv 1$ for our simulation). The spin flip changes the local field of the nearest neighbors and may cause them to flip as well, etc. This *avalanche* process continues until no more spin flips are triggered. Each step of the avalanche, that is, each Δt in which a set of spins simultaneously flip, is called a *shell*. The number of spins that flip in a shell is directly proportional to the voltage $V(t)$ during the interval Δt that an experimentalist would measure in a pick-up coil wound around the sample. In our simulations we therefore denote the number of spins flipped in a shell at a time t by $n_t (= V(t))$. The first shell of an avalanche (one spin flip) is triggered by the external field $H(t)$, while each subsequent shell within the avalanche is triggered only by the previous shell, since $H(t)$ is kept constant while the avalanche is propagating. $H(t)$ is only increased when the current avalanche has stopped, and is increased only until the next avalanche is triggered (i.e. $\frac{dH}{dt} \to 0$). The number of shells in an avalanche, n_t, times Δt defines the *pulse duration*, T, or the time it

25

took for the entire avalanche to flip. The time series of n_t values for many successive avalanches creates a Barkhausen train analogous to experiment.

3.3 Why Random Fields?

One may ask the question, why study the Random Field Ising Model, instead of the Random Bond Ising Model (RBIM), where the ferromagnetic interaction, J_{ij}, varies from site to site, or the Random Anisotropy Ising Model (RAIM), where each spin takes a random angle so $s_i \cdot s_j$ varies from site to site? Also, how can the inclusion of random fields account for so many potential causes of disorder, such as: dislocations and vacancies, anisotropy, random bond strengths, and grain boundaries? Why would not the RAIM be the best model for materials that have random anisotrophies? Also, why would not the RBIM be the best model for materials that have random bond strengths?

It turns out as far as critical behavior is concerned the RFIM gives the same universal exponents and universal scaling functions as the RBIM and the RAIM, since they are in the same universality class! The presence of the external driving field $H(t)$ breaks the rotational symmetry of the RFIM and RBIM, and breaks the time reversal symmetry of the RBIM and RAIM. Therefore all three models are in the same universality class since they share the same symmetries. We choose to study the RFIM since it is the fastest and most convenient to simulate [57]. Also, since the three models have the same critical behavior, the random fields effectively capture various sources of disorder present in real materials (with regards to critical behavior).

26

Chapter 4

Earthquake Model

Recently enough data have been collected to extract statistics of earthquakes on individual fault zones occupying long (order 100 km) and narrow (order 10 km) regions of space. Wesnousky and collaborators [28, 29] found that the frequency-size statistics of earthquakes on highly irregular fault zones, with many offsets and branches, as the San Jacinto fault in California, are also described by the Gutenberg-Richter power law relation up to the largest events. However, relatively regular fault zones (presumably generated progressively with increasing accumulated slip over time), such as the San Andreas fault in California, display power-law frequency-size statistics only for small events. These occur in the time intervals between roughly quasi-periodic earthquakes of a much larger "characteristic" size that is related to large-scale dimensions of the fault zone [23, 28, 47, 59]. (If the ratio of the mean divided by the standard deviation of the distribution of time intervals between characteristic earthquakes is larger than 1, the distribution is referred to as quasi-periodic [59]). Earthquakes of intermediate magnitude are typically not observed on these faults (other than, perhaps, during aftershock sequences). The corresponding frequency size statistics are called the "characteristic earthquake" distribution.

Previously these two types of behavior on individual fault zones have been modeled as statistics close-to and far-from an underlying critical point [60, 61], using a model for a strike-slip fault that incorporates long-range interaction and strong heterogeneities [47, 59]. The different dynamic regimes were associated with competition between failure-promoting effects of elastic stress-transfer or dynamic weakening, and the opposing effect of strength inhomogeneities in the fault structure. Fisher et al. [60] found that near the critical point the frequency-size statistics follow a power law distribution (with a cutoff at large magnitude), with the same scaling exponent of observed data for strike-slip faults (i.e., a b-value of 0.75). A similar form of frequency-size statistics and predicted b-value were obtained also for a critical parameter value in a stochastic branching model [62].

In this chapter we review and extend the model, the phase diagram for the model dynamics, and the scaling behavior on long length scales.

4.1 Ben-Zion and Rice Earthquake Model

The model we use was developed originally by Ben-Zion and Rice [47, 59], who suggested that a narrow irregular strike-slip fault zone of horizontal length L and vertical depth W may be repre-

sented by an array of $N \sim LW$ cells in a two dimensional plane, with constitutive parameters that vary from cell to cell to model the disorder (offsets etc.) of the fault zone structure (FIG. 4.1). The cells represent brittle patches on the interface between two tectonic blocks that move with slow transverse velocity v in the x direction at a great distance from the fault. The interaction between cells during slip events is governed by 3-D elasticity and falls with distance r from the failure zone as $\frac{1}{r^3}$. These interactions are sufficiently long range that scaling in mean field theory (where the interaction range is set to infinity) becomes exact, up to logarithmic corrections, in the physical fault dimension ($d = 2$) [47, 59, 60]. In mean field theory, the local stress τ_i on a given cell i is [47]:

$$\tau_i = J/N \sum_j (u_j - u_i) + K_L(vt - u_i) \tag{4.1}$$

$$= J\bar{u} + K_L vt - (K_L + J)u_i \tag{4.2}$$

where u_i is the total offset of cell in the horizontal x direction, $\bar{u} = \sum_j u_j/N$ is the average displacement, J/N is the mean-field elastic coupling strength between cells, and $K_L \sim 1/\sqrt{N}$ is the loading stiffness [61] of the tectonic blocks that move far away from the fault with relative velocity v. Initially the stresses τ_i are randomly distributed with $\tau_{a,i} \leq \tau_i \leq \tau_{s,i}$, where $\tau_{s,i}$ is a fixed local static failure threshold stress and $\tau_{a,i}$ is the fixed local arrest stress. The distributions of static failure stresses and arrest stresses represent the heterogeneity or geometrical disorder in the fault system. The differences between the failure and arrest stresses give the local distribution of stress drops during brittle failures; the earthquake dynamics depend only on the stress drop distribution (no stochasticity). In addition, the scaling behavior of the system is not sensitive to the exact form of the distributions as long as they are bounded and $\tau_{a,i} < \tau_{s,i}$. We choose a compact distribution for $\tau_{a,i}$, such that $p(\tau_{a,i}) = 3(W^2 - 4\tau_{a,i}^2)/(2W^3)$ for $-W/2 \leq \tau_{a,i} \leq W/2$ and 0 outside of these bounds. Also, we look at the low disorder limit where $W \ll \tau_{s,i}$, where we choose $\tau_{s,i} = 1$, so all cells will fail at this point.

The fault is stuck while the stress on each cell is increased uniformly as $d\tau_i/dt = K_L v$ as a result of the external loading which is increased adiabatically (that is, we take the limit $v \to 0$). When the stress on a cell reaches its failure threshold $\tau_{s,i}$, the cell slips by the amount:

29
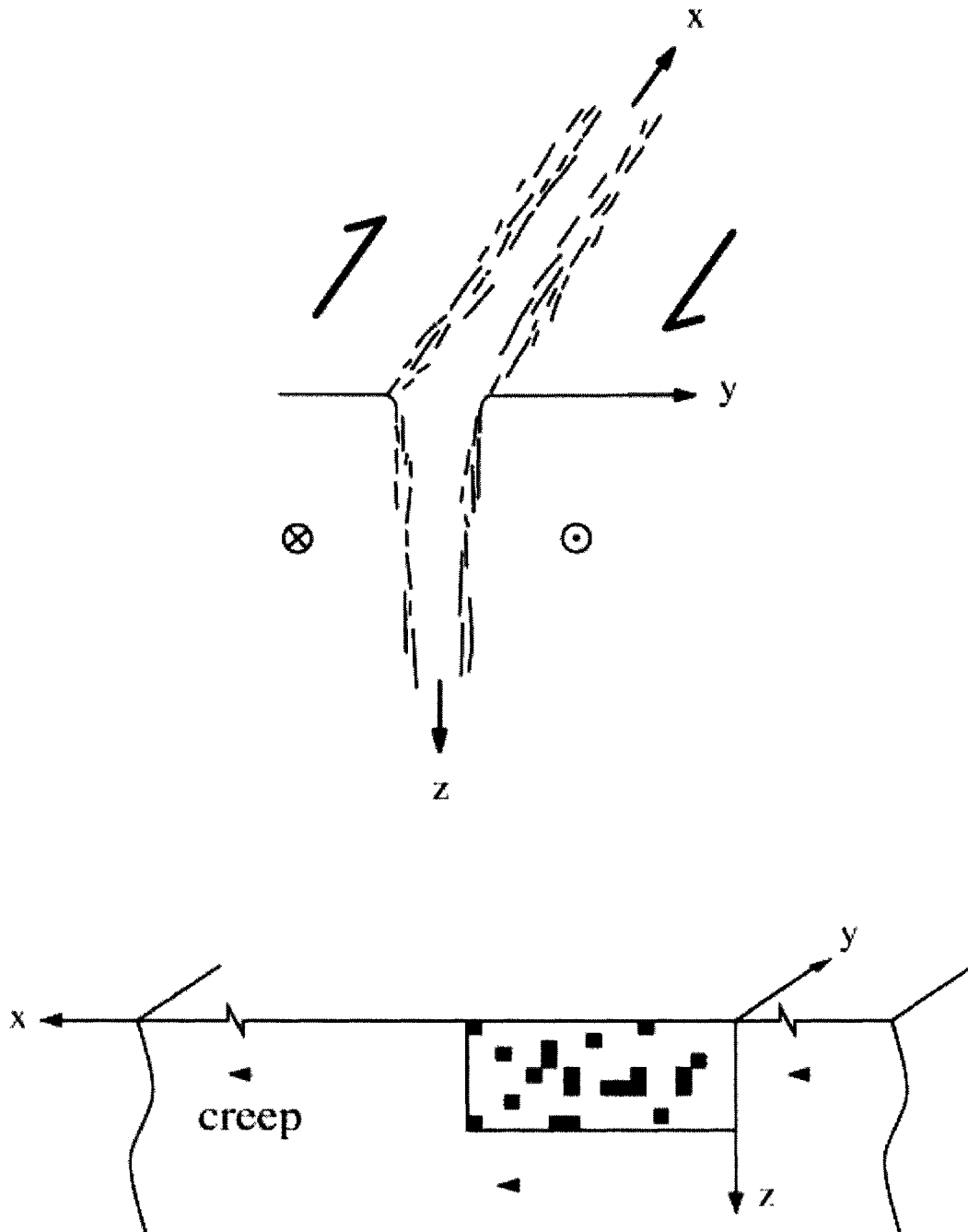
Figure 4.1: A planar representation of a 3-D segmented fault zone by a 2-D heterogeneous fault embedded in a 3-D solid [47, 59].

30

$$\Delta u_i = (\tau_{s,i} - \tau_{a,i})/(K_L + J). \tag{4.3}$$

This stress drop is uniformly redistributed to all other cells (employed in the mean field approximation) by an amount:

$$\delta\tau_j = (c/N)(\tau_{s,i} - \tau_{a,i}), j \neq i \tag{4.4}$$

Where $c \equiv J/(K_L + J)$, is the conservation parameter, that gives that fraction of stress drop of a cell that is retained in the system after it slips [61]. The resulting stress increase on the other cells can cause some of them to slip as well, leading to an avalanche of cell slips, or an earthquake.

4.2 Dynamical Weakening and Strengthening

The model includes dynamic weakening effects during the failure process [47, 59]: after an initial slip in an earthquake, the strength of a failed cell is reduced to a *dynamical* value:

$$\tau_{d,i} \equiv \tau_{s,i} - \epsilon(\tau_{s,i} - \tau_{a,i}), \tag{4.5}$$

with $0 \leq \epsilon \leq 1$ parameterizing the relative importance of dynamical weakening effects in the system. This weakening represents the transition from static friction to dynamic friction during the rupture and the strength of a failed cell remains at the dynamic value throughout the remainder of the earthquake. In the time intervals between earthquakes all failure thresholds heal back to their static value $\tau_{s,i}$. Fisher et al. [60] found that at exactly $\epsilon = 0$ the model produces a power law distribution of earthquake moments M_0 following equation (1.1), cutoff by the finite fault size, with an analytical exponent $\beta = 1/2$ (FIG. 4.2). This corresponds to a b-value of 0.75, close to that associated with observed earthquakes on strike-slip faults [26]. The power law scaling of the frequency-size statistics and other variables [60] indicates that the model with $\epsilon = 0$ operates at a critical point. In contrast, for a finite weakening $\epsilon > 0$ the model produces the characteristic earthquake distribution, with power law statistics for the small events up to a cutoff moment that scales like:

31
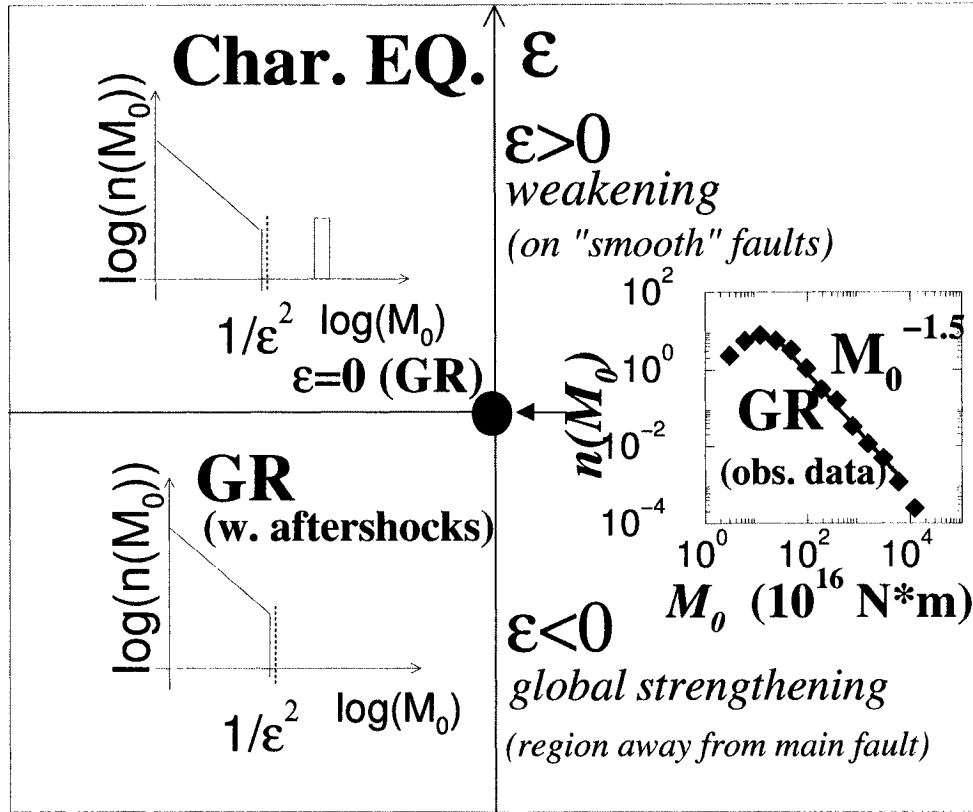
Figure 4.2: Phase diagram of the model (see text and [61] for details).

$$M_0^{cutoff} \sim 1/\epsilon^2, \tag{4.6}$$

and quasi-periodically recurring large characteristic events that scale with the fault size ($M_0 \sim N^{3/2}$).

The model can be expanded further to include dynamic strengthening represented by $\epsilon < 0$. Ben-Zion and Sammis [63] summarized multidisciplinary observations which indicate that brittle failure of rock has an initial transient phase associated with strain hardening rheology, distributed deformation, and continual creation of new structures. Thus $\epsilon < 0$ corresponds physically to regions off the main fault segments that are in an early deformation stage. To capture basic aspects of brittle deformation on such regions in the three-dimensional volume around the main fault (FIG. 4.1), we change the model as follows: when any cell i slips during an earthquake, and thereby

32

reduces its stress by $\Delta\tau_i \equiv \tau_{f,i} - \tau_{a,i}$ the failure stress $\tau_{f,j}$ of *every* cell $j = 1,...,N$ is *strengthened* by an amount $|\epsilon|\Delta\tau_i/N$. Once the earthquake is complete the failure stress of each cell is slowly lowered back to its original value. This represents in a simple way the brittle deformation that occurs during an earthquake in the off-fault regions, which are first in a strengthening regime and then have a weakening process. The events that are triggered as the failure stresses are lowered in the weakening period are referred to as *aftershocks*. The occurrence of aftershocks in this version of the model for off-fault regions is in agreement with the observation that a large fraction of observed aftershocks typically occur in off fault regions [64]. For this version of the model with $\epsilon < 0$, both the primary earthquakes (i.e., main shocks) and the triggered aftershocks are distributed according to the Gutenberg-Richter distribution, up to a cutoff moment scaling as $1/\epsilon^2$. Assuming that the increased failure stress thresholds $\tau_{f,i}$ are slowly lowered with time as $log(t)$ towards their earlier static values $\tau_{s,i}$, and that the stresses are distributed over a wide range of values, in Appendix D we show analytically that the temporal decay of aftershock rates at long times is proportional to $1/t$, as in the modified Omori law of Eq. (1.3) with $p = 1$ [21, 22].

Remarkably, the long length scale behavior of this model can be shown to be the same as the behavior of the model given in Eq. (4.2) with an added "antiferroelastic" term $(-|\epsilon|J\bar{u})$:

$$\tau_i = J\bar{u} + K_L vt - (K_L + J)u_i - |\epsilon|J\bar{u} \tag{4.7}$$

In Eq. (4.7) every time a cell fails, its slip Δu_i leads to stress loading of the other cells, lessened by $|\epsilon|J\Delta u_i/N$ compared to our original model (Eq. (4.2)). On the other hand, in the global strengthening model (described above) when a cell slips the failure stresses of all cells are strengthened by $|\epsilon|J\Delta u_i/N$. On long length scales the global strengthening of the failure stress has equivalent effects on the earthquake statistics as the dissipation of the redistributed stress, up to corrections of order $O(1/N)$, so the scaling behavior for large events of both models are the same. Moreover, Eq. (4.7) can be rewritten as:

$$\tau_i = J[1 - |\epsilon|][\bar{u} - u_i] + K_L vt - [K_L + J|\epsilon|]u_i \tag{4.8}$$

We can now absorb $|\epsilon|$ by defining $J' = J(1 - |\epsilon|)$ and $K_L' = K_L + J|\epsilon|$. Now rewriting Eq. (4.8)

33

with the new definitions, and dropping the $|\epsilon|$ contribution in $[K'_L - J|\epsilon|]vt$ since $v \to 0$, we find:

$$\tau_i = J'\bar{u} + K'_L vt - (K'_L + J')u_i \tag{4.9}$$

Therefore we recover Eq. (4.2) with $J \to J'$ and $K_L \to K'_L$. This amounts to changing the stress conservation parameter c (from reference [61]). For Eq. (4.9):

$$c = J'/(K'_L + J') = 1 - |\epsilon| \tag{4.10}$$

Where $K_L \to 0$, since we are concerned with the adiabatic limit. Since we also know (from reference [61]) that the cutoff S_{cf} for the Gutenberg-Richter distribution scales as: $S_{cf} \sim 1/(1-c)^2$. Thus, from Eq. (4.10) we find that the cutoff for Eq. (4.7) will scale as $\sim 1/|\epsilon|^2$.

4.3   Mapping to Single Interface Magnet Model

The mean field version of the single interface magnet model with infinite range antiferromagnetic interactions is given by [43, 65]:

$$\dot{h}_i(t) = J[\bar{h} - h_i(t)] + H(t) - k\bar{h} + \eta_i(h) \tag{4.11}$$

Where $h_i(t)$ is the position of the domain wall, $H(t)$ is the external driving field, k is the coefficient of the antiferromagnetic term, and $\eta_i(h)$ is the pinning field. In the paper by Fisher et. al [27] it has been shown that the scaling behavior on long length scales resulting from Eq. (4.7), without the $-|\epsilon|J\bar{u}$ term, is same as that of Eq. (4.11) without the antiferromagnetic term, $-k\bar{h}$. Furthermore, upon inspection we see the following correspondence between the single interface magnet model (Eq. (4.11)), and the mean field earthquake model (Eq. (4.7)):

$$-k\bar{h} \Longleftrightarrow -|\epsilon|J\bar{u} \tag{4.12}$$

In other words the coefficient of the antiferromagnetic term k, plays the same role in the magnet model (Eq. (4.11)), as the coefficient of strengthening $|\epsilon|J$ does in the earthquake model (Eq. (4.7)).

34

4.4 Phase Diagrams

The regimes with various statistics produced by the model are summarized by the phase diagram given in FIG. 4.2. The range $\epsilon > 0$ corresponds to "mature" localized faults with a weakening rheology and characteristic earthquake statistics. The value $\epsilon = 0$ corresponds to "immature" strongly inhomogeneous fault zones with Gutenberg-Richter statistics. Finally, the range $\epsilon < 0$ corresponds to the fracture network away from the main fault, characterized by strengthening due to the creation of new structures and associated emerging aftershocks. It may be surprising that the discussed simple model can capture many of the essential general features of earthquake statistics (or other systems with avalanches, such as driven magnetic domain walls). This can be understood through the renormalization group [1, 66], a powerful mathematical tool to coarse grain a system and extract its effective behavior on long space-time scales. Many microscopic details of a system are averaged out under coarse graining, and universal aspects of the behavior on long scales depend only on a few basic properties such as symmetries, dimensions, range of interactions, weakening/strengthening, etc. When a model correctly captures those basic features, the results provide proper predictions for statistics, critical exponents, and universal scaling functions near the critical point. Consequently, many models that are in the same universality class lead to the same statistics and exponents [1, 60, 61, 66]. The universal scaling functions around the critical point, discussed in the next section, provide additional information that can be used to distinguish between different models and universality classes.

35

Chapter 5

Universal Scaling Functions

In this chapter we perform a detailed quantitative comparison of the universal avalanche pulse shapes and exponents obtained from: the infinite range model, the nucleation model, and various experiments. Our analysis constitutes a test of whether the non-equilibrium zero-temperature RFIM (either the infinite range model or the domain nucleation model) is in the same universality class as experimental systems exhibiting Barkhausen noise.

5.1 The Experiments

In addition to examining results obtained from simulation we study results from three different experiments. Andy Mills and Mike Weissman at UIUC performed one of these experiments, since we analyzed this experiment in collaboration it is referred to as "our" experiment in the following context. The results for the other two experiments were obtained from already published results [42, 43].

Our own experiment was performed on an (unstressed) amorphous alloy, $Fe_{21}Co_{64}B_{15}$. The data we present from Durin et al [43] is from an experiment on an amorphous alloy with a different composition, $Fe_{64}Co_{21}B_{15}$, under a tensile stress. Studies of the effect of tensile stress on samples of this type indicate that for low tensile stress, the domain structure is a complicated pattern of maze domains, dominated by quenched-in stresses [44]. On the other hand, when such materials undergo tensile stress, the uniaxial anisotropy gives way to a simpler domain structure with a few parallel domains in the direction of the stress [44]. Related to this change in domain structure is a change in the dominant interaction in the material. In amorphous alloys under stress, surface tension effects are thought to be more important than dipolar interactions, while dipolar interactions dominate for polycrystals and materials with small grains [14].

Durin et al's sample was under stress so as to enhance stress-induced anisotropy so much that the long range dipolar interactions can be neglected, placing their experiment into the universality class of the infinite range model (introduced in chapter 3) [14, 15, 16]. Spasojević et al's sample was a quasi-two-dimensional metal glass, more precisely a commercial VITROVAC 6025 X [42]. Based on the scaling exponents obtained from Spasojević et al's experiment (given later), their experiment does not seem to fall into any universality class discussed in this thesis. Our experiment seems to be in a crossover regime between two universality classes; details are given later in this chapter.

37

Further details about Durin et al's, and Spasojević et al's experiment can be obtained elsewhere [14, 42, 43, 44].

5.2 Extracting Pulse Shapes

5.2.1 Nucleation Model

We simulate four realizations of a 1200^3 system near $R = R_c$ ($R = 2.2$) and record the time series $V(t,T)$ of avalanches from an H window near H_c ($1.42 < H < 1.43$). We average $V(t,T)$ for avalanches of a fixed pulse duration T (within the interval $[T, 1.05T]$), for various values of T. In each case we average over 1000 to 2000 avalanches to ensure strong fluctuations have been averaged out. We check finite size effects by performing simulations at 800^3 and 1000^3 and verifying that identical avalanche shapes (within small fluctuations) are obtained for all system sizes.

5.2.2 Infinite Range Model

We perform 100 realizations of a 400^3 system and record avalanches from an H window within the slated part of the hysteresis loop ($1.25 < H < 1.88$). Even though the infinite range model exhibits SOC due to the infinite range demagnetizing interaction, in order to avoid effects due to initial nucleation of the front (beginning of the hysteresis loop), or when the front encounters the boundaries of the simulation (the end of the hysteresis loop) we must choose avalanches near the middle of the hysteresis loop. We obtain avalanche shapes $V(t,T)$ in a manner identical to how they were obtained for the nucleation model. We check finite size effects by performing simulations of 200^3 and 300^3 size systems, and find a consistent avalanche shape for all three system sizes.

5.2.3 Experiment

Measurements were performed on a 21 cm x 1 cm x 30 μm ribbon of $Fe_{21}Co_{64}B_{15}$ alloy, a soft amorphous ferromagnet obtained from Gianfranco Durin. The domain walls run parallel to the long axis of the material, with about 50 domains across the width. A solenoid, driven with a triangle wave, applies a magnetic field along the long axis of the sample. Since domain wall motion dominates over other means of magnetization in the linear region of the loop, data were collected

38

in only a selected range of applied fields near the center of the loop. The Barkhausen noise was measured by a small pick-up coil wound around the center of the sample. This voltage signal was amplified, anti-alias filtered and digitized, with care taken to avoid pick-up from ambient fields. Barkhausen noise was collected for both increasing and decreasing fields for 80 cycles of the applied field through a saturation hysteresis loop. The driving frequency was 0.01 Hz; this corresponds to $c = 0.09$, where c is a dimensionless parameter proportional to the applied field rate and is defined in the Alessandro Beatrice Bertotti Montorsi model (ABBM model) for the Barkhausen effect [17]. In this way, our measurements should be well inside the $c < 1$ regime identified in the ABBM model, in which we can expect to find separable avalanches rather than continuous domain wall motion. Also, the ABBM model is directly related to the infinite range model, since the infinite range model projected onto 1D is equivalent to the ABBM model [54].

Due to background noise in real experimental data there is no definitive way to determine when an avalanche begins and when one ends; we set a sensitivity threshold which is high enough to cut out background noise and low enough to capture enough of the avalanche so as not to affect the shape. We check the validity of our threshold by perturbing the threshold by a small amount and noticing that there is no change in the avalanche shape.

5.3   Critical Exponents and Data Collapses

In the infinite range model, as well as in the nucleation model near (R_c, H_c), the voltage $V(T, t)$ scales as [13]:

$$V(T,t) = T^{1/\sigma\nu z - 1} f_{shape}(t/T) \tag{5.1}$$

By collapsing average avalanche shapes of various durations T we determine the universal scaling function, $f_{shape}(t/T)$, and the critical exponent $1/\sigma\nu z$. The exponent $1/\sigma\nu z$ relates the avalanche size, S, to the avalanche pulse duration, T, at criticality by $S \sim T^{1/\sigma\nu z}$. We find that the critical exponent $1/\sigma\nu z$ for the infinite range and nucleation model, obtained from simulation, is in close agreement with previous theoretical predictions and with experimental values [11]. The collapses are shown in Figs. 5.1 and 5.2.

39
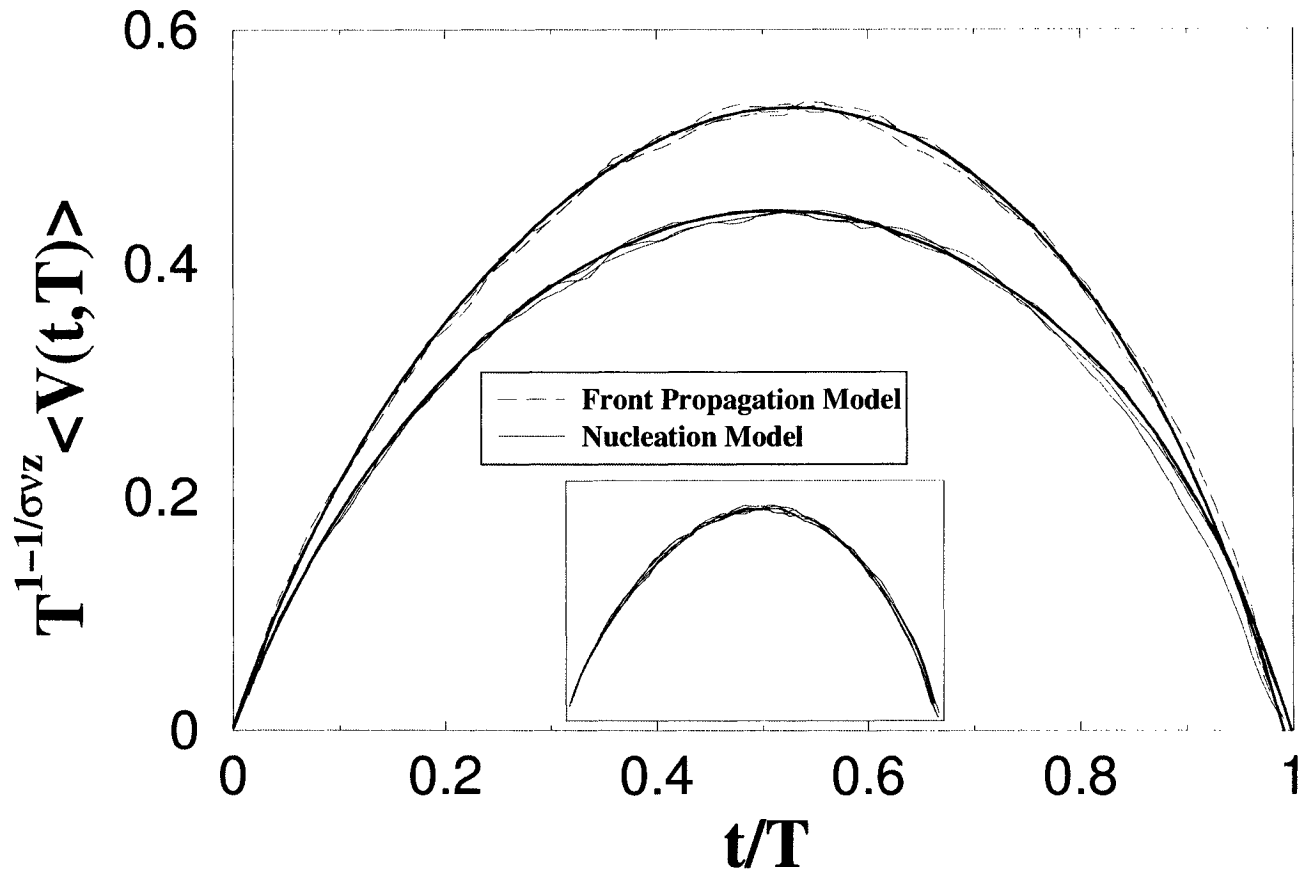
Figure 5.1: Pulse shape collapses of $V(t, T)$ (the number of spins flipping in each time step) obtained from simulation. Three pulse shapes were collapsed for each model; these pulse shapes represent averaged avalanches of pulse durations $T = 52$, 73, and 106 (total number of time steps) within 5%. From the collapse of infinite range model avalanche pulse shapes, we find $1/\sigma\nu z = 1.72 \pm 0.03$. From the collapse of nucleation model avalanche pulse shapes, we find $1/\sigma\nu z = 1.75 \pm 0.03$. The bold line going through the collapses is the non-linear curve fit obtained from the set of orthonormal polynomials presented in this chapter (Eqns. (5.2)-(5.6)). Note that the non-linear curve fit is shown for only one of the collapsed averaged avalanches in each case. Inset: By rescaling the height of the nucleation model collapse by 20% we obtain a collapse of pulse shapes from the two different models suggesting that their pulse shapes are very similar, but quantitatively not the same as described in the text.

40
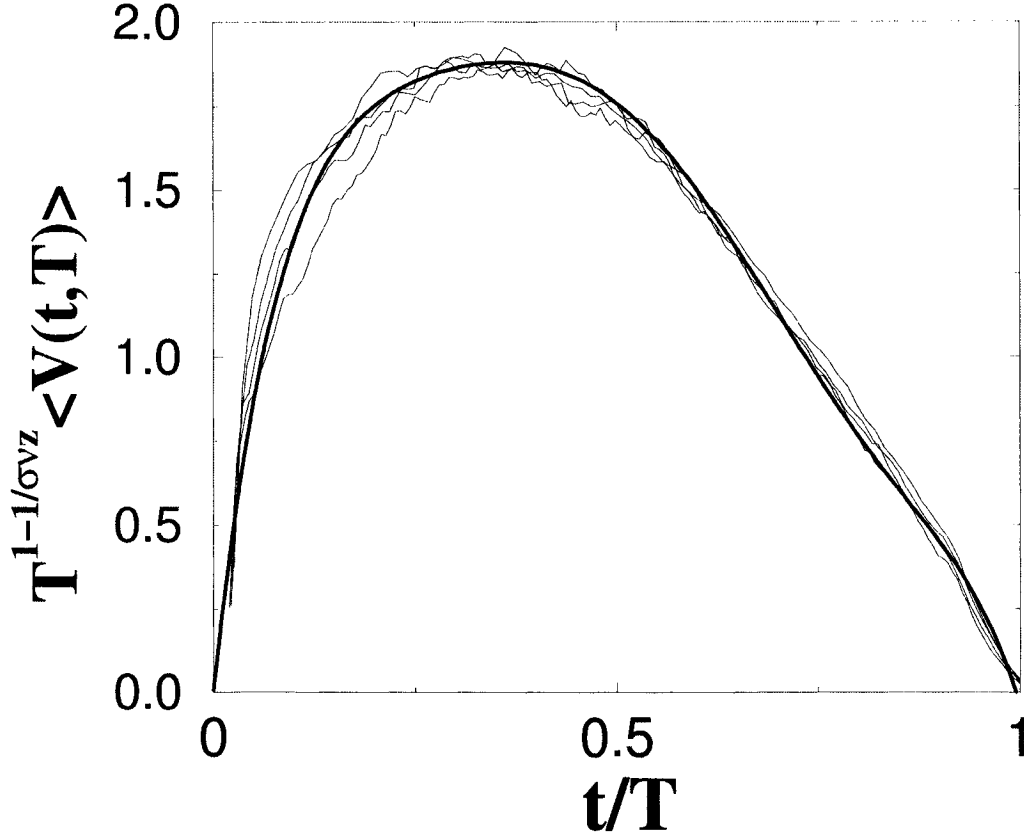
Figure 5.2: Collapse of averaged experimental avalanche pulse shapes $< V(t,T) >$ (in units of 0.316 mV) is shown, yielding $1/\sigma\nu z = 1.70 \pm 0.05$. The four curves represent averaged avalanches of pulse duration: $T = 88t_o$, $110t_o$, $132t_o$, and $165t_o$ within 10%, where $t_o = 6.4\mu s$ represents the time between each measurement of the Barkhausen noise train. Each of the four curves is an average of between 1152 to 1561 avalanches. The smooth bold curve is a fit of the averaged avalanche of duration $T = 132t_o$ using the orthonormal polynomials given in Eqns. (5.2)-(5.6). Inset: Pulse duration distribution, $D(T)$ (number of pulses of duration T), obtained from our experiment. Avalanche pulse shapes were extracted from the region indicated by the arrows, and this region is well within the scaling regime. In this scaling regime $D(T)$ scales as $D(T) \sim T^{-\alpha}$ where $\alpha = 1.74 \pm 0.06$. This value of α is between the mean field value of $\alpha = 2.0$ (sample without stress) and the value of $\alpha = 1.5$ for infinite range dynamics (sample with stress) [14], indicating that our experiment may be in a crossover regime.

41

We also determine the avalanche size distribution that scales as $D(S) \sim S^{-\tau}$ at criticality. The avalanche size distributions for our simulation and our experiment are given in Fig. 5.3; the values obtained for τ, for the infinite range model and nucleation model, are in close agreement with previously quoted values [13, 55]. Experimentally, the scaling exponent τ weakly depends on c in some materials [44]. From this dependence we find that there may be a difference of 0.02 between the value of τ we find in our experiment and the value of τ at $c = 0$ (zero frequency). However, this difference is within the error bars we give for τ. Table 5.1 summarizes results for τ and $1/\sigma \nu z$ for experiment, simulation, and mean field theory. We see that the critical exponents for the infinite range model agree (within error bars) with exponents from Durin et al's experiment, as expected.

While Durin et al's experiment is believed to fall into the infinite range universality class, as discussed above, our experiment is neither in the infinite range nor in the mean field universality class. A priori we would assume that our experiment would be in the mean field universality class since our sample was unstressed, and previous experiments have indicated that unstressed samples will exhibit mean field behavior [14]. The critical exponents found from our experiment indicate that it maybe in a crossover regime between the mean field and the infinite range universality classes. The exponent τ has a value of 1.46 ± 0.05 (see also Table 5.1), which is between the value of 1.28 for the infinite range model (sample with stress) and the mean field value of 1.5 (sample without stress) [13, 14]. In addition, the exponent $\alpha = 1.74 \pm 0.06$, determined from the avalanche pulse duration distribution given by $D(T) \sim T^{-\alpha}$ at criticality, (see Inset of Fig. 5.2), is between the value of 1.5 for the infinite range model (with stress), and the mean field value of 2 (without stress) [43]. Residual stress on our sample may have resulted in these anomalous exponents.

Although our experiment may be in a crossover regime, we were able to obtain a good collapse of the avalanche pulse shapes (see Fig. 5.2). In order to reaffirm the validity of the exponent obtained from the collapse, we independently checked the value of $1/\sigma \nu z$ from the power spectra ($P(w) \sim w^{-1/\sigma \nu z}$ at criticality), and found $1/\sigma \nu z = 1.73 \pm 0.08$, which is consistent (within errors bars) with $1/\sigma \nu z = 1.70 \pm 0.05$ obtained from the experimental avalanche pulse collapse.

42
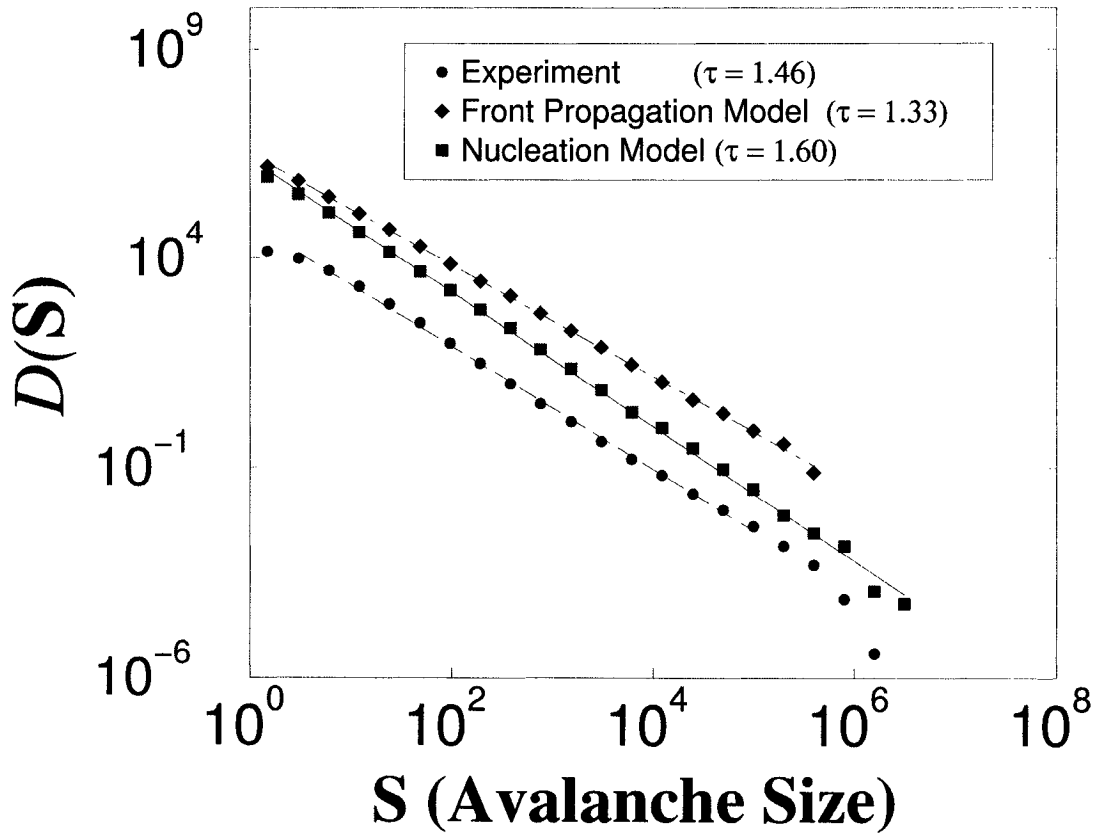
Figure 5.3: Avalanche size distribution, $D(S)$ (number of avalanches of size S), for the infinite range model, the nucleation model, and our experiment. The exponent τ given in the legend is the critical exponent corresponding to the scaling of the avalanche size distribution ($D(S) \sim S^{-\tau}$). For experiment S is given in units of 2.022 mV·μs, for simulation S is the total number of spins flipped in an avalanche.

43

	Nucleation Model	Infinite Range Model	Our Experiment Durin et al's Expt.[†] Spasojević et al's Expt.[*]	Mean Field [57]
τ	1.60 ± 0.04 1.60 ± 0.06[55]	1.33 ± 0.08 1.28[57]	1.46 ± 0.05 1.27 ± 0.03[†][14, 15] 1.77[*][42]	1.5
$1/\sigma\nu z$	1.75 ± 0.03 1.75 ± 0.07[55]	1.72 ± 0.03 1.72[57]	1.70 ± 0.05 1.77 ± 0.12[†] [14, 43] 1.58[*][42]	2

Table 5.1: In the above table we present the critical exponents τ and $1/\sigma\nu z$ in $d = 3$ dimensions for the nucleation model, infinite range model, and all three experiments discussed in this chapter. We also include the mean field values of these exponents.

5.4 Fitting to Orthonormal Polynomials

The mean field shape of avalanches in our model $V^{MFT}(t, T)$ is an inverted parabola [67]. In order to study corrections to the mean field shape, in simulation and experiment, in Appendix B we derive a set of orthonormal polynomials $f_i(t)$ with $f_i(-L) = f_i(L) = 0$, where $L = T/2$ is half the duration of the avalanche. The negative of the first polynomial, $f_0(t)$, is proportional to the mean field result. The first five polynomials of the set are:

$$f_0(t) = \sqrt{\frac{15}{16L^5}}(t^2 - L^2) \tag{5.2}$$

$$f_1(t) = \sqrt{\frac{105}{16L^7}}(t^3 - L^2 t) \tag{5.3}$$

$$f_2(t) = \sqrt{\frac{45}{64L^9}}(7t^4 - 8L^2 t^2 + L^4) \tag{5.4}$$

$$f_3(t) = \sqrt{\frac{1155}{64L^{11}}}(3t^5 - 4L^2 t^3 + L^4 t) \tag{5.5}$$

$$f_4(t) = \sqrt{\frac{1365}{2048L^{13}}}(33t^6 - 51L^2 t^4 + 19L^4 t^2 - L^6) \tag{5.6}$$

We fit a linear combination of the above polynomials to the average avalanche shape obtained from simulation and experiment. L is also left as a free parameter in the fits to the average shapes. The pulse duration is then precisely defined as $T = 2L$. The results of the fits are shown in Fig. 5.1 and Fig. 5.2. In Fig. 5.4 we give the coefficients for the fits, found in simulation and experiment. We also include the coefficients for the fit to an average avalanche shape determined by Durin et

44

al's experiment [43], whose avalanche shape is given in Fig. 5.5. The coefficients are determined from the total fit function:

$$F(t) = a_0 f_0(t) + a_1 f_1(t) + a_2 f_2(t) + a_3 f_3(t) + a_4 f_4(t) \tag{5.7}$$

a_0, a_2, and a_4 are the *symmetric* coefficients of the fit, while a_1, a_3 are the *antisymmetric* coefficients of the fit (i.e. multiplying polynomials that are not symmetric under time reversal $t \rightarrow -t$). We are particularly interested in the asymmetry of the avalanche shapes.

From inspection of the avalanche shapes we see that the experimental avalanche shapes are strongly asymmetric under time reversal, while the avalanche shapes determined from the simulation of the two models are both very close to symmetric. Theoretical calculations predict a symmetric avalanche shape in mean field theory [67], also the ABBM model predicts a symmetric sine function for the avalanche shape [19].

Quantitatively, the coefficients for the avalanche shapes of the nucleation model are very similar to those of the infinite range model and both are different from the experimental avalanche shapes' coefficients. While avalanche shapes in both models are slightly asymmetric to the left (i.e. $V(t,T)$ increases more slowly than it decreases), the experimental avalanche shapes are strongly asymmetric to the right direction (i.e. $V(t,T)$ increases quickly and decreases slowly). The origin of this difference between theory and experiment is not yet understood. It comes as a surprise, since the critical exponents obtained in Durin et al's experiment are in close agreement with exponents obtained from the infinite range model (see Table 5.1) and the avalanche shapes are expected to be just as universal as the critical exponents. On the other hand, we see in Fig. 5.5 that different experiments give different pulse shape scaling functions. This difference may be a result of the fact that the experiments are not in the same universality class. Nevertheless, all the experimental pulse shapes do have the same sign of asymmetry.

We did one check on whether the pulse shape function in our model is indeed *universal*, an assumption often taken for granted: We changed the lattice of our simulation from a simple cubic to a BCC (body centered cubic) lattice and found an identical pulse shape scaling function (within small statistical error), as expected when universality holds.

45
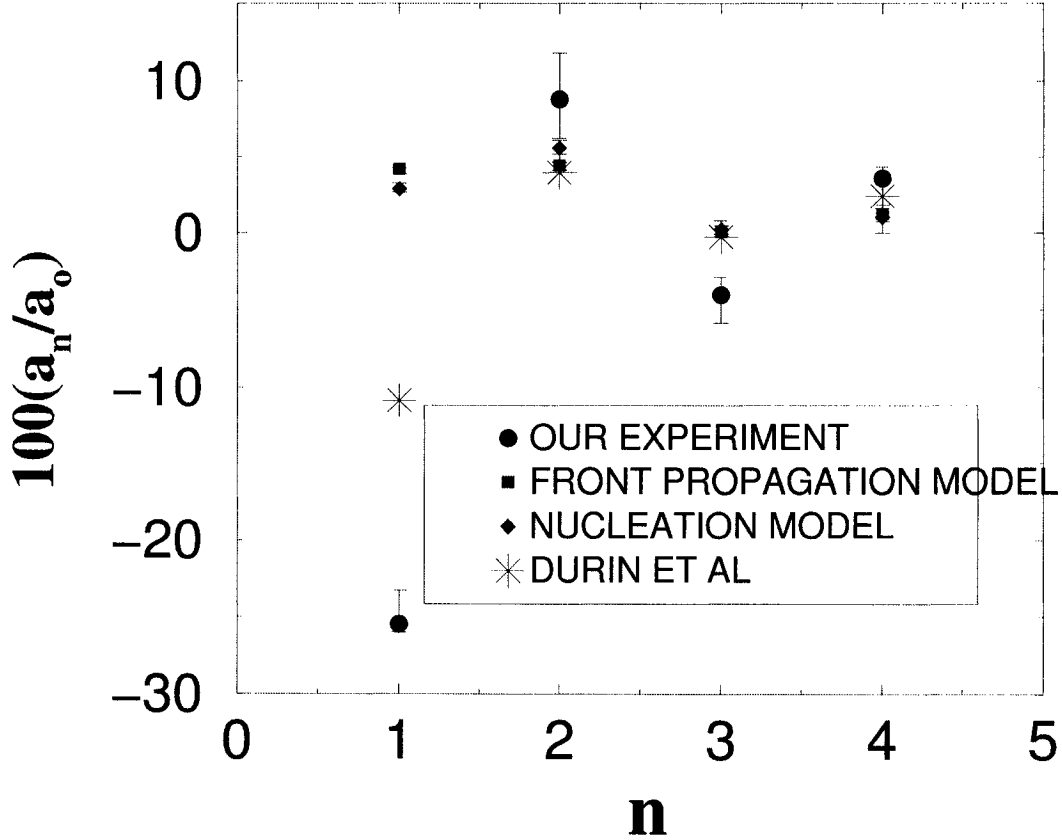
Figure 5.4: Fitting coefficients to the avalanche shapes determined for the two models, our experiment, and Durin et al's experiment [43]. We find that the coefficients are very similar for the two models. While the a_1 coefficients determined from the experiments are significantly different from the two models, the difference is not only in the sign of asymmetry but also in the magnitude of asymmetry. Each fitting coefficient, except for Durin et al's, was determined from three realizations of the universal scaling function in each case. The coefficients, for the two models and our experiment, plotted above, represent median values, while the error bars are determined from the higher and lower values. Durin et al's avalanche shape, presented in Fig. 5.5, was used to calculate the coefficients presented above; no error bars are provided in this case since only one realization was available.

46
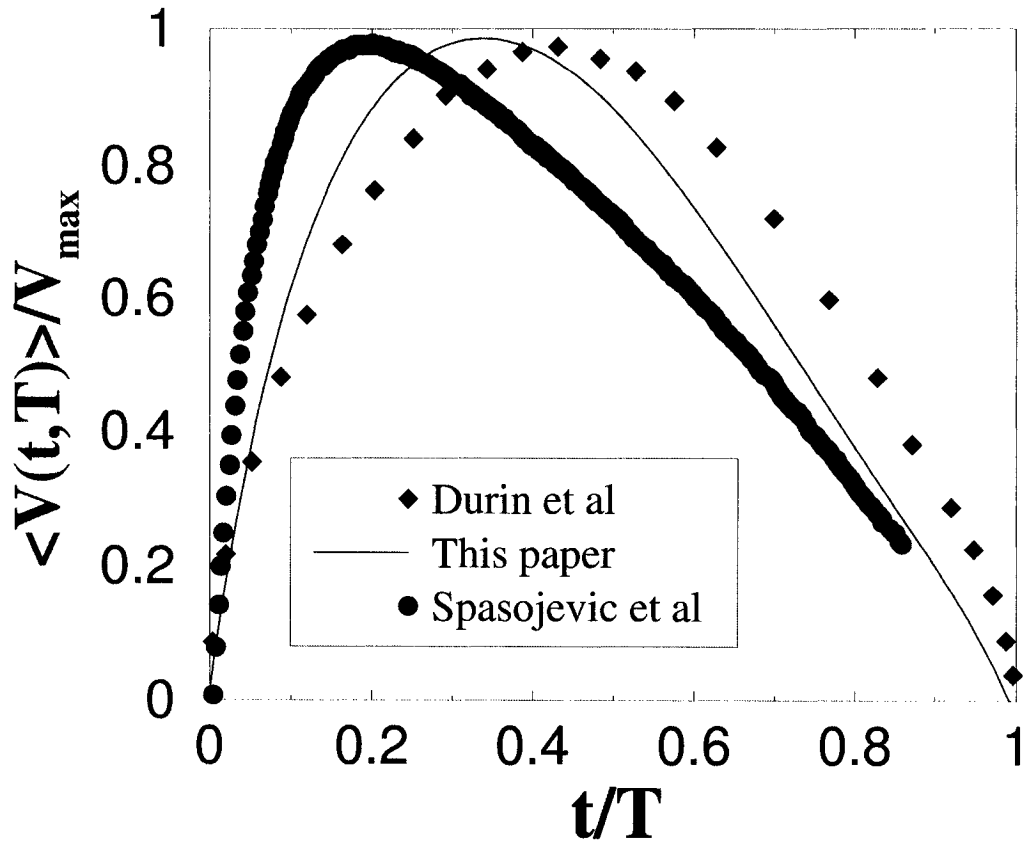
Figure 5.5: Comparison of our experimental pulse shapes with experimental pulse shapes obtained by two other groups. Durin et al's sample was under stress with large stress induced anisotropies, putting their experiment into the universality class of infinite range [14, 15, 16]. For Durin's experiment $1/\sigma\nu z = 1.77$ [43] and $\tau = 1.27$ [14, 15]. For Spasojević's experiment $1/\sigma\nu z = 1.58$ and $\tau = 1.77$ [42].

47

5.5 Discussion

In performing these analyses we have stumbled upon an interesting observation: after appropriate rescaling of the y-axis, the universal pulse shape function for the infinite range and nucleation model appear to look the same (see Inset for Fig. 5.1) even though we know [1] that the models do not belong to the same universality class. However, upon more precise quantitative analysis we see that they are in fact different, their a_1 coefficients are different by several σ. Furthermore, we tried to collapse two pulse shape functions with $T \simeq 52$ from the two different models and found that they could not be collapsed precisely despite, naturally, scaling by different critical exponents appropriate for the two models. The infinite range pulse scaling function is more asymmetric, as supported by the somewhat larger a_1 fit coefficient compared to the nucleation model result.

By examining the pulse shape scaling functions as a sharper test than merely critical exponents for the universality class of the non-equilibrium zero temperature RFIM, we raised many questions. What accounts for the difference between theory and experiment, and between different experiments? Is the theory incomplete or inaccurate at this level of description? Experimentally, we do not yet know what material features are required to produce universality of the pulse shape function. Differences between experimental results make further experimental tests desirable (see Fig. 5.5).

Although the three experiments we examined do not fall into the same universality class and do not have very similar pulse shapes, they share one universal aspect not shared by the results from simulation: all the experimental averaged pulse shapes are asymmetric in the leftward direction. This suggests that there may be a phenomena that exists in real materials that has not been accounted for in theory. Gianfranco Durin has recently suggested that the asymmetry may result from eddy currents [68].

48

Chapter 6

Universal Moment Rates Functions

To obtain an improved understanding of earthquake dynamics that can provide further evidence for or against an underlying critical point, we focus on faults with Gutenberg-Richter like earthquake statistics (i.e. near-critical behavior) and develop two universal scaling *functions* associated with mean moment-rate time profiles at either fixed total moment or fixed total earthquake duration. Universal scaling functions (or shape profiles) give important information on the underlying dynamics as discussed in chapter 1 and 2. If the behavior of fault zones with earthquakes following the Gutenberg-Richter statistics is indeed critical, then the shapes of these functions should be as universal as the exponent β in Eq. (1.1). The scaling functions can be used for a much stronger test of theory versus observed data via comparisons of entire functions as opposed to single-valued exponents. In this study we compute the scaling functions for both model predictions and observational data and compare the results. In section 6.1 we introduce the universal scaling functions and their scaling forms, and in section 6.2 extract the functions from both simulation and observational data. Finally, in section 6.3 we discuss the results and emerging new questions.

6.1 Moment Rate Shapes

In this section we focus on fault zones with Gutenberg-Richter power law statistics, modeled by systems at or close to the $\epsilon = 0$ critical point. Recent analysis allowed researchers to obtain the moment rate $dm_0(t)/dt$, which gives the slip on a fault per unit time during the propagation of earthquake rupture, for hundreds of large seismic events recorded on global networks [69]. Motivated by works on statistical physics of magnetic systems studied in the previous chapter (also refer to [1, 70]), we are interested in studying the event-averaged moment rate time profile (FIG. 6.2) for earthquakes with given duration T, denoted with $< dm_0(t|T)/dt >$, and the event-averaged moment rate time profile (FIG. 6.1) for earthquakes with given total moment M_0, denoted with $< dm_0(t|M_0)/dt >$. Here $m_0(t|T)$ is the (cumulative) moment at time t of the propagating earthquake of total duration T, and $m_0(t|M_0)$ is the cumulative moment at time t of the earthquake of total moment M_0. Theoretical analysis of phase diagrams similar to that shown in FIG. 4.2 implies that near the critical point there should be, in addition to scaling exponents, also universal scaling functions (up to a rescaling of the ordinate and abscissa) [70]. In our model the two scalable functions of interest, $< dm_0(t|M_0)/dt >$ and $< dm_0(t|T)/dt >$, obey respectively the following

scaling relations [13, 40]:

$$< dm_0(t|M_0)/dt > /M_0^{1/2} \sim f(t/M_0^{1/2}) \tag{6.1}$$

and

$$< dm_0(t|T)/dt > \sim g(t/T) \tag{6.2}$$

We determined these scaling functions from corresponding results for magnets, using the fact that our mean field version of the Ben-Zion and Rice model of Eq. (4.2) [60, 61] is in the same universality class (i.e. has the same universal behavior on long length scales) as the above mentioned model for domain wall motion in magnets. Details of the determination of the scaling form given Eq. (6.1) and the functional form of $f(...)$ are given in Appendix C.

6.2   Exponents and Data Collapses

We compare the observation results with our model and find remarkable agreement in most cases. The frequency-moment distribution, $D(M_0) \sim M_0^{-1-\beta}$ of the observed data [69] has (inset of FIG. 4.2) three decades of scaling and an exponent of $\beta = 1/2 \pm 0.05$, in close agreement with the model near $\epsilon = 0$. The deviation from a power law distribution at the low moment range is associated with the reduced resolution of the observational network for small events. In mean field theory the universal scaling function $f(x)$ in Eq. (6.1) is of the exact form [71]: $f_{mf}(x) = Axe^{-Bx^2/2}$ with non-universal constants $A = B = 1$. In FIG. 6.1 we present a collapse of the observational data of $< dm_0(t|M_0)/dt >$ for four different values of M_0 to obtain the corresponding function $f_{exp}(x)$ for observations with $x = t/M_0^{1/2}$. The observational curves not only collapse, and are therefore *universal*, the mean field exponent 1/2 in the scaling variable x is in excellent agreement with observations. We fit the functional form $f_{mf}(x)$ with $A = 4$ and $B = 4.9$ to the collapse of the observed data; $f_{exp}(x)$ deviates from the $f_{mf}(x)$ for small values of the ordinate.

In mean field theory, the function $g(x)$ of Eq. (6.2) is of the symmetric form: $g_{mf}(x) = Ax(1-x)$, where A is a non-universal constant. In FIG. 6.2 we collapse observational data for $< dm_0(t|T)/dt >$ for three values of T to obtain the function $g_{exp}(x)$ with $x = t/T$. Again we find that the curve

51
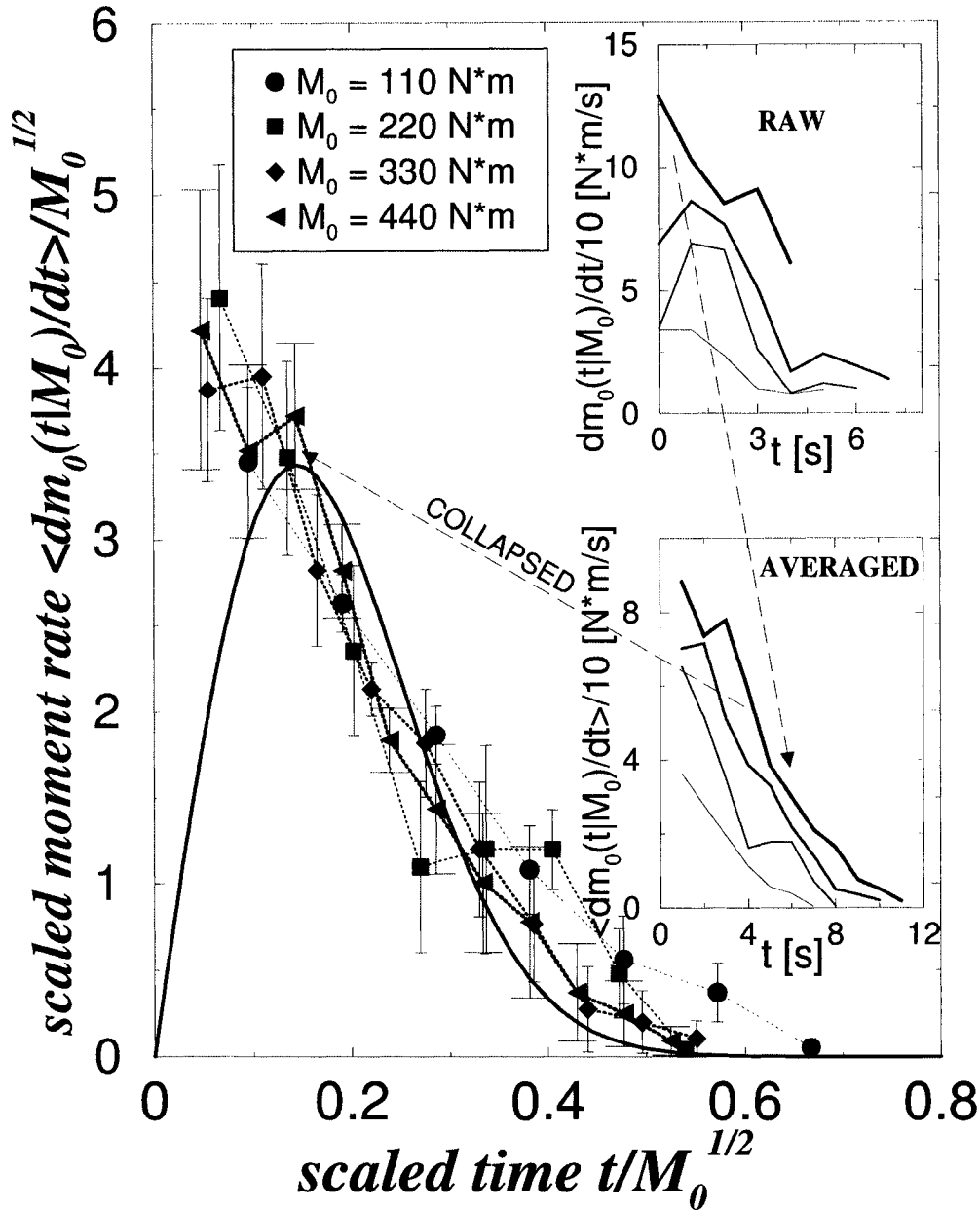
Figure 6.1: A collapse of averaged earthquake pulse shapes, $< dm_0(t|M_0)/dt >$, with the size of the moment M_0 in Newton meters within 10% of each size given in the legend respectively. In order to obtain each collapsed moment rate shape, five to ten earthquakes were averaged for each value of M_0. The collapse was obtained using the mean field scaling relation [60]: $< dm_0(t|M_0)/dt >$ $/M_0^{1/2} \sim f(t/M_0^{1/2})$ (see text Eq. (6.1)). In our mean field theory the universal scaling function is $f_{mf}(x) = Axe^{-Bx^2/2}$ where $x = t/M_0^{1/2}$. We plot this functional form (bold curve) with $A = 4$ and $B = 4.9$. Inset: The raw data and the averaged data (before collapsed).

52

collapses well, even though only small data sets where available, and the exponent of 1 obtained from the collapse is in excellent agreement with mean field theory.

We also plot the mean field scaling function $g_{mf}(x)$ with $A = 80$. The results show that while the scaling exponents agree, there are notable differences between the observational function $g_{exp}(x)$ and the mean field function $g_{mf}(x)$, especially for small values of the ordinate. We find that finite size effects do not play a role in $g_{mf}(x)$ (or in $f_{mf}(x)$ for that matter). Also, we find that that mean skewness coefficient for the $g_{exp}(x)$ curves is -0.878 and the mean standard error of skewness is 0.705: since twice the standard error is greater than the absolute value of the skewness, the asymmetry is not statistically significant. Therefore more observational work with a larger data set is required to verify the moment rate shape asymmetry and clarify its origin. An asymmetry may result from a rupture process that begins with a failure of a large asperity, or possibly from finite fault size effects if the rupture process slows down once the rupture has traversed the fault in one direction.

6.3 Remarks

The employed earthquake model [47, 59] was shown in the past to have a critical point at $\epsilon = 0$ and additional dynamic regimes for $\epsilon > 0$ [60, 61] compatible with observed frequency-size statistics of earthquakes on individual fault zones [28, 29]. We have generalized the theoretical analysis to include a strengthening regime $\epsilon < 0$ with aftershocks, and derived universal scaling functions around the critical point $\epsilon = 0$. The results provide new tools for data analysis that may be used to obtain an improved understanding of earthquake dynamics. The analysis indicates that at $\epsilon = 0$, the model is in the same universality class as a recent model for domain wall motion in magnets [1, 13, 43, 60]. In other words, the two systems are marked by the exact same universal scaling exponents and universal scaling functions. The model predictions for frequency-size statistics and moment-rates of earthquakes near $\epsilon = 0$ are overall in close agreement with observational data of relatively large earthquakes recorded on global networks [69]. However, the observed mean moment-rate of earthquakes with a given duration T, apparently increases with time more rapidly than it drops off, contrary to the corresponding symmetric model function. The potential asymmetry in the observed data may result from a rupture process that begins with a failure of a large asperity.

53
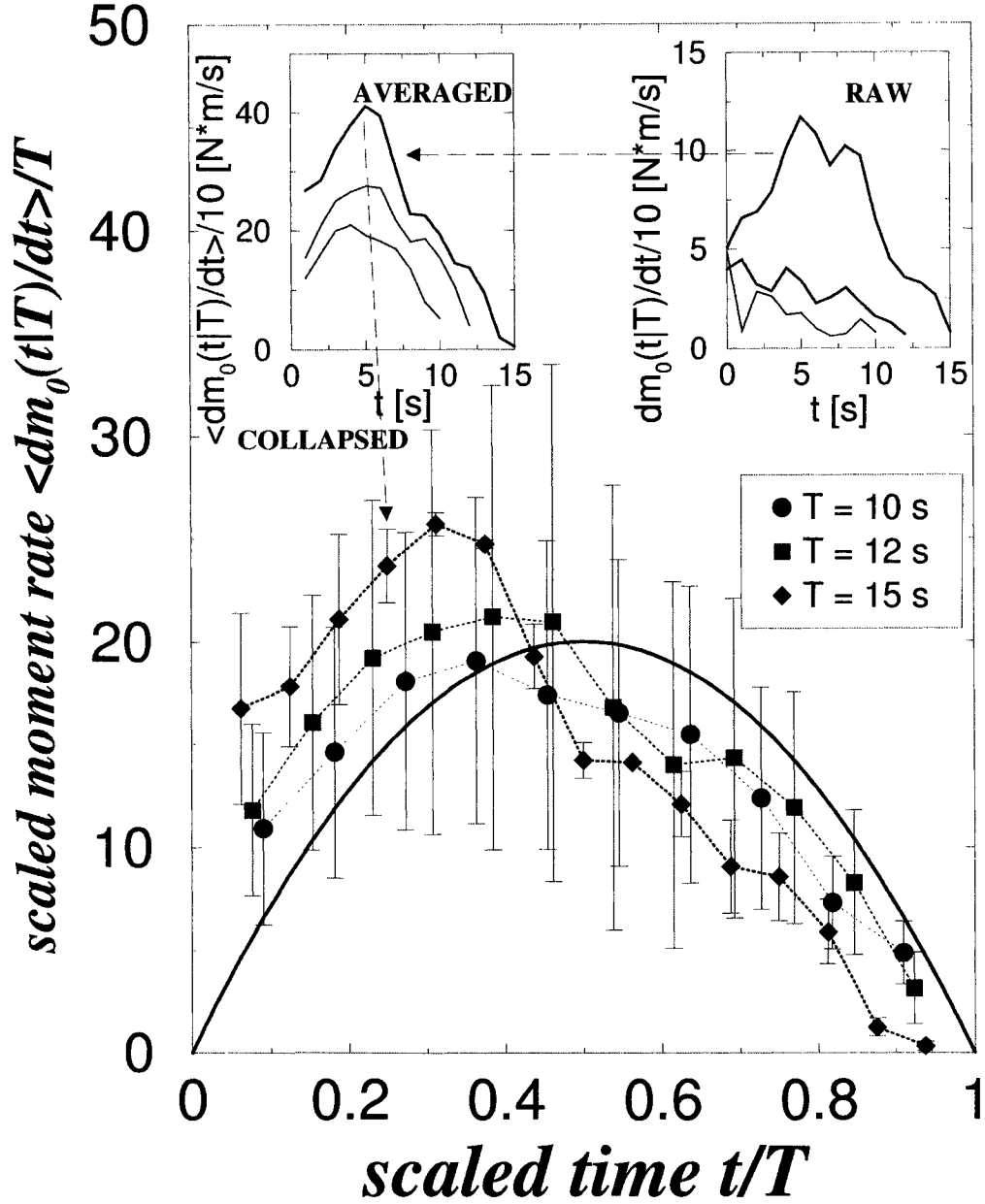
Figure 6.2: A collapse of averaged earthquake pulse shapes,$< dm_0(t|M_0)/dt >$ with a duration of T (seconds) within 10% (given in legend), is shown. The collapse was obtained using the mean field scaling relation [13]: $< dm_0(t|T)/dt > \sim g(t/T)$. In order to obtain each collapsed pulse shape, two to ten earthquakes were averaged for each value of T. In our mean field theory the universal scaling function is $g_{mf}(x) = Ax(1 - x)$ with $x = t/T$. We plot this functional form (bold curve) with $A = 80$. Note the apparent asymmetry to the left in the observed data while the theoretical curve is symmetric around is maximum. Inset: The raw data and the averaged data (before collapsed).

This is compatible with observations that hypocenter locations tend to be located close to the area on a fault that produce the largest moment release [e.g., [72]].

Theoretical analysis of such a potential asymmetric rupture process requires corrections to the simple earthquake model results. Recently it has been shown that the corresponding magnetic domain-wall model [1, 70] predicts well the critical scaling exponents for Barkhausen noise experiments in magnets. Significantly, the experimental scaling function for magnetization avalanches or Barkhausen "pulses" [1, 70], that is the analogue of the moment-rate time profile for fixed earthquake duration of Eq. (6.2), shows the same type of asymmetry that is apparently observed for earthquakes (FIG. 6.2). This raises the possibility that the origin of this asymmetry may be similar in both magnets and earthquakes. Our study shows that there are important theoretical and observational connections between processes in earthquake and magnetic systems.

A promising study of earthquake moment rate shapes was done by Heidi Houston [41] (see 2.1.2 for more details), where shallow earthquake events (less than 40km deep) and deep earthquake events (more than 40km deep) were separately analyzed. In Fig. 2.3 the top plots correspond to $\langle dm_0(t|M_0)/dt \rangle$ collapsed, and the bottom plots correspond to $\langle dm_0(t|T)/dt \rangle$ collapsed; we see that moment rate shapes for the Non-Plate Boundary or deep events agree very well with our predicted mean field shapes. By comparing the top plot (the Non-Plate Boundary curve) of Fig. 2.3 with the mean field prediction in Fig. 6.1 we see strong agreement in the moment rate shape. Likewise by comparing the bottom plot (the Non-Plate Boundary curve) of Fig. 2.3 with the mean field prediction in Fig. 6.2 we see excellent agreement in the shape. On the other hand, we do not see good agreement when comparing the Plate Boundary curves (shallow events) to our mean field predictions. Why deep events apparently agree with our mean field model better than shallow events is still an ongoing area of research. Note however, regarding the collapse of $\langle dm_0(t|M_0)/dt \rangle$, exponents of 1/3 and 2/3 were used by Houston [41] to rescale the x and y axises (by dividing by $M_0^{1/3}$ and $M_0^{2/3}$, respectively), instead of an exponent of 1/2 used in our analysis (see Fig. 6.1). It would be interesting to see if Houston's data would collapse with an exponent of 1/2 (both x and y axises), instead of exponents of 1/3 (x-axis) and 2/3 (y-axis). We hope this work will motivate more observational work and analysis to answer these questions.

55

Chapter 7

Higher Order Spectra in Avalanche Models

In previous chapters we have focused on specific models of earthquakes and magnets, however in this chapter our mean field analysis is relevant to a broad range of systems that include: charge density waves, vortices in type II superconductors, crack propagation, earthquakes, and Barkhausen noise in magnets. These systems are characterized by many interacting degrees of freedom and strong interactions that make thermal effects negligible, and the avalanche dynamics of these systems are described by Poisson statistics (given by Eq. (7.1)) in mean field theory at a critical point or critical depinning transition [13, 40].

Through our analysis of mean field avalanche models we determine the following spectral functions: Haar power spectrum, real 1.5 spectra, second spectra, and real cross second spectra for systems that have avalanche dynamics given by Eq. (7.1). This analysis provides new tools for noise analysis in dynamical systems, since there are very few theoretical calculations of higher order noise statistics. In particular, to our knowledge this is the first derivation of universal scaling forms of higher order spectra for the avalanche systems mentioned above.

The Haar transform allows us to obtain a power versus time series, $H(t, f_1)$, needed to calculate higher order spectra. These higher order spectra give valuable information about the avalanche dynamics in Barkhausen noise not accessible through ordinary power spectra [48, 49]. As discussed in chapter 2, higher order spectra also have been used to obtain crucial information about a variety of diverse systems such as: metastable states in vortex flow [35], natural auditory signals [36], conductance-noise in amorphous semiconductors [37], fluctuating current paths in devices [38], and quasi-equilibrium dynamics of spin glasses [39]. While much experimental work has been done studying higher order spectra [35, 36, 37, 38, 39, 48, 49], we present a rigorous mean field treatment that is applicable to a broad range of systems [40]. This analysis will allow a better understanding of the dynamics of these systems, and provide a direct method of comparison to experiment or observation.

In addition, we compare our general results from mean field theory to Barkhausen noise obtained: from a mean field simulation of the $T = 0$ random field Ising model (RFIM) [11], from a simulation of the $T = 0$ infinite range RFIM (IRM) in $d = 3$, and from experiment. We also find novel exponents from our analysis, and we compare our results from theory, simulation, and experiment; we find key similarities and differences.

57

7.1 Theory

7.1.1 Poisson Distribution

The probability distribution for the avalanche dynamics in the class of mean field avalanche models we are interested in is given by [13, 40]:

$$P(n_0 = 1, n_1, n_2, ..., n_\infty) = \frac{1}{en_1!} \prod_{t=2}^{\infty} \frac{e^{-n_{t-1}} n_{t-1}^{n_t}}{n_t!} \tag{7.1}$$

The above probability distribution (Eq. 7.1) is for the time series of a single avalanche at the critical point. In the context of the mean field RFIM, n_t represents the number of spins flipped at a time t. That is, each n_t represents a shell of the avalanche, and since an avalanche begins with one spin flip we have that $n_0 = 1$.

Let $\langle . \rangle$ represent the average over Eq. 7.1. In order to calculate the Haar transform and higher order spectra in mean field theory we need the following quantities, where $m \geq l \geq k \geq 0$ and $j \geq 0$:

$$\langle n_j \rangle = 1 \tag{7.2}$$

$$\langle n_j^2 \rangle = j + 1 \tag{7.3}$$

$$\langle n_j n_{j+k} \rangle = \langle n_j^2 \rangle = j + 1 \tag{7.4}$$

$$\langle n_j^3 \rangle = \frac{1}{2}(3j^3 + 5j + 2) \tag{7.5}$$

$$\langle n_j^4 \rangle = \frac{1}{2}(6j^3 + 13j^2 + 9j + 2) \tag{7.6}$$

$$\langle n_j n_{j+k} n_{j+l} \rangle = \langle n_j^3 \rangle + k \langle n_j^2 \rangle \tag{7.7}$$

$$\langle n_j n_{j+k} n_{j+l} n_{j+m} \rangle$$
$$= \langle n_j^4 \rangle + (2k + l) \langle n_j^3 \rangle + \frac{k}{2}(k + 2l - 1) \langle n_j^2 \rangle \tag{7.8}$$

These relations can be determined from Eq. (7.1). We notice that the time ordering of the indices plays on important role. Details of how Eqs. (7.2-7.8) were derived are given in Appendix E.

58

7.1.2 Haar Power

The Haar transform is a simple wavelet transform with basis states consisting of single-cycle square waves. We use the Haar transform rather than the Fourier transform since it gives us improved time resolution in exchange for less frequency resolution. Time resolution is important to our purpose since we are interested in studying how the power contribution around a frequency f_1 changes along the duration of the avalanche.

Physically, the Haar power, $H(t, f_1)$, is the absolute square of the time integral over a period (of duration $1/f_1$) of a single-cycle square wave times a section of the train centered around t [49]. In other words, to determine the Haar power we integrate a square wave of duration $1/f_1$ over a section of the noise train centered at time t; this integrated segment is then squared to assure our resulting values is positive definite, this squared segment corresponds to $H(t, f_1)$, the Haar power at time t and around frequency f_1. In order to analytically determine the Haar power series we first define the sum over N shells:

$$\tilde{x}_i^+(N) = \sum_{l=0}^{N/2-1} n_{Ni+l}\Delta t \tag{7.9}$$

$$\tilde{x}_i^-(N) = \sum_{l=N/2}^{N-1} n_{Ni+l}\Delta t \tag{7.10}$$

Where $t = Ni$, and Δt is the time separation between shells. The Haar power series for a frequency $f_1 = \frac{1}{N\Delta t}$ is defined as:

$$H(i = \frac{t}{N}, f_1 = \frac{1}{N\Delta t}) \equiv \langle(\tilde{x}_i^+(N) - \tilde{x}_i^-(N))^2\rangle \tag{7.11}$$

To evaluate Eq. 7.11 we determine the following relations:

$$\langle\tilde{x}_i^\pm(N)\rangle = N\Delta t/2 \tag{7.12}$$

$$\langle(\tilde{x}_i^+(N))^2\rangle = \sum_{m=0}^{N/2-1} [2(N/2 - 1 - m) + 1]\langle n_{Ni+m}^2\rangle \tag{7.13}$$

59

$$\langle (\tilde{x}_i^-(N))^2 \rangle = \sum_{m=N/2}^{N-1} [2(N - 1 - m) + 1] \langle n_{Ni+m}^2 \rangle \tag{7.14}$$

$$\langle \tilde{x}_i^+(N)\tilde{x}_i^-(N) \rangle = \frac{N}{2} \sum_{m=0}^{N/2-1} \langle n_{Ni+m}^2 \rangle \tag{7.15}$$

When evaluating Eq. (7.13-7.15) we must take into account the time ordering of the indices, since the time ordering is needed to evaluate the ensemble average of 2-pt (Eq. 7.4), 3-pt (Eq. 7.7), and 4-pt (Eq. 7.8) correlation functions. Refer to Appendix F for details.

The above sums can be evaluated with the help of Eq. (7.3). Now using Eqs. (7.12)-(7.15) we obtain the following exact result:

$$H(i, f_1 = \frac{1}{N\Delta t}) = \frac{1}{12}(\frac{1}{f_1^3} + \frac{2(\Delta t)^2}{f_1}) \tag{7.16}$$

To find the Haar power spectrum we sum over all i, that corresponds to the sum over the Haar wavelets. Since $H(i, f_1)$ does not depend on the avalanche duration, we must set a duration for the avalanche in order to perform the sum over Haar wavelet. Therefore we define the duration of the avalanche to be T. Now since blocks of N shells have been summed over, we perform a sum over Eq. (7.16) from 0 up to $T/N - 1$ (where T/N represents the number of wavelets):

$$S_H(f_1) = \frac{1}{T} \sum_{i=0}^{T/N-1} H(f_1 = \frac{1}{N}, i) \tag{7.17}$$

$$= \frac{1}{12}(2(\Delta t)^2 + \frac{1}{f_1^2}) \tag{7.18}$$

$$\simeq \frac{1}{12f_1^2} \tag{7.19}$$

The Haar power spectrum, $S_H(f_1)$, is in excellent agreement with the Haar power spectrum determined from simulation. The Fourier power spectrum, $S_F(f_1) = 1/f_1^2$ [13], differs by an additive constant and a constant factor from $S_H(f_1)$. The additive constant, which depends on Δt, is in effect a result of aliasing produced by the discrete sampling.

60

7.1.3   1.5 Spectra, Second Spectra, and Cross Second Spectra

The 1.5 spectra, second spectra, and cross second spectra are defined below:

$$S_{1.5}(f_2, f_1) = \frac{\langle F_t\{v(t, f_1)\}F_t^*\{H(t, f_1)\}\rangle}{\langle H(t, f_1)\rangle_t} \tag{7.20}$$

$$S_2(f_2, f_1) = \frac{\langle F_t\{H(t, f_1)\}F_t^*\{H(t, f_1)\}\rangle}{\langle H(t, f_1)\rangle_t^2} \tag{7.21}$$

$$S_2(f_2, f_b, f_a) = \frac{\langle F_{t_a}\{H(t_a, f_a)\}F_{t_b}^*\{H(t_b, f_b)\}\rangle}{\langle H(t_a, f_a)\rangle_{t_a}\langle H(t_b, f_b)\rangle_{t_b}} \tag{7.22}$$

Where $v(t, f_1)$ is the sum of n_i around the time t over a duration $1/f_1$, and f_2 is the frequency conjugate to t. Also, $F_t\{...\}$ is the discrete Fourier transform with respect to t. Now $\langle ...\rangle_t$ denotes sum over t over the duration of the avalanche $(\sum_{t=0}^{T-1/f_1})$, similarly $\langle ...\rangle_{t_a} \equiv \sum_{t=0}^{T-1/f_a}$ and $\langle ...\rangle_{t_b} \equiv \sum_{t=0}^{T-1/f_b}$. For the cross second spectra, $S_2(f_2, f_b, f_a)$, we require that $f_b > f_a$. In addition, in the definition of $S_2(f_2, f_b, f_a)$ we require two times, t_a and t_b. The time t_a labels the starting point of a single-cycle square wave with a period of $1/f_a$ along the Barkhausen train, and therefore t_a takes on values that are multiples of $1/f_a$. Similarly, t_b labels the starting point of a single-cycle square wave with a period of $1/f_b$, and takes on values that are multiples of $1/f_b$.

To calculate Eq. (7.20-7.22) we first write the product of Fourier transforms as the Fourier transform of a convolution. This mathematical identity allows us to separate the Fourier transform ($F_t\{...\}$) from the ensemble average ($\langle.\rangle$) This leaves us with the following quantities: $\langle v(t, f_1)H(t + \theta, f_1)\rangle$, $\langle H(t, f_1)H(t+\theta, f_1)\rangle$, and $\langle H(t_a+\theta, f_a)H(t_b, f_b)\rangle$ where θ is the convolution variable. These quantities may then be rewritten as a sum of 3-pt or 4-pt correlation functions, and subsequently evaluated.

We present the results of our mean field calculation in Eq. (7.23-7.28) (given below) in terms of general scaling forms since the mean field and IRM simulations, as well as the experimental data, obey the same scaling form as mean field theory, only with different exponents and non-universal constants.

61

$$\Gamma_{1.5}(f_1) \equiv \sum_{t=0}^{T-1/f_1} \langle v(t,f_1)H(t,f_1)\rangle \simeq \frac{A_{1.5}}{f_1^{Q_{1.5}}} \qquad (7.23)$$

$$\Gamma_2(f_1) \equiv \sum_{t=0}^{T-1/f_1} \langle H(t,f_1)H(t,f_1)\rangle \simeq \frac{A_2}{f_1^{Q_2}} \qquad (7.24)$$

$$\Gamma_2(f_b,r) \equiv r \sum_{t_a=0}^{T-1/f_a} \sum_{t_b=t_a}^{t_a+1/f_a-1/f_b} \langle H(t_b,f_b)H(t_a,f_a)\rangle \simeq \frac{D_2 r^3}{f_b^{Q_2}} \qquad (7.25)$$

$$Re\{S_{1.5}(f_2,f_1)\} = \frac{B_{1.5}}{f_2^{V_{1.5}}} + \Gamma_{1.5}^{(N)}(f_1) \qquad (7.26)$$

$$S_2(f_2,f_1) = \frac{B_2}{f_2^{V_2}} + \Gamma_2^{(N)}(f_1) \qquad (7.27)$$

$$Re\{S_2(f_2,f_a,f_b)\} = \frac{B_2 r}{f_2^{V_C}} + \Gamma_2^{(N)}(f_b,r) \qquad (7.28)$$

The exponents $V_{1.5}$, V_2, $Q_{1.5}$, Q_2 are given in Table 7.1 for mean field theory, the IRM, and the experiment. Also, $A_{1.5}$, A_2, $B_{1.5}$, and B_2 are non-universal constants. In Eq. (7.25) and Eq. (7.28) $r = f_a/f_b$. Plots of Eqs. (7.26-7.28) are given in Figs. (7.1)-(7.3).

The functions $\Gamma_{1.5}(f_1)$, $\Gamma_2(f_1)$, and $\Gamma_2(f_b,r)$ are independent of f_2 since they resulted from the $\theta = 0$ evaluation of $\langle v(t,f_1)H(t+\theta,f_1)\rangle$, $\langle H(t,f_1)H(t+\theta,f_1)\rangle$, and $\langle H(t_a+\theta,f_a)H(t_b,f_b)\rangle$ (see Fig. 7.4). These f_2 independent terms are referred to as Gaussian background terms [38]. Now $\Gamma_{1.5}^{(N)}(f_1)$, $\Gamma_2^{(N)}(f_1)$, and $\Gamma_2^{(N)}(f_b,r)$ are $\Gamma_{1.5}(f_1)$, $\Gamma_2(f_1)$, and $\Gamma_2(f_b,r)$ normalized by $\langle H(t,f_1)\rangle_t$, $\langle H(t,f_1)\rangle_t^2$, and $\langle H(t_b,f_b)\rangle_{t_b}\langle H(t_a,f_a)\rangle_{t_a}$, respectively. The first terms of Eq. (7.26) and Eq. (7.27) have no f_1 dependence, since the f_1 dependence of these terms drops out after they are normalized by $\langle H(t,f_1)\rangle_t$ and $\langle H(t,f_1)\rangle_t^2$, respectively. Nevertheless, the lack of f_1 dependence in the first terms of second spectra and real 1.5 spectra is in excellent agreement with our simulation results, see Fig. 7.1 and the inset of Fig. 7.2. Also, we defer the discussion of $Im\{S_2(f_2,f_a,f_b)\}$ and $Im\{S_{1.5}(f_2,f_1)\}$, since they are very sensitive to the non-stationary properties of the avalanche in the analytical model. Please refer to Appendix G for details of how Eqs. (7.23-7.28) are calculated.

62
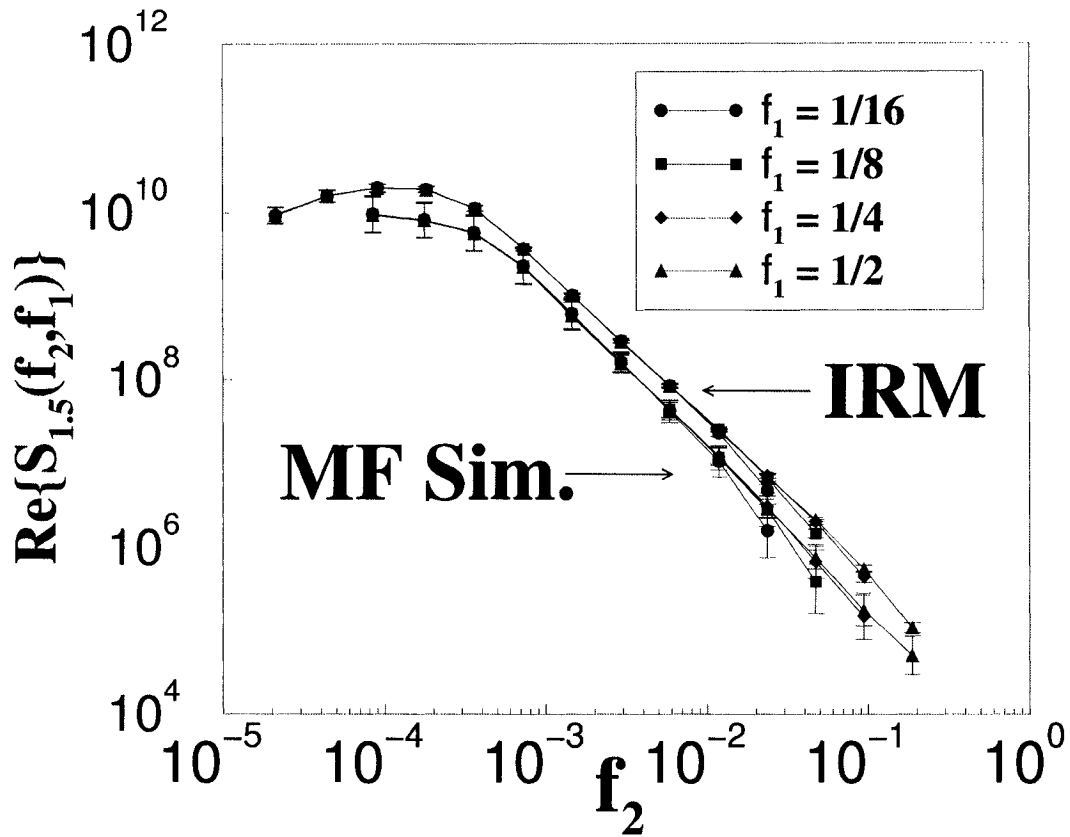
Figure 7.1: We present the $Re\{S_{1.5}(f_2, f_1)\}$ in the MF simulation and in the IRM. At high frequency $Re\{S_{1.5}(f_2, f_1)\} \sim f_2^{-V_{1.5}}$ (go to Table 7.1). There is not a visible flattening present due to $\Gamma_{1.5}^{(N)}(f_1)$ ($\theta = 0$) term, since the magnitude of this term is small relative to the f_2 dependent term.

63
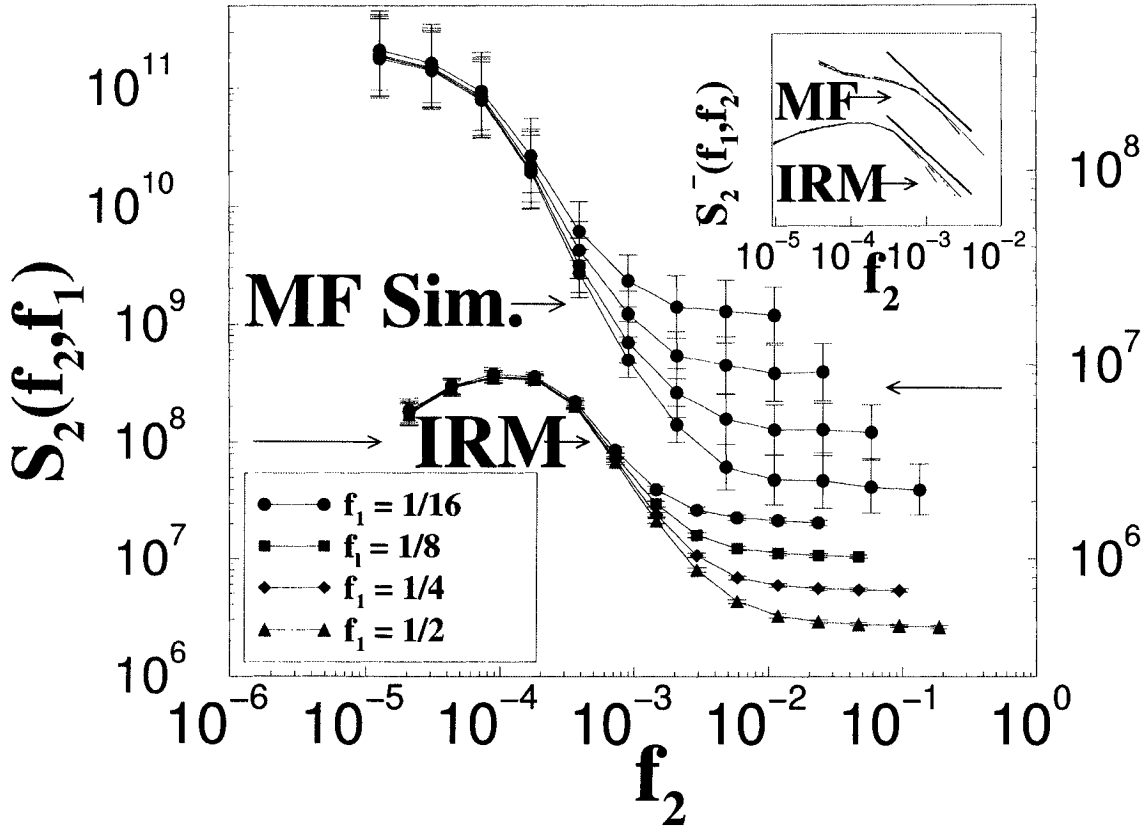
Figure 7.2: We present the $S_2(f_2, f_1)$ in the MF and IRM. Notice the flattening due to the $\Gamma_2^{(N)}(f_1)$ ($\theta = 0$) term. Inset: $S_2^-(f_2, f_1)$ is the second spectra in the MF simulation and the IRM with background term subtracted. The bold lines adjacent to the MF curve is a power law with an exponent of -2, and the bold line adjacent to the IRM curve has an exponent of -1.8.

64
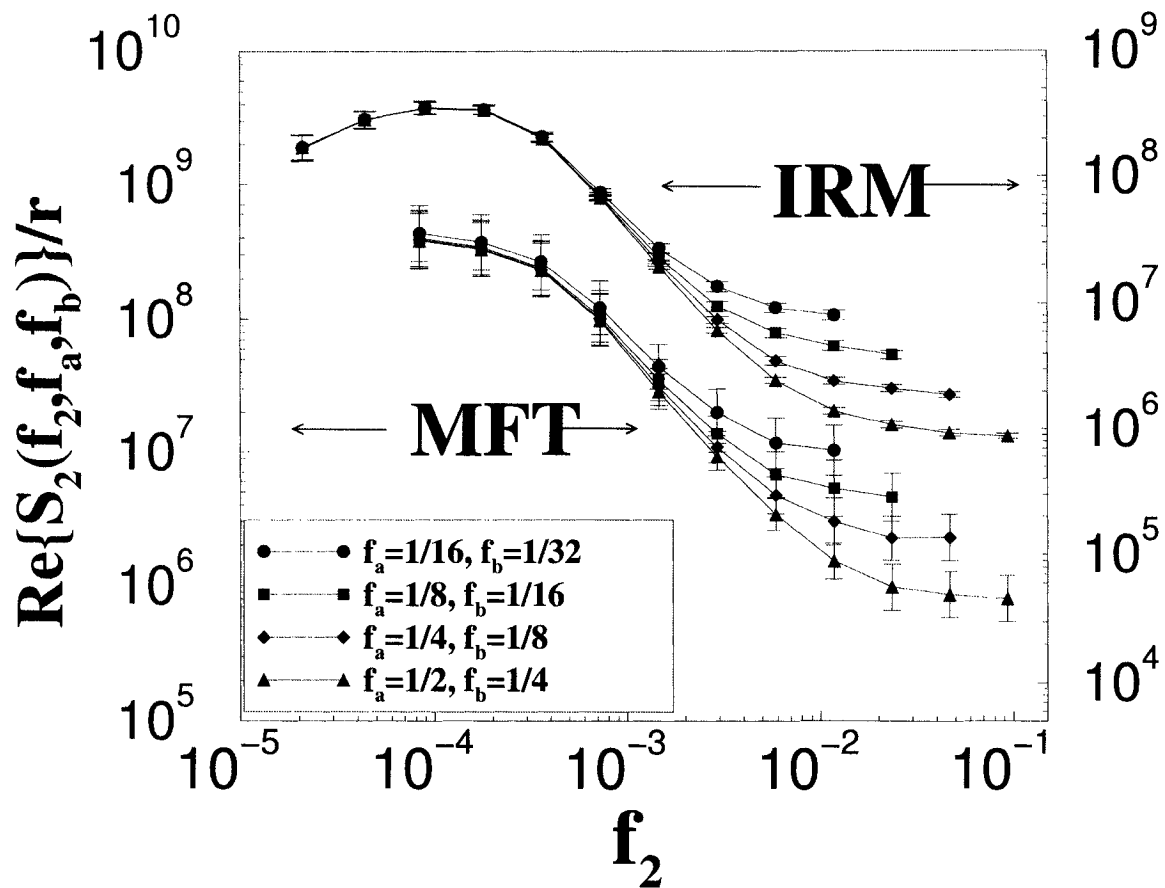
Figure 7.3: We present the $Re\{S_2(f_2, f_a, f_b)\}$ for $r = f_a/f_b = \frac{1}{2}$ in the MF simulation and the IRM. Notice the flattening due to the $\Gamma_2^{(N)}(f_b, r = \frac{1}{2})$ $(\theta = 0)$ term.

65

Figure 7.4: We present $\Gamma_2(f_1, r)$ ($r = \frac{f_a}{f_b} = 1$ corresponds to $\Gamma_2(f_1)$, and we set $f_1 = f_b$ for $r < 1$) in the MF simulation and in the IRM. $\Gamma_2(f_1, r)$ collapses for $r < 1$, in excellent agreement with Eq. (7.25). For high frequency $\Gamma_2(f_1, r) \sim f_1^{-Q_2}$, (see Table 7.1). Inset: $\Gamma_{1.5}(f_1)$ for the MF and the IRM. For high frequency $\Gamma_{1.5}(f_1) \sim f_1^{-Q_{1.5}}$, see Table 7.1.

66

7.2 Simulation

7.2.1 Mean Field (MF) Simulation

We perform 300 runs of a simulation of the mean field RFIM. We collect data taken from $H \in [0, 0.00125]$ at $R = 0.79788$ ($R_c = 0.79788456$) in systems with $N = 15 \times 10^6$ spins, and $J = 1$. From this data we determine our simulation results agree with the scaling forms given in Eq. (7.23-7.28) with exponents given by Table 7.1.

7.2.2 Infinite Range Model (IRM) Simulation

We perform 60 runs of a 3D simulation of the IRM. The data was taken from $H \in [1.25, 1.88]$ (from the slanted part of the hysteresis loop) at $R = 2.2$ in system with $N = 400^3$ spins, $J_{inf} = \frac{1}{N}$ and $J = 1$. Again results agree with Eq. (7.23-7.28) with exponents given in Table 7.1.

7.2.3 Finite Size Effects

We study finite size effects in our simulation (mean field and IRM) by examining higher order spectra for various system sizes. We find that for smaller system sizes the high frequency scaling (and flattening due to the background term) is unchanged for second spectra, real 1.5 spectra, and real cross second spectra. However, at low frequency the scaling regime of the second spectra, real 1.5 spectra, and real cross second spectra rolls over (in the IRM and MF simulations) at frequency $f_1 \simeq \frac{1}{T_{max}}$, where T_{max} is the maximum avalanche duration. T_{max} is system size dependent where $T_{max} \sim L^z$, and $L = N^{1/d}$. In a $N = 400^3$ system (IRM) we find that $T_{max} \simeq 4300$.

7.3 Experiment

We compare our results for theory and simulation with results obtained from an experiment performed on an (unstressed) amorphous alloy, $Fe_{21}Co_{64}B_{15}$. Measurements were performed on a 21 cm x 1 cm x 30 μm ribbon of $Fe_{21}Co_{64}B_{15}$ alloy, a soft amorphous ferromagnet obtained from Gianfranco Durin. The domain walls run parallel to the long axis of the material, with about 50 domains across the width. A solenoid, driven with a triangle wave, applies a magnetic field along the long axis of the sample. Since domain wall motion dominates over other means of magnetization

67

	$V_{1.5}$	V_2	$Q_{1.5}$	Q_2	V_C
MFT	2	2	3	5	2
MF Sim.	1.93 ± 0.10	1.92 ± 0.12	2.95 ± 0.10	4.93 ± 0.12	1.92 ± 0.15
IRM ($d=3$)	1.80 ± 0.07	1.80 ± 0.05	2.73 ± 0.06	4.46 ± 0.07	1.82 ± 0.14
Experiment	0.93 ± 0.20	0.66 ± 0.12	2.81 ± 0.08(h.f.) 1.66 ± 0.12(l.f)	4.39 ± 0.15(h.f.) 2.48 ± 0.10(l.f.)	0.63 ± 0.06

Table 7.1: We present the values of the exponents: $V_{1.5}$, V_2, $Q_{1.5}$, and Q_2 given in Eqs. (7.23-7.27) for mean field theory (MFT), mean field simulation (MF Sim.), the infinite range model (IRM) for $d = 3$, and experiment. While the exponents values for MFT were determined analytically, the exponents for the MF Sim., IRM, and experiment were determined through a non-linear curve fitting of the data. In particular, in our experimental plots (Figs. 7.5-7.8) we use the following window sizes to fit the exponents: $f_1 : [1kHz, 200kHz]$ for $V_{1.5}$, $f_1 : [20Hz, 2kHz]$ for V_2, $f_1 : [14kHz, 40kHz]$ for $Q_{1.5}$ (high frequency exponent), $f_1 : [.4kHz, 18kHz]$ for Q_2 (high frequency exponent), and $f_1 : [20Hz, 2kHz]$ for V_C. We find that that these exponents do not change (outside of their error bars stated above) when the window size for their measurement is changed within the scaling regime of the data. Also, l.f. stands for low frequency and h.f. stands for high frequency, since for the experiment there are distinct l.f. and h.f. exponents, in some cases.

in the linear region of the loop, data were collected in only a selected range of applied fields near the center of the loop. The Barkhausen noise was measured by a small pick-up coil wound around the center of the sample. This voltage signal was amplified, anti-alias filtered and digitized, with care taken to avoid pick-up from ambient fields. Barkhausen noise was collected for both increasing and decreasing fields for 80 cycles of the applied field through a saturation hysteresis loop. The driving frequency was 0.01 Hz; this corresponds to $c = 0.09$, where c is a dimensionless parameter proportional to the applied field rate and is defined in the Alessandro Beatrice Bertotti Montorsi model (ABBM model) for the Barkhausen effect in metals [17]. In this way, our measurements should be well inside the $c < 1$ regime identified in the ABBM model, in which we can expect to find more or less separable avalanches rather than continuous domain wall motion [17].

7.4 Discussion

The mean field theoretical calculation was for a single infinite avalanche while the mean field simulation was obtained from a train of avalanches. Consequently, the train of avalanches introduces intermittancy that lowers the magnitude of the mean field exponents, since the intermittancy effectively adds white inter-avalanche noise to the intra-avalanche noise seen in the MF calculation. From Table 7.1 we notice that the exponents for our mean field simulation are systematically smaller
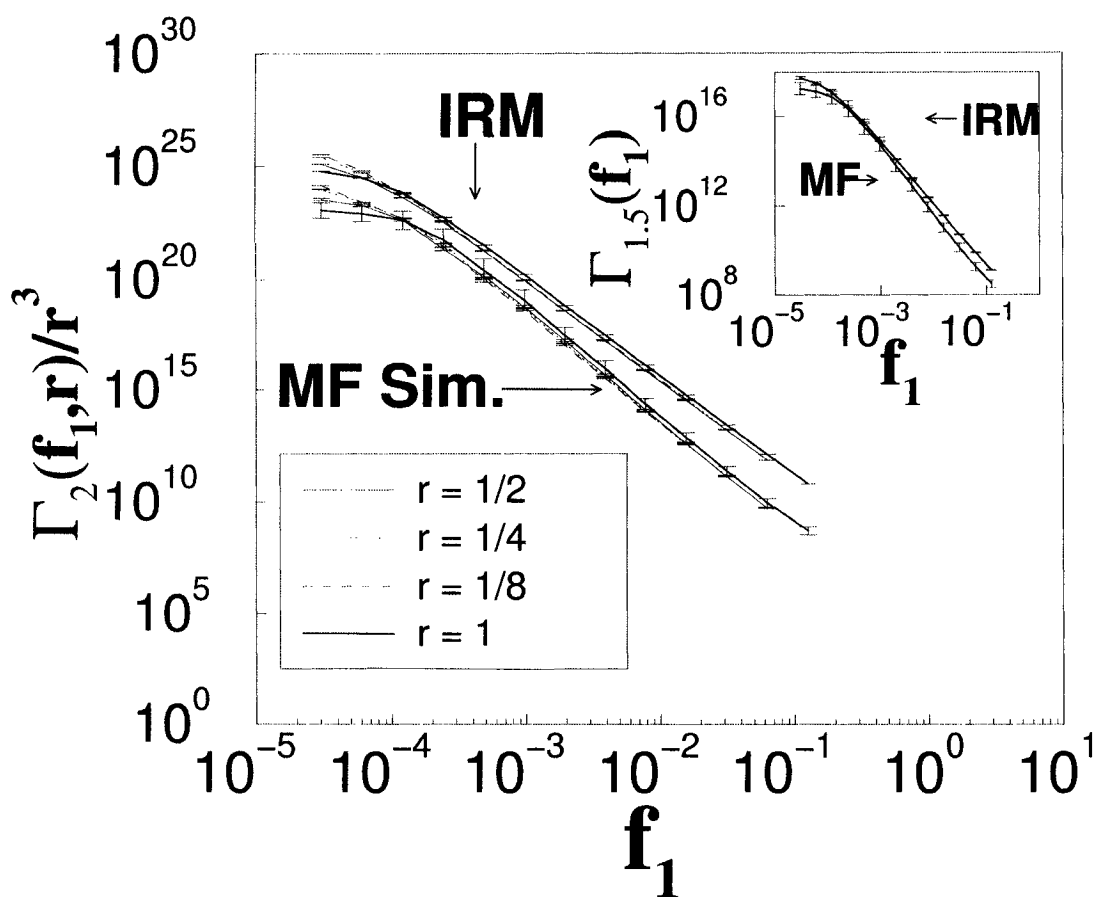
68
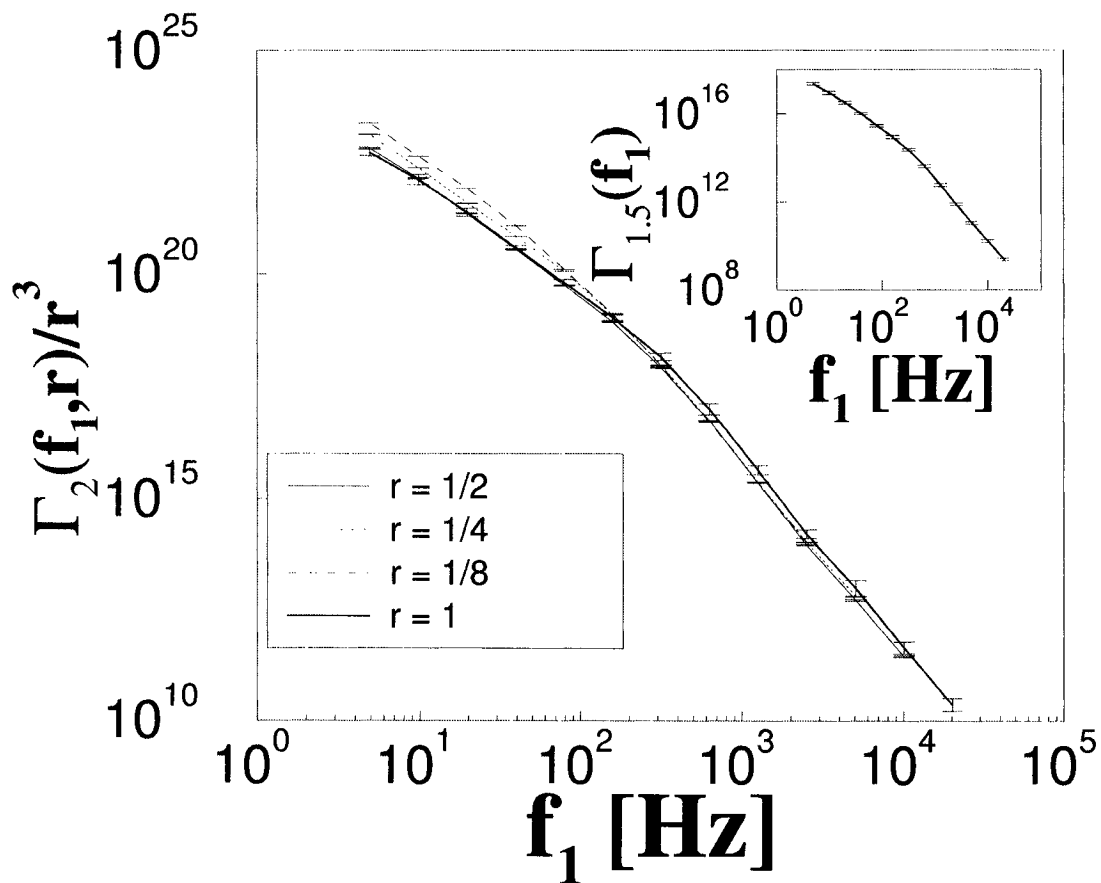
Figure 7.5: We present $\Gamma_2(f_1, r)$ (where $r = \frac{f_a}{f_b} = 1$ corresponds to $\Gamma_2(f_1)$, and we set $f_1 = f_b$ for $r < 1$) in experiment. $\Gamma_2(f_1, r)$ collapses for $r < 1$, in excellent agreement with Eq. (7.25). For high frequency $\Gamma_2(f_1, r) \sim f_1^{-Q_2}$, see Table 7.1. Inset: $\Gamma_{1.5}(f_1)$ for experiment. For high frequency $\Gamma_{1.5}(f_1) \sim f_1^{-Q_{1.5}}$, see Table 7.1.

69
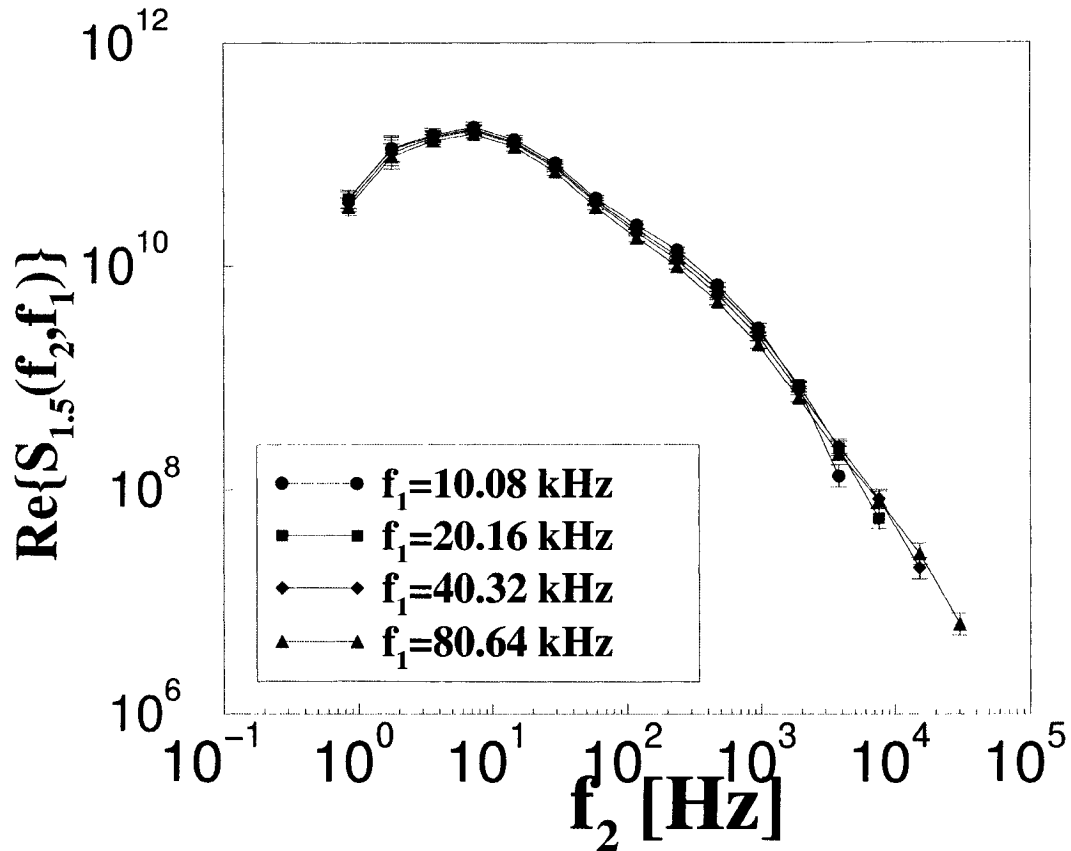
Figure 7.6: We present the real 1.5 spectra $Re\{S_{1.5}(f_2, f_1)\}$ in experiment. At high frequency $Re\{S_{1.5}(f_2, f_1)\} \sim f_2^{-V_{1.5}}$ (go to Table 7.1). The high frequency scaling regime is small for the experimental real 1.5 spectra since curve rolls over at $f_{cross} \simeq 320$ Hz.

70
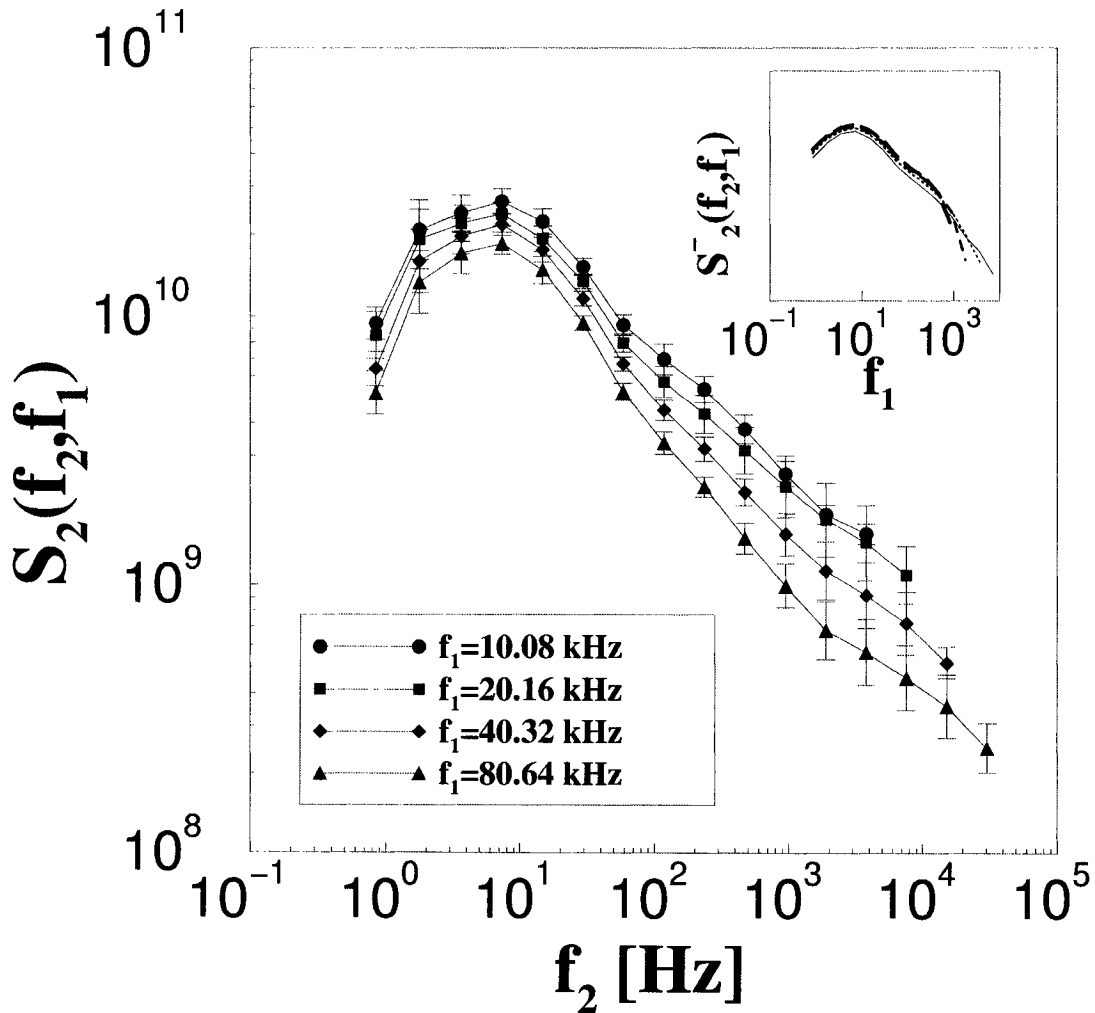
Figure 7.7: We present the second spectra, $S_2(f_2, f_1)$, in experiment. At high frequency the scaling is given $S_2(f_2, f_1) \sim f_2^{-V_2}$, where $V_2 = 0.66 \pm 0.12$, that is significantly smaller than the mean field simulation ($V_2 = 1.92 \pm 0.12$) and the IRM ($V_2 = 1.80 \pm 0.05$). Further more, there is no conspicuous flattening in these experimental second spectra curves, indicating that the background term, $\Gamma_2^{(N)}(f_1)$, is small for experiment versus the mean field simulation and the IRM. Also, there is a noticeable separation between curves at low frequency that is not present in the mean field simulation or IRM second spectra curves. Inset: $S_2^-(f_2, f_1)$ is the second spectra in experiment with the background term subtracted, as a result the separation between the curves vanishes, within error bars.

71
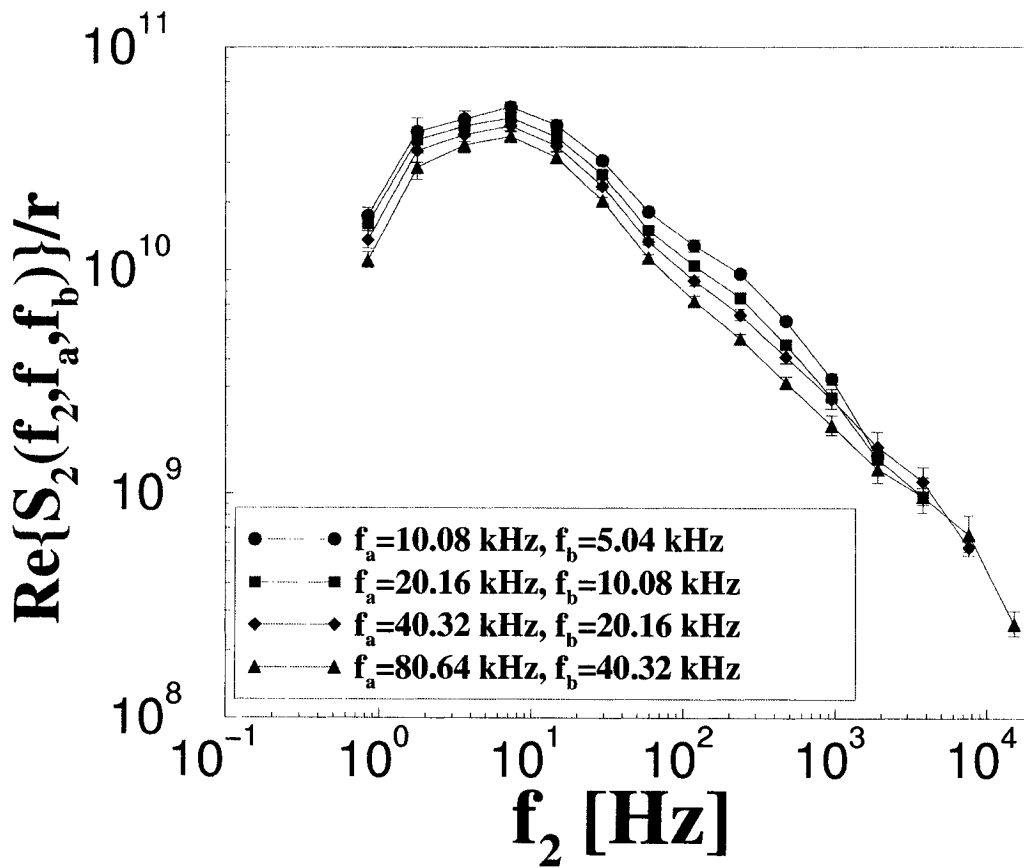
Figure 7.8: We present the real cross second spectra, $Re\{S_2(f_2, f_a, f_b)\}$, for $r = f_a/f_b = \frac{1}{2}$, in experiment. Again, as in the experimental second spectra there is no conspicuous flattening due to the background term, $\Gamma_2^{(N)}(f_b, r = \frac{1}{2})$. However, the separation between the curves vanishes, within error bars, when the background term is subtracted off.

72

(by an amount of 1% to 4%) than the exponents determined in mean field theory. Nevertheless, despite this small deviate, our mean field simulation results agree very well with mean field theory, corroborating our theoretical calculation.

The background components ($\theta = 0$), given by $\Gamma_{1.5}(f_1)$ and $\Gamma_2(f_b, r)$, are given in Fig. 7.4 for mean field theory and the mean field simulation. For the corresponding exponents $Q_{1.5}$ and Q_2 we find excellent agreement between mean field theory and the mean field simulation results. In Appendix H we ascertain the following exponent relation for Q_2 and $Q_{1.5}$:

$$Q_2 = \frac{5 - \tau}{\sigma \nu z} - 2 \tag{7.29}$$

$$Q_{1.5} = \frac{1}{\sigma \nu z} + 1 \tag{7.30}$$

Plugging τ and $1/\sigma \nu z$ (given in [18]) into Eqs. (7.29-7.30) we find exact agreement in mean field theory: $Q_2 = 5$ and $Q_{1.5} = 3$. For the IRM in $d = 3$ we find $Q_2 = 4.40 \pm 0.10$ and $Q_{1.5} = 2.72 \pm 0.03$, in close agreement with the table above. Also, for experiment we find reasonable agreement (within 10%) against the high frequency values for Q_2 and $Q_{1.5}$; using Eqs. (7.29-7.30) and [18] we find $Q_2 = 2.70 \pm 0.05$ (agrees within error bars) and $Q_{1.5} = 4.02 \pm 0.20$ for experiment. Also, the measured experimental values for Q_2 and $Q_{1.5}$ in the table above agree within error bars with the exponents for the IRM.

Interestingly, we notice that the background components for experiment (given in Fig. 7.5) have two scaling regimes: a flatter slope at low frequency, a steeper slope at high frequency, and a transition point at $f_{cross} \simeq 320$ Hz. This change in slope indicates that intra-avalanche correlations are effecting the power at $f_1 < f_{cross}$.

The real 1.5 spectra and the second spectra are given in Figs. (7.1-7.2,7.6-7.7). Since the background term is small for the real 1.5 spectra (for IRM, MF simulation, and experiment) we find that the real 1.5 spectra curves collapse upon themselves, in agreement with Eq. (7.26). The high frequency scaling exponent $V_{1.5}$ for the real 1.5 spectra shows excellent agreement between mean field theory ($V_{1.5} = 2$) and mean field simulation ($V_{1.5} = 1.93 \pm 0.10$). The second spectra (Fig. 7.2) exhibits a conspicuous flattening due to the background term, except in the experimental

73

second spectra (Fig. 7.7) where the flattening in much less pronounced. In order to find the high frequency scaling exponent for the second spectra we do a non-linear curve fit using the equation: $A0*x^{-A1}$+ (theoretical value, $\Gamma_2^{(N)}(f_1)$), where $A0$, and $A1$, are free parameters. We find very good agreement between mean field theory ($V_2 = 2$) and our mean field simulation ($V_2 = 1.92 \pm 0.12$) for our second spectra exponent.

The very weak dependence of the real 1.5 spectra on f_1 and the strong fall off of the second spectra at high frequency suggests that the high frequency power comes from the fine structure of large avalanches ($T >> 1/f_1$, T is the duration) and not small individual pulses ($T \simeq 1/f_1$)[48]. Through simulation we verify this claim in the mean field simulation and IRM. When we subtract all avalanches smaller than $T = T_{max}/4$ from the Barkhausen train (where T_{max} is the duration of the largest avalanche) and then determine the second spectra, we find no change in V_2. However, when we subtract all avalanches larger than $T = T_{max}/4$ from the Barkhausen train, we find that the second spectrum flattens and that there is an evident separation between the real 1.5 spectra curves (i.e. increased f_1 dependence). In experiment we also find a weak dependence of the real 1.5 spectra on f_1 and a strong fall off of the second spectra, however, the second spectra for experiment falls off with an exponent $V_2 = 0.66 \pm 0.12$ versus an exponent of $V_2 = 1.80 \pm 0.05$ for IRM and $V_2 = 2$ for mean field theory. This suggests that the high frequency power in experiment comes from the fine structure of larger pulses to a *lesser degree* than in IRM or mean field theory. With data obtained from Gianfranco Durin we have tested the possibility that the differences in the exponents V_2 and $V_{1.5}$ maybe a result of dipole-dipole interactions, since these interactions decay as a power law they may still be significant at short length scales, thereby resulting in suppressed spin flips that cause otherwise larger avalanches to be broken down into smaller high frequency pulses. However, our analysis found no evidence that dipole-dipole interactions are the culprit.

In Fig. 7.3 we give the real cross second spectra ($r = f_a/f_b = \frac{1}{2}$) for the mean field simulation and the IRM, and in Fig. 7.8 we give the real cross second spectra for experiment (also $r = \frac{1}{2}$). The cross second spectra plots for $r < \frac{1}{2}$ are similar to $r = \frac{1}{2}$, so to avoid redundancy $r < \frac{1}{2}$ plots have been left out. The real cross second spectra not only strongly resemble the second spectra, but we also notice in Table 7.1 that the exponents values for V_2 and V_C (where V_C was determined using the same non-linear curve fit used to find V_2) in mean field theory, the mean field simulation, the

74

IRM, and in the experiment are identical or nearly identical. For the class of models and systems we study the real cross second spectra give no new information, however, the real cross second spectra is useful when studying systems that have different dynamics on different length and time scales [39].

Remarkably, we have found that $Q_{1.5}$ and Q_2 agree (within error bars) for the IRM and experiment. Since $Q_{1.5}$ and Q_2 are directly related to known exponents, as we have found above, they may be obtained from a standard analysis of power spectra $(P(w) \sim w^{-\frac{1}{\sigma \nu z}})$ and the avalanche size distribution $(D(S) \sim S^{-\tau})$ [13]. However, when we compare $V_{1.5}$, V_2, and V_C between the IRM and experiment we find a significant difference, whose origin we are currently investigating.

Thus by utilizing higher order spectra we've not only found novel exponents ($V_{1.5}$, V_2, and V_C), we have also idenfied key differences between the IRM model and our experiment, previously believed to be in excellent agreement. Higher order spectra may also prove as a more rigorous test of other avalanche models against experiment, in particular systems discussed in [40]. Our study of higher order spectra is a powerful tool to further our understanding of noise in disordered systems; ultimately this method of analysis will allow us to develop better theoretical models by identifying differences between model and experiment that cannot be found through the traditional analysis of critical phenomena.

Appendix A

Random Bond Calculation

A.1 Introduction

In this chapter we demonstrate that the mean field Random Bond Ising Model (RBIM) has a continuous phase transition at a critical value of the disorder, R_c. We accomplish this by showing the mean field RBIM has a diverging magnetic susceptibility ($\frac{\partial M}{\partial H} \to 0$), and thereby demonstrating the existence of a critical point. We then identify the corresponding critical disorder, R_c, at which this divergence occurs.

A.2 The Mean Field Random Bond Ising Model

The mean field RBIM consists of an array of N spins ($s_i = \pm 1$), which may point up ($s_i = +1$) or down ($s_i = -1$). Spins are coupled to all other spins (through a ferromagnetic exchange interaction J_{ij}), and to an external field $H(t)$ which is increased adiabatically slowly. To model dirt in the material, we have random bonds, $J_{ij} = 1 + h_{ij}N^{1/2}$, chosen from a distribution $P(h_{ij}) = exp(-\frac{1}{2R^2}h_{ij}^2)/(\sqrt{2\pi}R)$, where R, the disorder, determines the width of the Gaussian probability distribution and therefore gives a measure of the amount of quenched disorder for the system. The Hamiltonian for the system at a time t is given by: $H = -\sum_{ij}\frac{1}{N}(1 + h_{ij}N^{1/2})s_is_j + \sum_i H(t)s_i$. Initially, $H(-\infty) = -\infty$ and all the spins are pointing down. Each spin is always aligned with its local effective field: $h_i^{eff} = N^{-1/2}\sum_j h_{ij}s_j + M + H(t)$, where $M = \frac{1}{N}\sum_i s_i$ is the magnetization of the system.

A.3 Calculation of the Critical Disorder

Since we know when $h_i^{eff} = N^{-1/2}\sum_j h_{ij}s_j + M + H(t) > 0$ means $s_i = +1$ and when $h_i^{eff} = N^{-1/2}\sum_j h_{ij}s_j + M + H(t) < 0$ means $s_i = -1$, we obtain the following self-consistent integral equation for the magnetization:

$$M = \int_{-\infty}^{\infty} \ldots \int_{-\infty}^{\infty} (2*\Theta[\frac{1}{N^{1/2}}\sum_j h_{ij}s_j + M + H] - 1)\prod_{j=1}^{N} P(h_{ij})dh_{ij} \qquad (A.1)$$

Where $\Theta[...]$ is the step function. In Eq. (A.1) we integrate out h_{ij} (in the step function) for $j = 1$ to N by integrating over the probability distribution for each j, that is, $\prod_{j=1}^{N} P(h_{ij})dh_{ij}$.

Next we define a functional called Γ as follows:

$$\Gamma = \int_{-\infty}^{\infty} \cdots \int_{-\infty}^{\infty} \Theta[\frac{1}{N^{1/2}}\sum_j h_{ij}s_j + M + H] \prod_{j=1}^{N} P(h_{ij})dh_{ij} \tag{A.2}$$

Where we have: $M = 2 * \Gamma - 1$. Now to simplify Γ we use the following identity, that expresses the step function as a contour integral around a pole $i\epsilon$:

$$\Theta[x] = \int_{\epsilon \to 0^+} \frac{dw}{2\pi i} \frac{e^{iwx}}{w - i\epsilon} \tag{A.3}$$

With Eq. (A.3) we write Γ as:

$$\Gamma = \int_{-\infty}^{\infty} \cdots \int_{-\infty}^{\infty} \int \frac{dw}{2\pi i} \frac{e^{i(M+H)w}}{w - i\epsilon} e^{-\frac{1}{2R^2}\sum_j (h_{ij}^2 - 2R^2 iwh_{ij}s_j/\sqrt{N})} \prod_{j=1}^{N} \frac{dh_{ij}}{(\sqrt{2\pi}R)^N} \tag{A.4}$$

We now complete the square with respect to h_{ij} in the exponential:

$$\Gamma = \int_{-\infty}^{\infty} \cdots \int_{-\infty}^{\infty} \int \frac{dw}{2\pi i} \frac{e^{i(M+H)w}}{w - i\epsilon} e^{-\frac{1}{2R^2}\sum_j (h_{ij} - R^2 iws_j/\sqrt{N})^2} e^{-\sum_j \frac{R^2 w^2 s_j^2}{2N}} \prod_{j=1}^{N} \frac{dh_{ij}}{(\sqrt{2\pi}R)^N} \tag{A.5}$$

With $s_j^2 = 1$, and integrating over the Gaussian product we obtain:

$$\Gamma = \int \frac{dw}{2\pi i} \frac{e^{i(M+H)w}}{w - i\epsilon} e^{-R^2 w^2/2} \tag{A.6}$$

To find the critical point we must determine the point where the magnetic susceptibility, $\frac{\partial M}{\partial H}$, diverges. Since $\frac{\partial M}{\partial H} = 2 * \frac{\partial \Gamma}{\partial H}$, we look directly at $\frac{\partial \Gamma}{\partial H}$:

$$\frac{\partial \Gamma}{\partial H} = \int iw(\frac{\partial M}{\partial H} + 1)\frac{1}{2\pi i}\frac{e^{iw(M+H)}}{w - ie}e^{-R^2 w^2/2}dw \tag{A.7}$$

$$= \frac{1}{2\pi}(2\frac{\partial \Gamma}{\partial H} + 1)\int e^{iw\alpha}e^{-R^2 w^2/2}dw \tag{A.8}$$

Where $\alpha \equiv M + H$. Let's define:

$$\gamma[\alpha] \equiv \frac{1}{2\pi} \int e^{iw\alpha} e^{-R^2 w^2/2} dw \tag{A.9}$$

$$= \sqrt{\frac{1}{2\pi}} \frac{1}{R} e^{\frac{-\alpha^2}{2R^2}} \tag{A.10}$$

Rewriting Eq. (A.8) we find:

$$\frac{\partial \Gamma}{\partial H} (1 - 2\gamma[\alpha]) = \gamma[\alpha] \tag{A.11}$$

$$\frac{\partial \Gamma}{\partial H} = \frac{\gamma[\alpha]}{1 - 2\gamma[\alpha]} \tag{A.12}$$

In the mean field RBIM we have $M_c = 0$ and $H_c = 0$, since from Eq. (A.6) on this analysis is identical for the mean field RFIM where $M_c = H_c = 0$ [11]. The susceptibility diverges when: $1 - 2\gamma[\alpha] = 0$, thus setting $\alpha = M_c + H_c = 0$ in this equation allows us to find R_c. We first determine $\gamma[0]$:

$$\gamma[0] = \frac{1}{2\pi} \int e^{-R_c^2 w^2/2} dw = \sqrt{\frac{1}{2\pi}} \frac{1}{R_c} \tag{A.13}$$

Thus we have:

$$1 - 2\gamma[0] = 0 \tag{A.14}$$

$$1 - \sqrt{\frac{2}{\pi}} \frac{1}{R_c} = 0 \tag{A.15}$$

$$R_c = \sqrt{\frac{2}{\pi}} \tag{A.16}$$

79

Appendix B

Determination of Orthnormal Polynomials

80

To derive a set of orthonormal polynomials, that fit the scaling functions discussed in chapter 5, we specify the conditions that $f_i(\pm L) = 0$, where the avalanche duration is $T = 2L$, and $\pm L$ are the endpoints, representing when the scaling function begins and ends. We start with a quadratic polynomial, $f_0(t)$, that represents the mean field scaling function (that is a parabola). Also, the polynomials with even indices ($f_i(t)$ where i is even), are even polynomials such that $f_i(-t) = f_i(t)$, and the polynomials with odd indices, are odd polynomials such that $f_i(-t) = -f_i(t)$. By explicitly separating even and odd polynomials we can measure any potential asymmetries in the scaling function.

We use the Graham-Schmidt algorithm to derive the polynomials; to assure the polynomials are orthonormal we have the following requirements:

$$\langle f_i | f_i \rangle \equiv \int_{-L}^{L} f_i(t) f_i(t) dt = 1 \qquad (B.1)$$

and where $i \neq j$:

$$\langle f_i | f_j \rangle \equiv \int_{-L}^{L} f_i(t) f_j(t) dt = 0 \qquad (B.2)$$

We begin with $f_0(t)$ in the form:

$$f_0(t) = A_0 t^2 + A_1 \qquad (B.3)$$

Using $f_0(\pm L) = 0$ we solve for A_1:

$$f_0(L) = A_0 L^2 + A_1 = 0$$

$$A_1 = -A_0 L^2$$

$$f_0(t) = A_0(t^2 - L^2)$$

With the condition $\langle f_0 | f_0 \rangle = 1$ we have:

81

$$A_0^2 \int_{-L}^{L} (t^2 - L^2)dt = 1$$

$$A_0 = \sqrt{\frac{15}{16L^5}}$$

Thus

$$f_0(t) = \sqrt{\frac{15}{16L^5}}(t^2 - L^2) \tag{B.4}$$

To find the next polynomial in the series, $f_1(t)$, we start with:

$$f_1(t) = B_0 t^3 + B_1 t \tag{B.5}$$

Where we have explicitly set this polynomial to be odd. Similar to determining Eq. (B.4), we use the conditions that $f_1(\pm L) = 0$ and $\langle f_1|f_1\rangle = 1$ to determine B_0 and B_1, we find:

$$f_1(t) = \sqrt{\frac{105}{16L^7}}(t^3 - L^2 t) \tag{B.6}$$

The next polynomial, $f_2(t)$, is of the form:

$$f_2(t) = C_0 t^4 + C_1 t^2 + C_2 \tag{B.7}$$

To solve for all three constants C_0, C_1, and C_2 we need to utilize the condition that $\langle f_2|f_0\rangle = 0$, in addition to the conditions that $\langle f_2|f_2\rangle = 1$ and $f_2(\pm L) = 0$. Also, we note that $\langle f_2|f_1\rangle = 0$ automatically, since $f_2(t)$ is an even polynomial and $f_1(t)$ is an odd polynomial. From the conditions that $\langle f_2|f_0\rangle = 0$ and $f_2(\pm L) = 0$ we obtain the following equations:

$$f_2(\pm L) = C_0 L^4 + C_1 L^2 + C_2 = 0 \tag{B.8}$$

$$\langle f_2|f_0\rangle = \int_{-L}^{L} (C_0 t^4 + C_1 t^2 + C_2) f_0(t) dt = 0 \tag{B.9}$$

With Eq. (B.8-B.9) we may solve for C_1, and find $C_1 = -8L^2 C_0/7$. Thus we have:

82

$$f_2(t) = C_0 t^4 - \frac{8}{7} t^2 L^2 C_0 + C_2 \qquad (B.10)$$

Now using $f_2(\pm L) = 0$ with Eq. (B.10) we solve for C_2, and ascertain that $C_2 = L^4 C_0/4$. Finally, we find C_0 with the condition that $\langle f_2|f_2 \rangle = 1$. Thus we have:

$$f_2(t) = \sqrt{\frac{45}{64 L^4}} (7t^4 - 8L^2 t^2 + L^4) \qquad (B.11)$$

The next polynomial, $f_3(t)$, is of the form:

$$f_3(t) = D_0 t^5 + D_1 t^3 + D_2 t \qquad (B.12)$$

We may solve for D_0, D_1, and D_2 just as we solved for C_0, C_1, and C_2. Thus we find:

$$f_3(t) = \sqrt{\frac{1155}{64 L^{11}}} (3t^5 - 4L^2 t^3 + L^4 t) \qquad (B.13)$$

The last polynomial in the series, $f_4(t)$, takes the form:

$$f_4(t) = E_0 t^6 + E_1 t^4 + E_2 t^2 + E_3 \qquad (B.14)$$

To solve for E_0 to E_3 we must have four conditions. The four conditions we need are the following:

$$f_4(\pm L) = 0 \qquad (B.15)$$

$$\langle f_4|f_2 \rangle = 0 \qquad (B.16)$$

$$\langle f_4|f_0 \rangle = 0 \qquad (B.17)$$

$$\langle f_4|f_4 \rangle = 1 \qquad (B.18)$$

Upon evaluating Eq. (B.15-B.18) we obtain four equations with four unknowns that may be determined by any standard matrix method for solving a system of equations. In our approach we use Eq. (B.15-B.16) to solve for E_1 in terms of E_0 and find $E_1 = -51 E_0 L^2/33$. With Eq. (B.17) we

83

get $E_3 = -L^6 E_0/33$, and using Eq. (B.15) again we find $E_2 = 19L^4 E_0/33$. Finally, we determine E_0 using the normalization condition given in Eq. (B.18). Thus we find:

$$f_4(t) = \sqrt{\frac{1365}{2048L^{13}}}(33t^6 - 51L^2t^4 + 19L^4t^2 - L^6) \qquad \text{(B.19)}$$

Appendix C

Calculation of Mean Field Size Distribution and Shape

C.1 Derivation of Mean Field Avalanche Size Distribution

The total probability distribution for an avalanche of duration T in mean field theory is given by [13]:

$$P(n_0 = 1, n_1, n_2, ..., n_T) = \frac{e^{-2J\rho}(2J\rho)^{n_1}}{n_1!} \prod_{t=2}^{T} \frac{e^{-2J\rho n_{t-1}}(2J\rho n_{t-1})^{n_t}}{n_t!} \tag{C.1}$$

where $2J\rho$ represents the average number of spins triggered to flip by the previous (one) spin flip [13]. The probability distribution to have n_i spin flips in the ith shell, given that there were n_{i-1} flips in the $(i-1)$th shell, of the avalanche is given by:

$$P(n_i|n_{i-1}) = \frac{e^{-2J\rho n_{i-1}}(2J\rho n_{i-1})^{n_i}}{n_i!} \tag{C.2}$$

With the above equations (Eq. (C.1-C.2)) and closely following the method described in [40], we derive the mean field avalanche size distribution, and in the next section we derive the mean avalanche shape for avalanches of a fixed size. We let $\langle ... \rangle \equiv \sum_{\{n_1,...,n_T\}} ... P(1, n_1, ..., n_T)$, that is, the average over Eq. (C.1).

We first define a generating functional for Eq. (C.1):

$$\Gamma_T\{\mu_t\} = \sum_{\{n_1,...,n_T\}} e^{i\sum_{t=0}^{T} \mu_t n_t} P(1, n_1, ..., n_T) \tag{C.3}$$

$$= \langle e^{i\sum_{t=0}^{T} \mu_t n_t} \rangle \tag{C.4}$$

Before we evaluate Eq. (C.3) consider that,

$$\langle e^{i\mu_T n_T} \rangle = \langle e^{i\mu_T n_T} | n_{T-1} \rangle \tag{C.5}$$

that means $e^{i\mu_T n_T}$ only depends on n_{T-1}, since n_T, and equivalently a function of n_T, depend only on n_{T-1} (this follows from Eq. (C.1-C.2)). So now we can express $\langle e^{i\mu_T n_T} \rangle$ as:

86

$$\langle e^{i\mu_T n_T} \rangle = \sum_{n_T=0}^{\infty} P(n_T|n_{T-1})e^{i\mu_T n_T} \tag{C.6}$$

$$= \sum_{n_T=0}^{\infty} \frac{e^{-2J\rho n_{T-1}}(2J\rho n_{T-1})^{n_T}e^{i\mu_T n_T}}{n_T!} \tag{C.7}$$

$$= e^{-2J\rho n_{T-1}} \sum_{n_T=0}^{\infty} \frac{(2J\rho n_{T-1}e^{i\mu_T})^{n_T}}{n_T!} \tag{C.8}$$

$$= e^{-2J\rho n_{T-1}}e^{2J\rho n_{T-1}e^{i\mu_T}} \tag{C.9}$$

$$= exp[2J\rho n_{T-1}(e^{i\mu_T} - 1)] \tag{C.10}$$

Now we can rewrite Eq. (C.3) as:

$$\Gamma_T\{\mu_t\} = \langle e^{i\mu_0 n_0}e^{i\mu_1 n_1}...e^{i\mu_{T-1}n_{T-1}}e^{i\mu_T n_T} \rangle \tag{C.11}$$

$$= \langle e^{i\mu_0 n_0}...e^{i\mu_{T-2}n_{T-2}}e^{i(\mu_{T-1}-i2J\rho(e^{i\mu_T}-1))n_{T-1}} \rangle \tag{C.12}$$

Let us define:

$$\lambda_{T-1} = \mu_{T-1} - i2J\rho(e^{i\mu_T} - 1), \tag{C.13}$$

so we have found:

$$\Gamma_T[\mu_0, ..., \mu_T] = \Gamma_{T-1}[\mu_0, ..., \mu_{T-2}, \lambda_{T-1}] \tag{C.14}$$

Next we define:

$$\lambda_{T-1} = \mu_{T-1} - i2J\rho(e^{i\lambda_T} - 1), \tag{C.15}$$

where we have set $\lambda_T = \mu_T$. We can justify this by making our above argument for $T + 1$ time steps. Indeed, performing the above argument (Eq. (C.14)) iteratively we have (where $\{\mu_t\} = [\mu_0, ..., \mu_T]$ and $n_0 = 1$):

87

$$\Gamma_T\{\mu_t\} = \Gamma_0(\lambda_0\{\mu_t\}) = e^{i\lambda_0\{\mu_t\}n_0} \tag{C.16}$$

Considering the limit $T \to \infty$ and setting all $\mu_t = \mu$, for all t (the motivation for this will become clear later), Eq. (C.13) becomes:

$$\lambda_\infty = \mu - i2J\rho(e^{i\lambda_\infty} - 1) \tag{C.17}$$

Eq. (C.17) represents a fixed point equation for λ_∞, which we will later solve to find a stable fixed point solution. However, let us first go back and determine the consequence of setting all $\mu = \mu_t$, for all t, and taking $T \to \infty$. Eq. (C.3) becomes:

$$\Gamma_\infty(\mu) = \sum_{\{n_1,...,n_\infty\}} e^{i\mu\sum_{t=0}^{\infty}n_t} P(1, n_1, ..., n_\infty) \tag{C.18}$$

Notice that the avalanche size, $s = \sum_{t=0}^{\infty} n_t$, thus:

$$\Gamma_\infty(\mu) = \sum_{\{n_1,...,n_\infty\}} e^{i\mu s} P(1, n_1, ..., n_\infty) \tag{C.19}$$

Now since we have taken $T \to \infty$ we can consider the continuum limit for μ when performing the inverse Fourier transform:

$$P(s) = \frac{1}{2\pi} \int_{-\infty}^{\infty} d\mu e^{-i\mu s} \Gamma_\infty(\mu) \tag{C.20}$$

Thus we have determined an expression for the avalanche size distribution. Now let us go back and find λ_∞ (Eq. (C.17)) so we may evaluate Eq. (C.20) with $\Gamma_\infty = e^{i\lambda_\infty}$. Since we are interested in the critical point, we may define $\epsilon \equiv 1 - 2J\rho$, where ϵ is small near criticality and exactly zero at the critical point. To evaluate Eq. (C.17) we Taylor expand $e^{i\lambda_\infty}$ up to $O(\lambda_\infty^2)$ and obtain:

$$\lambda_\infty = \mu - i2J\rho(i\lambda_\infty - \lambda_\infty^2/2) \tag{C.21}$$

$$\epsilon\lambda_\infty = \mu + i2J\rho\lambda_\infty^2/2 \tag{C.22}$$

88

Near the critical point $2J\rho \simeq 1$, so we have:

$$\epsilon\lambda_\infty \simeq \mu + i\lambda_\infty^2/2 \tag{C.23}$$

$$i\lambda_\infty^2/2 - \epsilon\lambda_\infty + \mu = 0 \tag{C.24}$$

We ascertain the stable root is: $\lambda_\infty = -i\epsilon + \sqrt{(-\epsilon^2 + 2i\mu)}$. Now since $\Gamma_\infty(\mu) = e^{i\lambda_\infty}$, we may readily evaluate Eq. (C.20) (setting $e^\epsilon \simeq 1$):

$$P(s) = \frac{1}{2\pi}\int_{-\infty}^{\infty} d\mu e^{-i\mu s} e^{i\lambda_\infty} \tag{C.25}$$

$$\simeq \frac{1}{2\pi}\int_{-\infty}^{\infty} d\mu e^{-i\mu s} e^{i\sqrt{2i(\mu+i\epsilon^2/2)}} \tag{C.26}$$

Taylor expanding $e^{i\sqrt{2i(\mu+i\epsilon^2/2)}} \simeq 1 + i\sqrt{2i(\mu + i\epsilon^2/2)}$, and substituting $\mu' = \mu + i\epsilon^2/2$ we find:

$$P(s) \simeq \frac{1}{2\pi}\int_{-\infty}^{\infty} d\mu' i\sqrt{2i\mu'} e^{-i\mu' s} e^{-s\epsilon^2/2} \tag{C.27}$$

Setting $z = \mu' s$:

$$P(s) \simeq \frac{1}{2\pi}\frac{1}{s^{3/2}} e^{-s\epsilon^2/2}\int_{-\infty}^{\infty} dz i\sqrt{2iz} e^{iz} \tag{C.28}$$

Since the integral is independent of s we have:

$$P(s) \sim \frac{1}{2\pi}\frac{1}{s^{3/2}} e^{-s\epsilon^2/2} \tag{C.29}$$

C.2 Derivation of mean field Avalanche Shape

Closely following a method described in [40] we will utilize $\Gamma_T\{\mu_t\} = e^{i\lambda_0\{\mu_t\}}$ (Eq. (C.16)) to find the universal avalanche shape function for avalanches of a fixed size, $\langle n_t|s\rangle$. First we take $\mu_t = \mu + \nu_t$ and $\mu_T = \mu$, then we have:

89

$$\frac{1}{i}\frac{\partial \Gamma_T}{\partial \nu_t}\Big|_{\nu_t=0} = \langle n_t e^{i\mu s}\rangle = \frac{\partial \lambda_0}{\partial \nu_t}\Big|_{\nu_t=0}e^{i\lambda_0\{\mu\}} \tag{C.30}$$

Now to connect $\langle n_t e^{i\mu s}\rangle$ to $\langle n_t|s\rangle$ we first acknowledge the following (see Eq. (C.3) and (C.20)):

$$P(s) = \frac{1}{2\pi}\int_{-\infty}^{\infty}\langle e^{i\mu s}\rangle e^{-i\mu s}d\mu = \sum_{n_t}Prob(n_t, s) \tag{C.31}$$

From this we ascertain that:

$$\frac{1}{2\pi}\int_{-\infty}^{\infty}\langle n_t e^{i\mu s}\rangle e^{-i\mu s}d\mu = \sum_{n_t}n_t Prob(n_t, s) \tag{C.32}$$

Where $Prob(n_t, s)$ is the probability for n_t and s. We can rewrite $\sum_{n_t}n_t Prob(n_t, s)$ as:

$$\sum_{n_t}n_t Prob(n_t, s) = \sum_{n_t}n_t P(n_t|s)P(s) = \langle n_t|s\rangle P(s) \tag{C.33}$$

$P(n_t|s)$ is the probability of n_t given s. Thus:

$$\langle n_t|s\rangle = \frac{1}{2\pi}\frac{1}{P(s)}\int_{-\infty}^{\infty}\langle n_t e^{i\mu s}\rangle e^{-i\mu s}d\mu \tag{C.34}$$

Now we can evaluate $\frac{\partial \lambda_0}{\partial \nu_t}\Big|_{\nu_t=0}$ using the chain rule:

$$\frac{\partial \lambda_0}{\partial \nu_t} = \frac{\partial \lambda_t}{\partial \mu_t}\frac{\partial \lambda_{t-1}}{\partial \lambda_t}\times ... \times \frac{\partial \lambda_0}{\partial \lambda_1} \tag{C.35}$$

We evaluate Eq. (C.35) with Eq. (C.17) and finally we set $\lambda_t = \lambda_\infty$ (the fixed point), for all t, and $\mu_t = \mu$, for all t. So for each term in the product in Eq. (C.35) we get a factor of $2J\rho e^{i\lambda_\infty}$:

$$\frac{\partial \lambda_0}{\partial \nu_t}\Big|_{\nu_t=0} = (2J\rho e^{i\lambda_\infty})^t \simeq e^{i\lambda_\infty t}, \tag{C.36}$$

where we use the approximation $2J\rho \simeq 1$ near the critical point. Now from Eq. (C.30) it follows that:

$$\frac{\partial \lambda_0}{\partial \nu_t}\Big|_{\nu_t=0}e^{i\lambda_0\{\mu\}} = \langle n_t e^{i\mu s}\rangle = e^{i\lambda_\infty(t+1)}, \tag{C.37}$$

90

where we have taken $\lambda_0\{\mu\} = \lambda_\infty$ in the $T \to \infty$ limit. We are now ready to write down a complete expression for $\langle n_t | s \rangle$ that we can solve, from Eq. (C.34) and (C.37) we have:

$$\langle n_t | s \rangle \simeq \frac{1}{2\pi} \frac{1}{P(s)} \int_{-\infty}^{\infty} e^{i\lambda_\infty (t+1)} e^{-i\mu s} d\mu \qquad (C.38)$$

Now plugging in $\lambda_\infty = -i\epsilon + \sqrt{2i(\mu + i\epsilon^2/2)}$, and taking $\mu' = \mu + i\epsilon^2/2$, we obtain:

$$\langle n_t | s \rangle \simeq \frac{1}{2\pi} \frac{1}{P(s)} \int_{-\infty}^{\infty} e^{-s\epsilon^2/2} e^{-i\mu' s + 2i(t+1)\sqrt{2i\mu'}} d\mu' \qquad (C.39)$$

Now plugging in the expression for $P(s)$ (Eq. (C.29)) we have:

$$\langle n_t | s \rangle \simeq s^{3/2} \int_{-\infty}^{\infty} e^{-i\mu' s + 2i(t+1)\sqrt{2i\mu'}} d\mu' \qquad (C.40)$$

Substituting $\mu' = -ix^2/s$, completing the square with respect to x in the exponential, and finally solving the resulting Gaussian integral we find:

$$\langle n_t | s \rangle \simeq \sqrt{2\pi}(t+1) e^{-\frac{(t+1)^2}{2s}} \qquad (C.41)$$

91

Appendix D

Determination of Omori Law of Aftershock Decay

In this section we derive the Omari law for aftershock decay from our mean field earthquake model in the case of dynamic strenghtening; for introductory details on the model please refer to the first two sections of chapter 4.

In the case of dynamics strengthening, after a primary earthquake, the static failure stress, τ_s, is increased by an amount $\epsilon\langle s\rangle/N$, where $\langle s\rangle$ is the mean avalanche size. Given in terms of moment, the mean avalanche size in mean field theory is simply given by [61]:

$$\langle s\rangle = \int_0^{1/\epsilon^2} s/s^{3/2}ds \sim 1/\epsilon \tag{D.1}$$

Where $1/s^{3/2}$, is $D(s)$, the mean field avalanche size distribution. Now since $\langle s\rangle \sim 1/\epsilon$, the failure stress, τ_s, is then shifted by an amount $1/N$.

In order to produce aftershocks, we assume that the new larger failure stress, which we call τ_f^0, is lowered slowly, logarithmically in time until it returns to its original value, $\tau_s \simeq \tau_f^0 - 1/N$ [73]. More precisely, τ_f^0 decays as follows, where $t = 0$ is the time at the end of the previous earthquake:

$$\tau_f(t) = \tau_f^0(1 - log(1 + t)) \tag{D.2}$$

Now we define $\eta(t)$ as the amount τ_f^0 has been lowered:

$$\eta(t) = \tau_f^0 - \tau_f(t) = \tau_f^0 log(1 + t) \tag{D.3}$$

Eq. (D.2) is only accurate to first order since lowering the threshold triggers on average $\sim \eta(t)$ aftershocks (assuming nonsingular stress distributions). Since aftershocks are happening quickly compared to the weaking time scale, the aftershocks that are triggered due to lowering the threshold will cause $\tau_f(t)$ to shift up by: $\eta(t) \times \epsilon\langle s\rangle/N \sim \eta(t)/N$. So now the expression for $\tau_f(t)$ becomes:

$$\tau_f(t) = \tau_f^0(1 - log(1 + t)) + \eta(t)/N \tag{D.4}$$

Thus Eq. (D.3) becomes:

$$\eta(t) = \tau_f^0 log(1 + t) - \eta(t)/N \tag{D.5}$$

93

$$\eta(t) = \frac{\tau_f^0 log(1+t)}{1 + 1/N} \tag{D.6}$$

Now we define the number of aftershocks triggered by time t as: $A(t) \sim \eta(t)$. Thus we obtain the Omari law for aftershock decay [21, 22]:

$$\frac{\partial A(t)}{\partial t} \sim \frac{\tau_f^0}{(1+t)(1+1/N)} \tag{D.7}$$

For large t and large N we have:

$$\frac{\partial A(t)}{\partial t} \sim \frac{\tau_f^0}{t} \tag{D.8}$$

94

Appendix E

Calculation of Correlation Functions in MFT

E.1 Poisson distribution Relations

We first derive several useful relations from the Poisson distribution, which we then use to derive the 3-pt and 4-pt time-time correlation function for an avalanche in mean field theory. The Poisson distribution for a shell within an avalanche in mean field theory (at criticality) is given by [13]:

$$P(n_i|n_{i-1}) = \frac{e^{-n_{i-1}} n_{i-1}^{n_i}}{n_i!} \tag{E.1}$$

For simplicity we let $x = n_{i-1}$ and $n = n_i$, so we have:

$$P(n|x) = \frac{e^{-x} x^n}{n!} \tag{E.2}$$

Also, let $\langle ... \rangle = \sum_{n=0}^{\infty} ... \frac{e^{-x} x^n}{n!}$. Now, by the definition of e^{-x}:

$$\langle 1 \rangle = \sum_{n=0}^{\infty} \frac{e^{-x} x^n}{n!} = 1 \tag{E.3}$$

Now differentiating with respect to x we find:

$$\frac{\partial}{\partial x} \left[\sum_{n=0}^{\infty} \frac{e^{-x} x^n}{n!} \right] = \frac{\partial}{\partial x} 1$$

$$\sum_{n=0}^{\infty} \frac{n e^{-x} x^{n-1}}{n!} - \sum_{n=0}^{\infty} \frac{e^{-x} x^n}{n!} = 0$$

$$\sum_{n=0}^{\infty} \frac{n e^{-x} x^n}{n!} = x \sum_{n=0}^{\infty} \frac{e^{-x} x^n}{n!}$$

$$\sum_{n=0}^{\infty} \frac{n e^{-x} x^n}{n!} = x \tag{E.4}$$

$$\langle n \rangle = x \tag{E.5}$$

Next to find $\langle n^2 \rangle$ we differentiate Eq. (E.4):

$$\frac{\partial}{\partial x} \left[\sum_{n=0}^{\infty} \frac{n e^{-x} x^n}{n!} \right] = \frac{\partial}{\partial x} x$$

96

$$\sum_{n=0}^{\infty} \frac{n^2 e^{-x} x^{n-1}}{n!} - \sum_{n=0}^{\infty} \frac{ne^{-x} x^n}{n!} = 1$$

$$\sum_{n=0}^{\infty} \frac{n^2 e^{-x} x^{n-1}}{n!} = \langle n \rangle + 1$$

$$\sum_{n=0}^{\infty} \frac{n^2 e^{-x} x^n}{n!} = x\langle n \rangle + x$$

$$\sum_{n=0}^{\infty} \frac{n^2 e^{-x} x^n}{n!} = x^2 + x \tag{E.6}$$

$$< n^2 >= x^2 + x \tag{E.7}$$

We continue by differentiating Eq. (E.6) to find $< n^3 >$:

$$\frac{\partial}{\partial x} \Big[\sum_{n=0}^{\infty} \frac{n^2 e^{-x} x^n}{n!} \Big] = \frac{\partial}{\partial x}(x^2 + x)$$

$$\sum_{n=0}^{\infty} \frac{n^3 e^{-x} x^{n-1}}{n!} - \sum_{n=0}^{\infty} \frac{n^2 e^{-x} x^n}{n!} = 2x + 1$$

$$\sum_{n=0}^{\infty} \frac{n^3 e^{-x} x^{n-1}}{n!} = \langle n^2 \rangle + 2x + 1$$

$$\sum_{n=0}^{\infty} \frac{n^3 e^{-x} x^n}{n!} = x\langle n^2 \rangle + x(2x + 1)$$

$$\sum_{n=0}^{\infty} \frac{n^3 e^{-x} x^n}{n!} = x(x^2 + x) + x(2x + 1)$$

$$\sum_{n=0}^{\infty} \frac{n^3 e^{-x} x^n}{n!} = x^3 + 3x^2 + x \tag{E.8}$$

$$< n^3 >= x^3 + 3x^2 + x \tag{E.9}$$

Finally, we differentiate Eq. (E.8) to find $< n^4 >$:

$$\frac{\partial}{\partial x} \Big[\sum_{n=0}^{\infty} \frac{n^3 e^{-x} x^n}{n!} \Big] = \frac{\partial}{\partial x}(x^3 + 3x^2 + x)$$

$$\sum_{n=0}^{\infty} \frac{n^4 e^{-x} x^{n-1}}{n!} - \sum_{n=0}^{\infty} \frac{n^3 e^{-x} x^n}{n!} = 3x^2 + 6x + 1$$

$$\sum_{n=0}^{\infty} \frac{n^4 e^{-x} x^{n-1}}{n!} = < n^3 > +3x^2 + 6x + 1$$

97

$$\sum_{n=0}^{\infty} \frac{n^4 e^{-x} x^n}{n!} = x < n^3 > + x(3x^2 + 6x + 1)$$

$$\sum_{n=0}^{\infty} \frac{n^4 e^{-x} x^n}{n!} = x(x^3 + 3x^2 + x) + x(3x^2 + 6x + 1)$$

$$\sum_{n=0}^{\infty} \frac{n^4 e^{-x} x^n}{n!} = x^4 + 6x^3 + 7x^2 + x \tag{E.10}$$

$$\langle n^4 \rangle = x^4 + 6x^3 + 7x^2 + x \tag{E.11}$$

E.2   Calculation of Correlation functions

From Eqs. (E.5, E.7, E.9, E.11) we have the following recursion relations for an avalanche in MFT (Eq. (7.1)):

$$< n_j > \;=\; < n_{j-1} > \tag{E.12}$$

$$< n_j^2 > \;=\; < n_{j-1}^2 > + < n_{j-1} > \tag{E.13}$$

$$< n_j^3 > \;=\; < n_{j-1}^3 > + 3 < n_{j-1}^2 > + < n_{j-1} > \tag{E.14}$$

$$< n_j^4 > \;=\; < n_{j-1}^4 > + 6 < n_{j-1}^3 > + 7 < n_{j-1}^2 > + < n_{j-1} > \tag{E.15}$$

Using the fact that $n_o \equiv 1$ we determine the following initial conditions:

$$< n_1 > \;=\; 1 \tag{E.16}$$

$$< n_1^2 > \;=\; 2 \tag{E.17}$$

$$< n_1^3 > \;=\; 5 \tag{E.18}$$

$$< n_1^4 > \;=\; 15 \tag{E.19}$$

Using the recursion relations and initial conditions we can find the explicit functionality of $< n_j^2 >$, $< n_j^3 >$, and $< n_j^4 >$:

98

$$\begin{aligned}
< n_j^2 > \ &= \ < n_{j-1}^2 > + < n_{j-1} > \\
&= \ < n_{j-2}^2 > + < n_{j-2} > + < n_{j-1} > \\
\ldots \ &= \ < n_1^2 > + \sum_{m=1}^{j-1} < n_{j-m} > \\
&= \ 2 + \sum_{m=1}^{j-1} 1 \\
&= \ j + 1
\end{aligned}$$

Thus we verify Eq. (7.4):

$$< n_j n_{j+k} > = < n_j^2 > = j + 1 \tag{E.20}$$

Now let us consider:

$$\begin{aligned}
< n_j^3 > \ &= \ < n_{j-1}^3 > + 3 < n_{j-1}^2 > + < n_{j-1} > \\
&= \ < n_{j-2}^3 > + 3(< n_{j-2}^2 > + < n_{j-1}^2 >) + < n_{j-1} > + < n_{j-2} > \\
\ldots \ &= \ < n_1^3 > + 3\sum_{m=1}^{j-1} < n_{j-m}^2 > + \sum_{m=1}^{j-1} < n_{j-m} > \\
&= \ 5 + 3\sum_{m=1}^{j-1}(j - m + 1) + \sum_{m=1}^{j-1} 1 \\
&= \ \frac{1}{2}(3j^2 + 5j + 2)
\end{aligned}$$

Thus we find:

$$< n_j^3 > = \frac{1}{2}(3j^2 + 5j + 2) \tag{E.21}$$

Now let us find $< n_j^4 >$:

$$< n_j^4 > \ = \ < n_{j-1}^4 > + 6 < n_{j-1}^3 > + 7 < n_{j-1}^2 > + < n_{j-1} >$$

99

$$= 15 + \sum_{m=1}^{j-1} [6 < n_{j-m}^3 > +7 < n_{j-m}^2 > + < n_{j-m} >]$$

$$= \frac{1}{2}(6j^3 + 13j^2 + 9j + 2)$$

So we have:

$$< n_j^4 > = \frac{1}{2}(6j^3 + 13j^2 + 9j + 2) \tag{E.22}$$

Now let us look at the case where $l \geq k \geq 0$:

$$
\begin{aligned}
< n_j n_{j+k} n_{j+l} > &= < n_i n_{j+k}^2 > \\
&= < n_j(n_{j+k-1} + n_{j+k-1}^2) > \\
&= < n_j^2 > + < n_j n_{j+k-1}^2 > \\
&= 2 < n_j^2 > + < n_j n_{j+k-2}^2 > \\
&\quad \cdots \\
&= k < n_j^2 > + < n_j^3 >
\end{aligned}
$$

Thus:

$$< n_j n_{j+k} n_{j+l} > = < n_j^3 > + k < n_j^2 > \tag{E.23}$$

Now let's look at the most general situation where $m \geq l \geq k \geq 0$:

$$
\begin{aligned}
< n_j n_{j+k} n_{j+l} n_{j+m} > &= < n_j n_{j+k} n_{j+l}^2 > \\
&= < n_j n_{j+k}(n_{j+l-1}^2 + n_{j+l-1}) > \\
&= < n_j n_{j+k}^2 > + < n_j n_{j+k} n_{j+l-1}^2 > \\
&= < n_j n_{j+k}^2 > + < n_j n_{j+k}(n_{j+l-2}^2 + n_{j-l-2}) > \\
&= 2 < n_j n_{j+k}^2 > + < n_j n_{j+k} n_{j+l-2}^2 >
\end{aligned}
$$

100

$$\cdots$$

$$= (l-k) < n_j n_{j+k}^2 > + < n_j n_{j+k}^3 >$$

$$= (l-k)[< n_j^3 > +k < n_j^2 >] + < n_j n_{j+k}^3 >$$

Now let's determine $< n_j n_{j+k}^3 >$:

$$< n_j n_{j+k}^3 > = < n_j(n_{j+k-1}^3 + 3n_{j+k-1}^2 + n_{j+k-1}) >$$

$$= < n_j n_{j+k-1}^3 > +3 < n_j n_{j+k-1}^2 > + < n_j n_{j+k-1} >$$

$$\cdots$$

$$= < n_j^4 > +3 \sum_{m=1}^{k-1} < n_j n_{j+m}^2 > +k < n_j^2 >$$

$$= < n_j^4 > +3 \sum_{m=1}^{k-1} [< n_j^3 > +m < n_j^2 >] + k < n_j^2 >$$

$$= < n_j^4 > +3k < n_j^3 > +\frac{k}{2}(3k-1) < n_j^2 >$$

Thus combining the above results we verify Eq. (7.7):

$$< n_j n_{j+k} n_{j+l} n_{j+m} >=< n_j^4 > +(2k+l) < n_j^3 > +\frac{k}{2}(k+2l-1) < n_j^2 > \qquad (E.24)$$

101

Appendix F

Time Ordered Products

In order to evaluate Eq. (7.11) we need to consider the time ordering of the indices of n, consider the following $(i < N)$:

$$\tilde{y} = n_1 + n_2 + \ldots + n_{N-1} + n_N \tag{F.1}$$

$$x_i = n_i + n_{i+1} + \ldots + n_{N-1} + n_N \tag{F.2}$$

Now we want to evaluate $\tilde{y}^2$, $\tilde{y}^3$, $\tilde{y}^4$ we must write the expansion as a sum of time-ordered products, here's how we do it:

$$\tilde{y}^2 = (n_1 + x_2)^2 = n_1^2 + 2n_1 x_2 + x_2^2 \tag{F.3}$$

$$x_2^2 = (n_2 + x_3)^2 = n_2^2 + 2n_2 x_3 + x_3^2 \tag{F.4}$$

$$x_3^2 = (n_3 + x_4)^2 = n_3^2 + 2n_3 x_4 + x_4^2 \tag{F.5}$$

$$\ldots$$

Thus by we can write Eq. (F.3) as:

$$\tilde{y}^2 = \sum_{i=1}^{N} [n_i^2 + 2n_i x_{i+1}] \tag{F.6}$$

$$= \sum_{i=1}^{N} [n_i^2 + 2n_i \sum_{j=i+1}^{N} n_j] \tag{F.7}$$

So we see that we have successfully written $\tilde{y}^2$ as a sum of time-ordered products. Now we can easily evaluate $< \tilde{y}^2 >$ using Eqs. (7.3)-(7.4). This remarkable method can be used for higher powers to evaluate $\tilde{y}^3$, and $\tilde{y}^4$.

103

Appendix G

Higher Order Spectra Calculation

G.1   Second Spectra

We first rewrite the second spectra as the follows:

$$S_2(\omega, N) = \frac{\langle F_i\{H(i,N)\}F_i\{H(i,N)\}\rangle}{\langle H(i,N)\rangle_i^2} \tag{G.1}$$

$$= \frac{\sum\limits_{\theta=0}^{T/N-1} e^{2\pi i\theta\omega N/T} \sum\limits_{i=0}^{T/N-1-\theta} \langle H(i,N)H(i+\theta,N)\rangle}{\langle H(i,N)\rangle_i^2} \tag{G.2}$$

$$\tag{G.3}$$

Where $i = t/N$, $\langle ... \rangle_i$ denotes sum over i ($\sum_{i=0}^{T/N-1}$), and $F_i\{..\}$ represents the discrete Fourier transform over i. The variable ω is conjugate variable to i in the Fourier transform; $f_2 = \omega/N$ is conjugate to t (the original time) since $t = Ni$. We will use ω in subsequent calculations for consistency and do a change of variable to f_2 in our final expression. Also, we have set $\Delta t = 1$.

Let's first consider the second spectra, when $\theta > 0$ we have:

$$\langle H(i+\theta, N)H(i,N)\rangle = \langle (\tilde{x}_{i+\theta}^+(N) - \tilde{x}_{i+\theta}^-(N))^2 (\tilde{x}_i^+(N) - \tilde{x}_i^-(N))^2 \rangle \tag{G.4}$$

This product is already partially time ordered since we know $\theta > 0$, however when $\theta = 0$:

$$\langle H(i,N)^2 \rangle = \langle (\tilde{x}_i^+(N) - \tilde{x}_i^-(N))^4 \rangle \tag{G.5}$$

In this case since $\theta = 0$ no simplification can be made, there is no partial time ordering like in the case of Eq. (G.4).

We begin by evaluating Eq. (G.5), which can be written as a sum of 4-pt functions (Eq.(7.7)). To write Eq. (G.5) as a sum of 4-pt functions we must use the method discussed in Appendix F, which allows us to write any power of $\tilde{x}_i^{\pm}(N)$ as a sum of time ordered products in n:

$$\langle H(i,N)^2 \rangle$$

$$= \langle (\tilde{x}_i^+ - \tilde{x}_i^-)^4 \rangle$$

105

$$= \langle (\tilde{x}_i^+)^4 - 4(\tilde{x}_i^+)^3 \tilde{x}_i^- + 6(\tilde{x}_i^+)^2 (\tilde{x}_i^-)^2 - 4\tilde{x}_i^+ (\tilde{x}_i^-)^3 + (\tilde{x}_i^-)^4 \rangle$$

$$= \sum_{j=0}^{N/2-1} \left[\Big[4(N/2 - 1 - j) + 1 \Big] \langle n_{iN+j}^4 \rangle + 6 \sum_{k=j+1}^{N/2-1} \Big[2(N/2 - 1 - k) + 1 \Big] \langle n_{iN+j}^2 n_{iN+k}^2 \rangle \right.$$

$$\left. + 4 \sum_{k=j+1}^{N/2-1} \Big[(3(N/2 - 1 - k) + 1) \langle n_{iN+j} n_{iN+k}^3 \rangle + 3 \sum_{l=k+1}^{N/2-1} (2(N/2 - 1 - l) + 1) \langle n_{iN+j} n_{iN+k} n_{iN+l}^2 \rangle \Big] \right]$$

$$- 2N \sum_{j=0}^{N-1} \left[\langle n_{iN+j}^4 \rangle + \sum_{l=j+1}^{N/2-1} \Big[3 \langle n_{iN+j}^2 n_{iN+l}^2 \rangle + 3 \langle n_{iN+j} n_{iN+l}^3 \rangle + 6 \sum_{m=l+1}^{N/2-1} \langle n_{iN+j} n_{iN+l} n_{iN+m}^2 \rangle \Big] \right]$$

$$+ 6 \sum_{j=0}^{N/2-1} \sum_{k=N/2}^{N-1} \Big[2(N - 1 - k) + 1 \Big] \Big[\langle n_{iN+j}^2 n_{iN+k}^2 \rangle + 2 \sum_{l=j+1}^{N/2-1} \langle n_{iN+j} n_{iN+l} n_{iN+k}^2 \rangle \Big]$$

$$- 4 \sum_{j=0}^{N/2-1} \sum_{k=N/2}^{N-1} \left[(3(N - 1 - k) + 1) \langle n_{iN+j} n_{iN+k}^3 \rangle + 3 \sum_{l=k+1}^{N-1} (2(N - 1 - l) + 1) \langle n_{iN+j} n_{iN+k} n_{iN+l}^2 \rangle \right]$$

$$+ \sum_{j=N/2}^{N-1} \left[\Big[4(N/2 - 1 - j) + 1 \Big] \langle n_{iN+j}^4 \rangle + 6 \sum_{k=j+1}^{N-1} \Big[2(N/2 - 1 - k) + 1 \Big] \langle n_{iN+j}^2 n_{iN+k}^2 \rangle \right.$$

$$\left. + 4 \sum_{k=j+1}^{N-1} \Big[(3(N - 1 - k) + 1) \langle n_{iN+j} n_{iN+k}^3 \rangle + 3 \sum_{l=k+1}^{N-1} (2(N - 1 - l) + 1) \langle n_{iN+j} n_{iN+k} n_{iN+l}^2 \rangle \Big] \right]$$

Performing the above sum we find:

$$\langle H(i,N)^2 \rangle$$
$$= \frac{N \left[64 + 56(21 - 20i)N^2 - 420N^3 + 14(58 + 80i)N^4 - 105N^5 + 4(61 + 70i)N^6 \right]}{13440} \tag{G.6}$$

Finally summing over i we obtain:

$$\Gamma_2(N) = \sum_{i=0}^{T/N-1} \langle H(i,N)^2 \rangle \tag{G.7}$$

$$= \frac{1}{96} N(N^2 + 2)^2 T^2 + O(T)$$

$$\simeq \frac{1}{96} N^5 T^2$$

Now let's consider the case where $\theta > 0$:

106

$$\langle H(i+\theta, N)H(i, N)\rangle$$

$$= \langle (\tilde{x}_i^+(N) - \tilde{x}_i^-(N))^2 (\tilde{x}_{i+\theta}^+(N) - \tilde{x}_{i+\theta}^-(N))^2 \rangle$$

$$= \left[\sum_{l=0}^{N/2-1} \left[2(N/2 - 1 - l) + 1 - N \right] + \sum_{l=N/2}^{N-1} \left[2(N - 1 - l) + 1 \right] \right] \times$$

$$\left[\sum_{j=0}^{N/2-1} \left[2 \sum_{k=j+1}^{N/2-1} \langle n_{iN+j} n_{iN+k} n_{(i+\theta)N+l}^2 \rangle + \langle n_{iN+j}^2 n_{(i+\theta)N+l}^2 \rangle \right] - 2 \sum_{j=0}^{N/2-1} \sum_{k=N/2}^{N-1} \langle n_{iN+j} n_{iN+k} n_{(i+\theta)N+l}^2 \rangle \right.$$

$$\left. + \sum_{j=N/2}^{N-1} \left[2 \sum_{k=j+1}^{N-1} \langle n_{iN+j} n_{iN+k} n_{(i+\theta)N+l}^2 \rangle + \langle n_{iN+j}^2 n_{(i+\theta)N+l}^2 \rangle \right] \right]$$

$$= \frac{1}{576} N^3 (N^2 + 2)(5N^2 + 4 + 4i(N^2 + 2))$$

After summing over i and performing Fourier transform we find:

$$\sum_{\theta=1}^{T/N-1} e^{2\pi i \theta \omega / T} \sum_{t=0}^{T/N-1-\theta} \langle H(t+\theta, N)H(t, N)\rangle$$
$$= \frac{N^2(N^2+2)^2 T}{144 \omega^2}$$

From Eq.(7.16) we know $\langle H(i, N)\rangle_t^2 = \frac{T^2}{144}(N^2 + 2)^2$, also $f_2 = \omega/N$, and $f_1 = 1/N$, so finally we obtain:

$$S_2(f_2, f_1) \simeq \frac{1}{Tf_2^2} + \frac{2}{3f_1} \tag{G.8}$$

G.2 1.5 Spectra

We first rewrite the 1.5 spectra equation in a form we may analytically evaluate:

$$S_{1.5}(\omega, N) = \frac{\langle F_i\{v(i, N)\} F_i\{H(i, N)\}\rangle}{\langle H(i, N)\rangle_i} \tag{G.9}$$

107

$$
= \frac{\displaystyle\sum_{\theta=0}^{T/N-1} e^{2\pi i\theta\omega N/T} \sum_{i=0}^{T/N-1-\theta} \langle v(i,N)H(i+\theta,N)\rangle}{\langle H(i,N)\rangle_i} \tag{G.10}
$$

Where $v(i,N) \equiv \tilde{x}_i^+(N) + \tilde{x}_i^-(N)$. Now we consider the 1.5 spectra, when $\theta = 0$ we have:

$$
\Gamma_{1.5}(N) = \sum_{i=0}^{T/N-1} \langle v(t,N)H(i,N)\rangle = \left[\sum_{l=0}^{N/2-1} n_{iN+l} + \sum_{l=N/2}^{N-1} n_{iN+l} \right] (\tilde{x}_i^+(N) - \tilde{x}_i^-(N))^2
$$

$$
= \sum_{i=0}^{T/N-1} \left[\sum_{j=0}^{N/2-1} \left[(3(N/2-1-j)+1)\langle n_{iN+j}^3 \rangle + \sum_{k=j+1}^{N/2-1} 3(2(N/2-1-k)+1)\langle n_{iN+j}^2 n_{iN+k}\rangle \right] \right.
$$

$$
\left. -N/2 \sum_{j=0}^{N/2-1} \left[\langle n_{iN+j}^3 \rangle + 2\sum_{k=j+1}^{N/2-1} \langle n_{iN+j} n_{iN+k}^2 \rangle \right] - \sum_{j=0}^{N/2-1} \sum_{k=N/2}^{N-1} \left[2(N-1-k)\langle n_{iN+j} n_{iN+k}^2 \rangle \right] \right]
$$

$$
= \frac{1}{24} N(N^2+2)T^2 + O(T)
$$

$$
\simeq \frac{1}{24} N^3 T^2
$$

For the case $\theta > 0$ we find:

$$
\langle v(i,N)H(i+\theta,N)\rangle = \sum_{l=0}^{N-1} n_{iN+l}(\tilde{x}_{i+\theta}^+(N) - \tilde{x}_{i+\theta}^-(N))^2
$$

$$
= \sum_{l=0}^{N-1} \left[\sum_{j=0}^{N/2-1} \left[(2(N/2-1-j)+1-N \right] \langle n_{iN+l} n_{(i+\theta)N+j}^2 \rangle \right.
$$

$$
\left. + \sum_{j=N/2}^{N-1} \left[2(N-1-j)+1 \right] \langle n_{iN+l} n_{(i+\theta)N+j}^2 \rangle \right]
$$

$$
= \frac{1}{24} N(N^2+2)(2Ni+N+1)
$$

After summing over i, performing Fourier transform, and taking the real part we find:

$$
Re\{ \sum_{\theta=1}^{T/N-1} e^{2\pi i\theta\omega/T} \sum_{i=0}^{T/N-1-\theta} \langle v(i,N)H(i+\theta,N)\rangle \}
$$

$$
= \frac{N^2(N^2+2)T}{12\omega^2}
$$

108

Now we normalize the result with $\langle H(i, N)\rangle_t = \frac{T}{12}(N^2 + 2)$, and substitute $f_2 = \omega/N$, and $f_1 = 1/N$.

$$Re\{S_{1.5}(f_2, f_1)\} = \frac{1}{f_2^2} + \frac{f_1}{2}T \qquad (G.11)$$

G.3   Cross Second Spectra

We rewrite the cross second spectra as follows:

$$S_2(\omega, M, N) = \frac{\langle F_j\{(j, M)\}F_i\{H(i, N)\}\rangle}{\langle H(i, N)\rangle_i \langle H(j, M)\rangle_j}$$

$$= \frac{\sum\limits_{\theta=0}^{T/N-1} e^{2\pi i \theta \omega N/T} \sum\limits_{i=0}^{T/N-1-\theta} \frac{M}{N} \sum\limits_{j=N(i-1)/M+1}^{Ni/M} \langle H(j, M)H(i + \theta, N)\rangle}{\langle H(i, N)\rangle_i \langle H(j, M)\rangle_j} \qquad (G.12)$$

Where $M = \frac{1}{f_b}$, $N = \frac{1}{f_a}$, and $\langle ...\rangle_j$ denotes sum over j ($\sum_{j=0}^{T/M-1}$), Before we calculation of the cross second spectra we find it useful to define the following notation:

$$\tilde{y}_j^-(M) = \sum_{l=M/2}^{M-1} n_{Mj+l}$$

$$\tilde{y}_j^+(M) = \sum_{l=0}^{M/2-1} n_{Mj+l}$$

$$a = Ni/M$$

$$b = N(2i + 1)/(2M) - 1$$

$$c = N(i + 1)/M - 1$$

$$\tilde{x}_i^-(N) = \sum_{k=b+1}^{c} (\tilde{y}_k^+(M) + \tilde{y}_k^-(M)) = \sum_{j=N/2}^{N-1} n_{Ni+j}$$

$$\tilde{x}_i^+(N) = \sum_{k=a}^{b} (\tilde{y}_k^+(M) + \tilde{y}_k^-(M)) = \sum_{j=0}^{N/2-1} n_{Ni+j}$$

$$Y_k = \tilde{y}_k^+(M) + \tilde{y}_k^-(M)$$

$$X_j = \tilde{y}_j^+(M) - \tilde{y}_j^-(M)$$

109

Again first we consider case where $\theta = 0$, using the notation above we have:

$$\Gamma_2(N, r) = \sum_{i=0}^{T/N-1} \frac{M}{N} \sum_{j=a}^{c} \langle H(j, M) H(i, N) \rangle \qquad (G.13)$$

$$= \sum_{i=0}^{T/N-1} \frac{M}{N} \sum_{j=a}^{c} \langle (\tilde{y}_j^+(M) - \tilde{y}_j^-(M))^2 (\tilde{x}_i^+(N) - \tilde{x}_i^-(N))^2 \rangle \qquad (G.14)$$

$$= \frac{M}{N} \sum_{i=0}^{T/N-1} \sum_{j=a}^{c} X_j^2 \Big[\sum_{j=a}^{b} Y_k - \sum_{j=b+1}^{c} Y_k \Big]^2 \qquad (G.15)$$

$$= \frac{M}{N} \sum_{i=0}^{T/N-1} \Big[\sum_{j=a}^{b} X_j^2 + \sum_{j=b+1}^{c} X_j^2 \Big] \Big[\sum_{j=a}^{b} Y_k - \sum_{j=b+1}^{c} Y_k \Big]^2 \qquad (G.16)$$

Now we make the follow approximation for Eq. (G.16), we simplify the limits by setting $N/M = 2$ in the limits. By deduction this approximation will preserve the scaling for any N/M (multiples of 2) in our final answer. Using $N/M = 2$ to simplify the limits we find:

$$a = 2i$$

$$b = 2i$$

$$c = b + 1 = 2i + 1$$

We now expand Eq. (G.16):

$$\Gamma_2(N) = \frac{M}{N} \sum_{i=0}^{T/N-1} \left(X_{2i}^2 + X_{2i+1}^2 \right) \left(Y_{2i} - Y_{2i+1} \right)^2$$

$$= \frac{M}{N} \sum_{i=0}^{T/N-1} \left(X_{2i}^2 Y_{2i}^2 + X_{2i+1}^2 Y_{2i+1}^2 + X_{2i+1}^2 Y_{2i}^2 + X_{2i}^2 Y_{2i+1}^2 - 2X_{2i}^2 Y_{2i} Y_{2i+1} - 2X_{2i+1}^2 Y_{2i+1} Y_{2i} \right)$$

We evaluate the above terms below as a function of k, where k represents either $2i$ or $2i + 1$:

110

$$X_{k+1}^2 Y_{k+1} Y_k$$

$$= \sum_{m=0}^{M-1} \sum_{q=M/2}^{M-1} \left[\left[3(M-1-q)+1 \right] \langle n_{kM+m} n_{(k+1)M+q}^3 \rangle \right.$$

$$\left. +3 \sum_{l=q+1}^{M-1} \left[2(M-1-l)+1 \right] \langle n_{kM+m} n_{(k+1)M+q} n_{(k+1)M+l}^2 \rangle \right]$$

$$- \sum_{m=0}^{M-1} \sum_{l=M/2}^{M-1} \sum_{q=0}^{M/2-1} \left[\left[2(M-1-l)+1 \right] \langle n_{kM+m} n_{(k+1)M+q} n_{(k+1)M+l}^2 \rangle \right]$$

$$-M \sum_{m=0}^{M-1} \sum_{l=0}^{M/2-1} \left[\langle n_{kM+m} n_{(k+1)M+l}^3 \rangle + 2 \sum_{q=l+1}^{M/2-1} \langle n_{kM+m} n_{(k+1)M+l} n_{(k+1)M+q}^2 \rangle \right]$$

$$+ \sum_{m=0}^{M-1} \sum_{q=0}^{M/2-1} \left[\left[3(M/2-1-q)+1 \right] \langle n_{kM+m} n_{(k+1)M+q}^3 \rangle \right.$$

$$\left. +3 \sum_{l=q+1}^{M/2-1} \left[2(M/2-1-l)+1 \right] \langle n_{kM+m} n_{(k+1)M+q} n_{(k+1)M+l}^2 \rangle \right]$$

$$X_{k+1}^2 Y_k^2$$

$$= \left[\sum_{m=0}^{M/2-1} \left[2(M/2-1-m)+1-M \right] + \sum_{m=M/2}^{M-1} \left[2(M-1-m)+1 \right] \right]$$

$$\times \left[\sum_{n=0}^{M-1} \left(\langle n_{kM+n}^2 n_{(k+1)M+m}^2 \rangle + 2 \sum_{l=n+1}^{M-1} \langle n_{kM+n} n_{kM+l} n_{(k+1)M+n}^2 \rangle \right) \right]$$

$$X_k^2 Y_k^2$$

$$= \sum_{j=M/2}^{M-1} \left[\left[4(M-1-j)+1 \right] \langle n_{Mk+j}^4 \rangle \right.$$

$$+6 \sum_{m=j+1}^{M-1} \left[2(M-1-m)+1 \right] \langle n_{Mk+j}^2 n_{Mk+m}^2 \rangle$$

$$+ \sum_{m=j+1}^{M-1} 4 \left[\left(3(M-1-m)+1 \right) \langle n_{Mk+j} n_{Mk+m}^3 \rangle \right.$$

111

$$+ \sum_{l=m+1}^{M-1} 3\Big(2(M-1-l)+1\Big)\langle n_{Mk+j}n_{Mk+m}n_{Mk+l}^2\rangle\Bigg]\Bigg]$$

$$-2\sum_{j=0}^{M/2-1}\sum_{m=M/2}^{M-1}\Big[2(M-1-m)+1\Big]\times\Big[\langle n_{Mk+j}^2 n_{Mk+m}^2\rangle + \sum_{l=j+1}^{M/2-1} 2\langle n_{Mk+j}n_{Mk+l}n_{Mk+m}^2\rangle\Big]+$$

$$\sum_{j=0}^{M/2-1}\Bigg[\Big[4(M/2-1-j)+1\Big]\langle n_{Mk+j}^4\rangle$$

$$+6\sum_{m=j+1}^{M/2-1}\Big[2(M/2-1-m)+1\Big]\langle n_{Mk+j}^2 n_{Mk+m}^2\rangle$$

$$+\sum_{m=j+1}^{M/2-1} 4\Big[\Big(3(M/2-1-m)+1\Big)\langle n_{Mk+j}n_{Mk+m}^3\rangle$$

$$+\sum_{l=m+1}^{M/2-1} 3\Big(2(M/2-1-l)+1\Big)\langle n_{Mk+j}n_{Mk+m}n_{Mk+l}^2\rangle\Bigg]\Bigg]$$

$$X_k^2 Y_k Y_{k+1}$$

$$= M\sum_{m=M/2}^{M-1}\Bigg[\langle n_{kM+m}^4\rangle + 3\sum_{l=m+1}^{M-1}\langle n_{kM+m}^2 n_{kM+l}^2\rangle$$

$$+3\sum_{l=m+1}^{M-1}\Big[\langle n_{kM+m}n_{kM+l}^3\rangle + 2\sum_{q=l+1}^{M-1}\langle n_{kM+m}n_{kM+l}n_{kM+q}^2\rangle\Big]\Bigg]$$

$$-M\sum_{m=0}^{M/2-1}\sum_{l=M/2}^{M-1}\Big[\langle n_{kM+m}n_{kM+l}^3\rangle + 2\sum_{q=l+1}^{M-1}\langle n_{kM+m}n_{kM+l}n_{kM+q}^2\rangle\Big]$$

$$-M\sum_{m=0}^{M/2-1}\sum_{l=M/2}^{M-1}\Big[\langle n_{kM+m}^2 n_{kM+l}^2\rangle + 2\sum_{q=m+1}^{M-1}\langle n_{kM+m}n_{kM+q}n_{kM+l}^2\rangle\Big]$$

$$+M\sum_{m=0}^{M/2-1}\Bigg[\langle n_{kM+m}^4\rangle + 3\sum_{l=m+1}^{M/2-1}\langle n_{kM+m}^2 n_{kM+l}^2\rangle$$

$$+3\sum_{l=m+1}^{M/2-1}\Big[\langle n_{kM+m}n_{kM+l}^3\rangle + 2\sum_{q=l+1}^{M/2-1}\langle n_{kM+m}n_{kM+l}n_{kM+q}^2\rangle\Big]\Bigg]$$

112

$$X_k^2 Y_{k+1}^2 = \sum_{n=0}^{M-1} \Big[2(M-1-n)+1 \Big]$$

$$\times \left[\sum_{n=0}^{M-1} \sum_{m=M/2}^{M-1} \Big(\langle n_{kM+m}^2 n_{(k+1)M+n}^2 \rangle + 2 \sum_{l=m+1}^{M-1} \langle n_{kM+m} n_{kM+l} n_{(k+1)M+n}^2 \rangle \Big) \right.$$

$$-2 \sum_{m=0}^{M/2-1} \sum_{l=M/2}^{M-1} \langle n_{kM+m} n_{kM+l} n_{(k+1)M+n}^2 \rangle +$$

$$\left. \sum_{m=0}^{M/2-1} \Big(\langle n_{kM+m}^2 n_{(k+1)M+n}^2 \rangle + 2 \sum_{l=m+1}^{M-1} \langle n_{kM+m} n_{kM+l} n_{(k+1)M+n}^2 \rangle \Big) \right]$$

Now we can evaluate Eq. (G.16) (where $r = M/N$):

$$\Gamma_2(N,r) = \frac{M^5 r^3}{144}\Big(5 + \frac{4}{M^3}\Big)T^2 \simeq \frac{25 M^5 r^3}{144}T^2 \qquad (G.17)$$

The $\theta > 0$ case is readily evaluated as followed:

$$\langle H(j,M)H(i+\theta,N) \rangle = \langle (\tilde{y}_j^+ - \tilde{y}_j^-)^2 (\tilde{x}_{i+\theta}^+ - \tilde{x}_{i+\theta}^-)^2 \rangle$$

$$= \left[\sum_{l=0}^{M/2-1} \Big[2(N/2-1-l)+1-N \Big] + \sum_{l=M/2}^{M-1} \Big[2(N-1-l)+1 \Big] \right]$$

$$\times \left[\sum_{m=0}^{M/2-1} \Big[2 \sum_{k=m+1}^{M/2-1} \langle n_{jM+m} n_{jM+k} n_{(i+\theta)N+l}^2 \rangle + \langle n_{jM+m}^2 n_{(i+\theta)N+l}^2 \rangle \Big] \right.$$

$$-2 \sum_{m=0}^{M/2-1} \sum_{k=M/2}^{M-1} \langle n_{jM+n} n_{jM+k} n_{(i+\theta)N+l}^2 \rangle$$

$$\left. + \sum_{m=M/2}^{M-1} \Big[2 \sum_{k=m+1}^{M-1} \langle n_{jM+m} n_{jM+k} n_{(i+\theta)N+l}^2 \rangle + \langle n_{jM+m}^2 n_{(i+\theta)N+l}^2 \rangle \Big] \right]$$

After summing over i and performing Fourier transform and taking the real part we find:

$$Re\{ \sum_{\theta=1}^{T/N-1} e^{2\pi i \theta \omega / T} \sum_{i=0}^{T/N-1-\theta} \langle H(j,M)H(i+\theta,N) \rangle \}$$

$$= \frac{MN(M^2+2)(N^2+2)T}{144\omega^2}$$

113

From Eq.(7.16) we know $\langle H(i,N) \rangle_t \langle H(j,M) \rangle_t = \frac{T^2}{144}(N^2+2)(M^2+2)$, $f_2 = \omega/N$, $f_a = 1/N$, and $f_b = 1/M$ finally we obtain:

$$Re\{S_2(f_2, f_a, f_b)\} \simeq \frac{r}{Tf_2^2} + \frac{25r^5}{f_a} \tag{G.18}$$

114

Appendix H

Derivation of Exponent Relations for $Q_{1.5}$ and Q_2

H.1 Exponent Relation for $Q_{1.5}$

The exponent $Q_{1.5}$ comes from the scaling form for $\Gamma_{1.5}(f_1)$:

$$\Gamma_{1.5}(f_1) \equiv \sum_{t=0}^{T-1/f_1} \langle v(t, f_1) H(t, f_1) \rangle \simeq \frac{A_{1.5}}{f_1^{Q_{1.5}}} \tag{H.1}$$

To ascertain the exponent relation for $Q_{1.5}$ we consider the following:

$$v(t, f_1) = \sum_{x=t}^{t+1/f_1} n_x \sim \frac{1}{f_1} \langle n_x \rangle \tag{H.2}$$

Also, $H(t, f_1) \sim f_1^{-1/\sigma\nu z}$ since it is a measure of the power spectrum ($P(\omega) \sim \omega^{-1/\sigma\nu z}$ [13]). Thus:

$$\Gamma_{1.5}(f_1) \equiv \sum_{t=0}^{T-1/f_1} \langle v(t, f_1) H(t, f_1) \rangle \sim \frac{1}{f_1} \times f_1^{-1/\sigma\nu z}$$

$$\Gamma_{1.5}(f_1) \sim \frac{1}{f_1^{1+1/\sigma\nu z}} \tag{H.3}$$

Thus we find:

$$Q_{1.5} = 1 + 1/\sigma\nu z \tag{H.4}$$

H.2 Exponent Relation for Q_2

The exponent Q_2 comes from the scaling form for $\Gamma_2(f_1)$:

$$\Gamma_2(f_1) \equiv \sum_{t=0}^{T-1/f_1} \langle H(t, f_1)^2 \rangle \simeq \frac{A_2}{f_1^{Q_2}} \tag{H.5}$$

In order to determine the exponent relation for Q_2 in terms of known exponents we need to look at the energy distribution of an avalanche, $D_E(E, r, h)$ (given in [11]):

116

$$D_E(E, r, h) \sim E^{-(1 + \frac{\tau - 1}{2 - \sigma\nu z})} D_E(E^{\frac{2 - \sigma\nu z}{\sigma}}, h/r^{\beta\delta}) \tag{H.6}$$

Where $r = (R - R_c)/R_c$ and $h = (H - H_c)/H_c$. E is energy an avalanche releases, given by $E \simeq \int_{aval} dtV(t)^2/R$, where R is the resistance of the induction coil, and $V(t)$ is the induced voltage [11].

Now to find the scaling of $\sum_{t=0}^{T-1/f_1} \langle H(t, f_1)^2 \rangle$ we must determine the scaling of the power spectrum *squared*, we accomplish this by determining the cosine transform of the convolution of $V(t)^2$ with itself:

$$\sum_{t=0}^{T-1/f_1} \langle H(t, f_1)^2 \rangle \sim \int \cos(f_1\theta) \langle V(t)^2 V(t + \theta)^2 \rangle d\theta \tag{H.7}$$

Eq. (H.7) is also a measure of $\langle E^2 \rangle$, since it is a measure of the power squared, thus $\langle E(f_1)^2 \rangle$ will scale the same way as $\sum_{t=0}^{T-1/f_1} \langle H(t, f_1)^2 \rangle$. So now let us connect Eq. (H.7) with the energy E, and the energy distribution $D_E(E, r, h)$. First we consider $\langle E^2 \rangle$ ($x = \frac{\tau - 1}{2 - \sigma\nu z}$ and $y = \frac{2 - \sigma\nu z}{\sigma}$):

$$\langle E^2 \rangle \sim \int E^2 E^{-(1+x)} D_E(Er^y, h/r^{\beta\delta}) dE \tag{H.8}$$

Let $z = Er^y$, so $dz = r^y dE$ and we get:

$$\langle E^2 \rangle \sim r^{-y} \int (zr^{-y})^{1-x} D_E(z, h/r^{\beta\delta}) dz$$
$$\langle E^2 \rangle \sim r^{y(x-2)} A_E(h/r^{\beta\delta}) \tag{H.9}$$

Now we define $E(\theta)$:

$$E \sim \int V(t)^2 dt \tag{H.10}$$
$$E(\theta) = \int V(t)V(t + \theta) dt \tag{H.11}$$

The scaling of $\langle E(\theta)^2 \rangle$ follows from Eq. (H.9):

117

$$\langle E(\theta)^2\rangle \sim r^{y(x-2)} A_\theta(\theta r^{\nu z}, h/r^{\beta\delta})\tag{H.12}$$

Where A_θ is a universal scaling function. Taking the cosine transform of Eq. (H.12) (and setting $y(x-2) = (2\sigma\nu z + \tau - 5)/\sigma$):

$$\langle E(f_1)^2\rangle \sim \int cos(f_1\theta) r^{(2\sigma\nu z+\tau-5)/\sigma} A_\theta(\theta r^{\nu z}, h/r^{\beta\delta}) d\theta\tag{H.13}$$

Setting $l = f_1\theta$ we get:

$$\langle E(f_1)^2\rangle \sim r^{(2\sigma\nu z+\tau-5)/\sigma} \mathcal{E}_{f_1}(f_1 r^{-\nu z}, h/r^{\beta\delta})\tag{H.14}$$

$$\langle E(f_1)^2\rangle \sim f_1^{-\left[\frac{5-\tau}{\sigma\nu z}-2\right]} \mathcal{E}_{f_1}(f_1 r^{-\nu z}, h/r^{\beta\delta})\tag{H.15}$$

Where $\mathcal{E}_{f_1} \equiv \int dl A_\theta(l,...)cos(l) dl$ (assuming the integral is nonsingular). Thus we have:

$$Q_2 = \frac{5-\tau}{\sigma\nu z} - 2\tag{H.16}$$

118

References

[1] J.P. Sethna, K. A. Dahmen, and C.R. Myers, *Crackling Noise*, Nature **410**, 242 (2001).

[2] L. P. Kadanoff, Physics **2**, 263-272 (1966).

[3] K. G. Problems in physics with many scales of length. Sci. Am. **241**, 140-157 (1979).

[4] M. E. Fisher, Rev. Mod. Phys.**70**, 653-681 (1998).

[5] P. C. Martin, E. D. Siggia, and H. A. Rose, Phys. Rev. A **8**, 423-437 (1973).

[6] S. Field, J. Witt, F. Nori, and X. Ling, Phys. Rev. Lett. **74**, 1206 (1995).

[7] W. Wu and P. W. Adams, Phys. Rev. Lett. **74**, 610 (1995).

[8] M. P. Lilly, P. T. Finley, and R. B. Hallock, Phys. Rev. Lett. **71**, 4186 (1993); A.H. Wooters and R.B. Hallock, Physica B **141**, 284 (2000).

[9] Ortín, J. et al. *J. Phys. IV (Paris)* **5**, 209 (1995).

[10] B. Gutenberg and C.F. Richter, Ann. Geofis. **9**, 1 (1956).

[11] K. A. Dahmen, *Hysteresis, Avalanches, and Disorder Induced Critical Scaling: A Renormalization Group Approach*, Ph.D. Thesis, Cornell University (May 1995); K. Dahmen, and J. P. Sethna, Phys. Rev. B **53**, 14872 (1996).

[12] J. P. Sethna, J. D. Shore, and M. Huang, Phys. Rev. B **44**, 4943 (1991), and references therein; J. D. Shore, Ph.D. Thesis, Cornell University (1992), and references therein; T. Riste and D. Sherrington, *Phase Transitions and Relaxation in Systems with Competing Energy Scales* (Proc. NATO Adv. Study Inst., Geilo, Norway, April 13-23, 1993), and references therein; M. Mézard, G. Parisi, M. A. Virasoro, *Spin Glass Theory and Beyond* (World Scientific, Singapore, 1987), and references therein; K. H. Fischer and J. A. Hertz, *Spin Glasses* (Cambridge University Press, Cambridge, 1993), and references therein; G. Grinstein and J. F. Fernandez, Phys. Rev. B **29**, 6389 (1984); J. Villain, Phys. Rev. Lett. **52**, 1543 (1984); D. S. Fisher, Phys. Rev. Lett. **56**, 416 (1986).

[13] Matthew C. Kuntz, and James P. Sethna, Phys. Rev. B **62**, 11699 (2000).

[14] G. Durin and S. Zapperi, Phys. Rev. Lett. **84**, 4705 (2000).

[15] G. Durin, private communications.

[16] H. Ji and M. O. Robbins, Phys. Rev. B **46**(22), 14519 (1992).

[17] B. Alessandro, C. Beatrice, G. Bertotti, and A. Montorsi, J. Appl. Phys. *68*, 2901 (1990).

[18] Amit P. Mehta, Andrea C. Mills, Karin Dahmen, and James P. Sethna, Phys. Rev. E **65**, 46139 (2002).

[19] G. Durin and S. Zapperi, preprint (2004), Alamos Nat'l Laboratory Archive, http://xxx.lanl.gov/abs/cond-mat/0404512.

[20] S. Zapperi, P. Ray, H. E. Stanley, A. Vespignani, *Phys. Rev. E*, **59**, 5049-5057, (1999).

[21] Y. Utsu, Y. Ogata, R. S. Matsu'uara,*J. Phys. Earth*, **43**,1-33 (1995).

[22] C. Kisslinger, L. M. Jones, *J. Geophys. Res.*, **96**, 11,947-11,958 (1991).

[23] Y. Ben-Zion, *International Handbook of Earthquake and Engineering Seismology* (Academic Press,2003), Part B, pp.1857-1875.

[24] T. C. Hanks, H. Kanamori, *J. Geophys. Res.*, **84**, 2348 - 2350 (1979).

[25] T. Utsu, *International Handbook of Earthquake and Engineering Seismology*,W. HK Lee, H. Kanamori, P. C. Jennings, C. Kisslinger, Eds. (2002) Part A, pp. 719-732).

[26] C. Frohlich, S. D. Davis, *JGR*, **98**, 631-644 (1993).

[27] D. S. Fisher, K. Dahmen, S. Ramanathan, Y. Ben-Zion, *Phys. Rev. Lett.*, **78**, 4885-4888 (1997).

[28] S. G. Wesnousky, *Bull. Seismol. Am.*, **84**, 1940-1959 (1994).

[29] M. W. Stirling, S. G. Wesnousky, K. Shimazaki,*Geophys. J. Int.*, **124**, 833-868 (1996).

[30] P. Bak, C. Tang, K. Wiesenfeld, *Phys. Rev. A*, **38**, 364-374 (1988).

[31] D. Sornette, C. G. Sammis, *J. Phys. I France*, *5*, 607-619 (1995).

[32] W. Klein, M. Anghel, C. D. Ferguson, J. B. Rundle, J. S. Sa' Martins, *Geophys. Mono. Series* **120**, *GeoComplexity and the Physics of Earthquakes*, J. B. Rundle, D. L. Turcotte, W. Klein, Eds.(American Geophysical Union, Washington, DC., 2000) pp.43-71.

[33] M. Schroeder, *Fractals, chaos, power laws* (W. H. Freeman and Co., 1991).

[34] D. Sornette, *Critical phenomena in natural sciences, Chaos, fractals, self-organization, and disorder: concepts and tools* (Springer-Verlag, 2000).

[35] R.D. Merithew, M.W. Rabin, M.B. Weissman, M.J. Higgins, and S.Bhattacharya, Phys. Rev. Lett. **77**(15), 3197 (1996).

[36] M.G.A. Thomson, Phys. Rev. Lett. **86**(13), 2901 (2001).

[37] C.E. Parman, N.E. Israeloff, and J. Kakalios, Phys. Rev. Lett. **69**(7), 1097 (1992).

[38] G.T. Seidler, and S.A. Solin, Phys. Rev. B **53**(15), 9753 (1996).

[39] M.B. Weissman, Annu. Rev. Mater. Sci. **26**, 395 (1996).

[40] D.S. Fisher, Phys. Reports **301**, 113 (1998).

[41] H. Houston, J. Geophys. Res. **106**, 11137 (2001).

[42] Djordje Spasojević, Srdjan Bukvić, Sava Milösević, and H. E. Stanley, Phys. Rev. E **54**, 2531 (1996).

[43] G. Durin, S. Zapperi, preprint (2001), Alamos Nat'l Laboratory Archive, http://xxx.lanl.gov/abs/cond-mat/0106113.

[44] G. Durin and S. Zapperi, J. Appl. Phys. *85*, 5196 (1999).

[45] Y. Tanoika and L. Ruff, Seismol. Res. Lett. **68**, 386 (1997).

[46] L. J. Ruff and A. D. Miller, Pure Appl. Geophys. **142**, 101 (1994).

[47] Y. Ben-Zion, J. R. Rice,*J. Geophys. Res.*, **98**, 14109-14131 (1993).

[48] J.R. Petta, M.B. Weissman, and G. Durin, Phys. Rev. E **57**(6), 6363 (1998).

[49] K.P. O'Brien and M.B. Weissman, Phys. Rev. E **50**(5), 3446 (1994)

[50] H. Safar, P.L. Gammel, D.A. Huse, G.B. Alers, and D.J. Bishop, Phys. Rev. B **52**, 6211 (1995); J.R. Clem, Phys. Rep. **75**, 1 (1981).

[51] J.P. Sethna, K. Dahmen, S. Kartha, J.A. Krumhansl, B.W. Roberts, J.D. Shore, Phys. Rev. Lett. **70**, 3347 (1993).

[52] J.S. Urbach, R.C. Madison, and J.T. Markert, Phys. Rev. Lett. **75**(2), 276 (1995).

[53] O. Narayan, Phys. Rev. Lett. **77**(18), 3855 (1996).

[54] S. Zapperi, P. Cizeau, G. Durin, and H.E. Stanley, Phys. Rev. B **58**(10), 6353 (1998).

[55] Olga Perković, Karin A. Dahmen, and James P. Sethna, Phys. Rev. B **59**, 6106 (1999).

[56] Olga Perković, Karin Dahmen, and James P. Sethna, Phys. Rev. Lett. **75**, 4528 (1995).

[57] Matthew C. Kuntz, Olga Perković, Karin A. Dahmen, Bruce W. Roberts, and James P. Sethna, *Comput. Sci. Eng.* **1**, 73 (1999).

[58] James P. Sethna, Olga Perković, and Karin A. Dahmen, preprint (1997), Los Alamos Nat'l Laboratory Archive, http://xxx.lanl.gov/abs/cond-mat/9704059.

[59] Y. Ben-Zion,*J. Geophys. Res.*, **101**, 5677-5706 (1996);Y. Ben-Zion, J. R. Rice,*J. Geophys. Res.*, **100**, 12959-12983 (1995).

[60] D. S. Fisher, K. Dahmen, S. Ramanathan, Y. Ben-Zion, *Phys. Rev. Lett.*, **78**, 4885-4888 (1997).

[61] K. A. Dahmen, D. Ertas, Y. Ben-Zion,*Phys. Rev. E*, **58**, 1494-1501 (1998).

[62] D. Vere-Jones, *Pure and Appl. Geophys.*, **114**, no.4, p. 711-726 (1976).

[63] Y. Ben-Zion, C. G. Sammis, *Pure appl. Geophys.*, **160**, 677-715 (2003).

[64] J. Liu, K. Sieh, E. Hauksson,*Bull. Seism. Soc. Am.*,**93**, 1333-1344 (2003).

[65] S. Zapperi, P. Cizeau, G. Durin, H. E. Stanley, *Phys. Rev. B*, **58**(10), 6353-6366 (1998).

[66] J. J. Binney, N. J. Dowrick, A. J. Fisher, M. E. J. Newman, *The theory of critical phenomena* (Oxford University Press, 1993).

[67] Matthew C. Kuntz, James P. Sethna, private communications.

[68] Gianfranco Durin, private communications.

[69] S. L. Bilek, PhD thesis, (University of California, Santa Cruz, 2001), pp. 180.

[70] A. P. Mehta, A. C. Mills, K. A. Dahmen, J. P. Sethna, *Phy. Rev. E.*, **65**, 46139/1-6 (2002).

[71] D. S. Fisher, *Phys. Reports*, **301**, 113-150 (1998).

[72] P. M. Mai, P. Spudich, J. Boatwright, *Seis. Res. Lett.*, **74**, 208 (2003).

[73] Yehuda Ben-Zion, private communciations.

Vita

Amit Pankaj Mehta was born on April 29th, 1978 in Denville, NJ. He attend Parsippany Hills high school in Parsippany, NJ from fall of 1992 to spring of 1996. In the spring of 1996 he was accepted to Cornell University in Ithaca, NY for undergraduate studies. In May of 2000 he completed his studies at Cornell with a BA in Physics. In the summer of 2000 he began his graduate studies under the tutelage of Professor Karin Dahmen.

124